

NUCLEAR FISSION AND TUNNELING PHENOMENA

By

Eric Douglas Flynn

A DISSERTATION

Submitted to
Michigan State University
in partial fulfillment of the requirements
for the degree of

Physics — Doctor of Philosophy
Computational Mathematics, Science and Engineering — Dual Major

2025

ABSTRACT

The fission of neutron-rich heavy, and superheavy, nuclei is hypothesized to impact r -process nucleosynthesis. However, the lack of experimental data for these nuclei demands theoretical predictions with quantified uncertainties. Nuclear energy density functional theory (DFT) has had success predicting fission lifetimes and yields for many r -process nuclei by representing the process as a tunneling problem in a collective space. In this dissertation, I will describe the current DFT framework we use and introduce an implementation of the nudged elastic band technique. I then discuss the application of the nudged elastic band to calculate fission lifetimes and yields to study nuclei with competing modes of fission. Then, I discuss recent progress towards improving our theoretical framework of fission using an instanton approach to model nuclear fission. Furthermore, I will highlight possible overlaps of this approach with nuclear dynamics. I propose an algorithm to find mean-field instanton solutions and I conclude with future directions for the instanton approach for nuclear fission and future applications of the nuclear DFT approach to fission lifetimes and yields.

To my fiancée Isabella

ACKNOWLEDGMENTS

First, I sincerely thank my advisor Witek Nazarewicz for giving me the opportunity to work in nuclear theory and for his is guidance, mentorship, and support throughout my entire graduate career. I also want to thank my thesis committee Hendrik Schatz, Scott Bogner, Alexei Bazavov, and Ekaterina Rapinchuk for their support.

I am very grateful for my collaborators Sylvester Agbemava, Pablo Giuliani, Samuel Giuliani, Kyle Godbey, Daniel Lay, Scott Lawrence, Jhila Sadhukhan, Semeon Valgushev, and Yukari Yamauchi. It was very exciting working with you all and I learned very much from all of you. Also thanks for tolerating my dumb questions.

I also thank present and past members of my research group for support and great conversations about nuclear physics: Josh Belieu, Maxwell Cao, Mengzhi Chen, Richard Gumbel, Bailey Knight, Sudhanva Lalit, Tong Li, Josh Nicholson, Ante Ravlić, Yukiya Saito, Mookyong So, Simin Wang, and Josh Wylie.

Special thanks goes to Sudhanva Lalit, Daniel Lay, Yukiya Saito, and Josh Wylie for providing wonderful feedback on my thesis and helping me stay motivated.

I was very lucky to be surrounded by many great people around FRIB and the physics department: Grayson Perez, Hieu Le, Mo Hassan, Jordan Purcell, Sheng Lee, Alex Adams, Yuanzhuo Ma, and Xilin Zhang, Andy Smith, Patrick Cook, Danny Jammooa, Nick Cariello, and Yani Udiani. I have had many great conversations with everyone and I have also learned a lot from all of you.

I especially would like to thank Jocelyn Read, Alfonso Agnew, Geoffrey Lovelace, Josh Smith, Marissa Walker, and the Gravitational Wave Physics and Astronomy Center at California State University, Fullerton. I am forever grateful to them for giving me a chance to do physics and mathematics research as an undergraduate. As someone who consistently

struggled with mathematics as a kid, they were the first ones to convince me I might have a little bit of a chance at becoming a scientist. I certainly would not be where I am today without them.

Finally I would like to thank my family. My dad, Doug, my mom, Julie, my sister Elizabeth and my brother-in-law Luigi, My uncles Art, Chuck, Oscar, Joe, and Mike and my aunts Gloria, Holly, and Martha, and my Grandparents Raul, Silva, Gene, and Alice. You all defined what I am today.

TEACHERS

Douglas Flynn, Julie Flynn, Elizabeth Flynn, Art Valencia, Gloria Valencia, Oscar Valencia, Chuck Valencia, Holly Flynn, Raul Valencia, Silva Valencia, Gene Flynn, Alice Flynn, Martha Anguiano, Joe Anguiano, Micheal Anguiano.

Zach Miller, Jodi Davis, James Lyle, June Mutrias, Daniel Van Nice, Lynn Van Nice.

Andrew Carlson, Ricky Dixon, Vaughn Sutterman, Ty Tu, Justin Martin, Joel Zimmerman, Todd Edwards, Richard Feynman, Kip Thorne, Murray Gell-mann, Norman Borlaug, Jacque Pepin, Julia Child, Hayao Miyazaki, Clifford Stoll, Martyn Poliakoff.

Jocelyn Read, Josh Smith, Geoffrey Lovelace, Alfonso Agnew, Marissa Walker, Tommy Murphy, Matthew Rathbun, Ionel Tifrea, Michael Loverude, Leigh Hargraves, Edgar Lara, Alyssa Garcia, Haroon Khan, Nick Demos, Torrey Collen, Nousha Afshari, Conner Park, Jesus Rangel, Michael Giolli, Edgard Bonilla.

Witek Nazarewicz, Daniel Lay, Josh Wylie, Grayson Perez, Samuel Giuliani, Sylvester Agbemava, Pablo Giuliani, Kyle Godbey, Alex Adams, Sudhanva Lalit, Ante Ravlić, Aurora Aksnes,

and the two robots.

TABLE OF CONTENTS

LIST OF TABLES	viii
LIST OF FIGURES	ix
Chapter 1. Introduction	1
1.1 Dissertation Organization	4
Chapter 2. Nuclear Mean-field Theory	6
2.1 Theoretical Foundations	6
2.2 Structure of a Nuclear Energy Density Functional	12
2.2.1 The Skyrme Functional	16
2.2.2 The Gogny Functional	19
2.3 Symmetries and Constraints	20
2.3.1 Particle Number and Pairing Fluctuations	20
2.3.2 Nuclear Deformation	22
2.4 Numerical Solution of the HFB Equations	24
Chapter 3. Spontaneous Nuclear Fission	25
3.1 Nuclear Fission as an Adiabatic Process	25
3.2 Tunneling in the Reduced Space	31
3.3 The Nudged Elastic Band Method	33
3.4 Analytic Examples	36
3.5 Realistic Examples	37
3.6 Summary	41
Chapter 4. Modes of Spontaneous Fission	42
4.1 Fission Fragment Distributions	42
4.1.1 Time-dependent Approach	42
4.1.2 Stochastic Methods	43
4.1.3 Hybrid Method	45
4.2 Applications	48
4.2.1 The Fermium Isotope Chain	48
4.2.2 Superheavy Nuclei	52
4.3 The Need for Reduced Order Modeling	54
4.4 Summary	54
Chapter 5. The Instanton Approach to Nuclear Fission Lifetimes	56
5.1 Path Integral Representation	57
5.2 Non-Relativistic Models	61
5.2.1 Transition Amplitudes	63
5.2.2 The Bounce Equations	67
5.3 Meson Exchange Models	72
5.3.1 Transition Amplitudes	74

5.3.2	Bounce Equations	78
5.4	Bounce Search Algorithm	80
5.5	Summary	82
Chapter 6. Future Investigations		83
6.1	Nuclear Fission Lifetimes and Yields with DFT	83
6.2	Instanton and Mean-field Extensions	84
6.3	Dimensionality Reduction for Nuclear Physics	85
APPENDIX A. Minimum Energy and Least Action Pathways		87
APPENDIX B. Derivation of Yukawa Path Integral		92
BIBLIOGRAPHY		99

LIST OF TABLES

Table 3.1: Action integrals for the 6-Camel-Back (CB-S and CB-A) and Müller-Brown (MB) surfaces. The integrals have been calculated using a linear spline interpolation evaluated at 500 points along each trajectory. Table taken from Ref. [159].	36
Table 3.2: Action integrals for ^{232}U computed using DPM, DA, EL method, and the NEB. The paths are computed using constant and non-perturbative inertia tensor are labeled as “con.” and “n.-p.”, respectively. The actions were computed using a linear spline interpolation evaluated at 500 points along each trajectory. Table taken from [159]	39
Table 4.1: The relative probability P_s of the symmetric mode for the 2D calculation of Fm isotopes.	50

LIST OF FIGURES

Figure 1.1:	Partition of the nuclear chart highlighting relevant regions for r -process nucleosynthesis. The green arrow schematically represents the r -process trajectory through the region of the chart predicted to exist by FDRM2012 [17]. The black and gray squares label the stable and measured nuclei respectively [18]. The blurred red boundary schematically represents the approximate location of the neutron dripline.	3
Figure 1.2:	Schematic representation of the different stages of fission separated by time scale starting from an initial state to scission. Figure taken from Ref. [33].	4
Figure 2.1:	Schematic representation of the energy functional $E[\Psi\rangle]$ over the space \mathcal{F} . $E[\Psi\rangle_{\text{KS}}]$ is defined over the low dimensional Kohn-Sham domain indicated by the red curve. The Kohn-Sham subset contains a state that reproduces the ground state energy E_{GS}	7
Figure 3.1:	Schematic representation of the time-dependent fission trajectory in the many-body manifold \mathcal{F} . The green curve represents the adiabatic density trajectory $\mathcal{R}^{(0)}(t)$. The curvature about $\mathcal{R}^{(0)}(t)$ is schematically represented by the dashed lines. The local variations in the pathway $\delta\mathcal{R}$ are represented by the solid black line connecting to an alternate pathway denoted by the dotted line. The $\delta^2\mathcal{R}$ is schematically represented by the width between the dashed lines.	27
Figure 3.2:	Calculated PES for ^{256}Fm parameterized by Q_{20} and Q_{30} using D1S EDF. Details are discussed in Ref. [159]. Figure taken from Ref. [159]	37
Figure 3.3:	Calculated ^{232}U PES (in MeV) using the SkM* EDF. The solid lines correspond to pathways obtained using constant inertia while the dotted lines are those obtained with non-perturbative inertia. The blue, orange, purple, and black curves represent the LAPs calculated using the NEB, DPM, EL, and DA methods, respectively. The green curve is the MEP calculated using NEB and the outer turning line is shown in white. Figure taken from Ref. [159].	38
Figure 3.4:	The PES (in MeV) for ^{240}Pu in the collective coordinates Q_{20} , Q_{30} and λ_2 . The 2D cross section of the PES of ^{240}Pu at $\lambda_2 = 0$ is shown. The blue, orange, and purple curves are the LAP, calculated using the NEB, DPM, and EL methods, respectively. The dashed curves are pathways computed with non-perturbative inertia. The outer turning surface is indicated by the dark blue meshed surface. Figure taken from Ref. [159].	40

Figure 4.1:	The nucleon localization functions calculated at an asymmetric exit point configuration of ^{254}Fm using the SkM* EDF. (a) and (b) are neutron and proton localizations respectively. Horizontal dashed lines denote the selected center of the prefragments.	46
Figure 4.2:	Potential energy surfaces of $^{254-260}\text{Fm}$ (in MeV) calculated using UNEDF1 _{HFB} (left column), SkM* (center column), and D1S (right column) EDFs. The symmetric (dashed lines) and asymmetric (solid and dotted lines) least action paths are drawn from the ground state (solid circle) to the fission isomer (asterisk) to the exit point (open square). The white contour denotes the outer turning line. Gray contours are marked at 1-MeV intervals for $0 < V_{\text{eff}} < 5$ MeV. Figure taken from Ref. [176]	49
Figure 4.3:	Fission fragment mass (left) and charge (right) yields for $^{254,256,258,260}\text{Fm}$ calculated with UNEDF1 _{HFB} (magenta vertical patterns), SkM* (black horizontal patterns), and D1S (green \times patterns). Experimental yields (circles) [220–223] are shown where available. Figure taken from Ref. [176].	50
Figure 4.4:	The least action paths in 3D for ^{258}Fm using SkM*. The outer turning surface is shown. A 2D PES is shown for constant $Q_{40} = 16 \text{ b}^2$. Neutron localizations for the identified precession configurations are shown in the insets. Figure adapted from Ref. [176].	51
Figure 4.5:	The fragment mass (left) and charge (right) yields for ^{258}Fm using SkM* calculated in the 2D (green solid lines) and 3D (blue lines) collective spaces. Experimental data from [223] is shown as red filled circles. Figure adapted from Ref. [176].	52
Figure 4.6:	Similar as Fig. 4.4 but for $^{306}_{122}$. The 2D surface is at constant $Q_{40} = 0$. Figure adapted from Ref. [176].	53
Figure 5.1:	An example of a real-time saddle point of the action with a cubic potential. The outer turning point (OTP) of the barrier is denoted with the orange circle.	59
Figure A.1:	The asymmetric camel-back surface $V_{\text{CB-A}}(x, y)$ with the calculated NEB-MEP (red), NEB-LAP (magenta), DPM (black), EL (cyan), and DA (lime) trajectories. Black stars indicate saddle points and yellow crosses mark local minima. Figure taken from Ref. [159]	87

Figure A.2: Absolute value of the minimum angle (in degrees) between the gradient of V and the eigenvectors of the Hessian H for the CB-S surface. The NEB-MEP is shown in red and NEB-LAP is shown in green. The yellow stars indicate critical points of the surface. The inset zooms-in on one region where there is a slight difference in the MEP path compared to the LAP. Figure taken from Ref. [159]. 90

Chapter 1. Introduction

Nuclear fission is currently understood as a spontaneous or induced, time-dependent, quantum mechanical process that transforms a nucleus into two or three smaller nascent fragments. Much of this understanding follows from experiments and theoretical models from the 1930's. In 1934, Enrico Fermi and collaborators irradiated uranium with neutrons and observed subsequent beta decays [1]. It wasn't until 1939 when Otto Hahn and Fritz Straßmann discovered decay products barium, strontium, yttrium, and krypton following the neutron irradiation of uranium. Their observations provided strong evidence the uranium nucleus was in fact splitting into two fragments [2]. Lise Meitner and Otto Frisch named the splitting "nuclear fission" and developed a qualitative description of the phenomena based on the concept of a charged liquid drop [3, 4]. Bohr and Wheeler formalized Meitner and Frisch's ideas into a quantitative theory in their seminal paper [5]. In their publication, they postulated that the nucleus behaves like a semi-classical charged liquid drop that is unstable against deformation. They characterized the instability by parameterizing the potential energy of the nucleus with various modes of nuclear deformation. This characterization defined a paradigm that persists in many models of fission used today.

Despite the success of the paradigm, there are still open problems regarding the origin of fissioning nuclei and the fission mechanism that have yet to be solved. It is known that many fissioning nuclei are actinides (heavy elements) with atomic numbers ranging between 89 and 102 and trans-actinides (superheavy elements) with atomic numbers greater than 102. Determining the natural production site of heavy and superheavy nuclei is an open problem in nuclear physics, and forming these elements in terrestrial laboratories is very challenging (see Refs. [6–9] for reviews). By studying the astrophysical rapid neutron capture process abundance patterns, we can learn about the origin of heavy and superheavy nuclei.

There are two primary neutron capture processes identified to be responsible for element formation beyond the iron group. Depending on the time scale of neutron capture compared to the time scale of beta decay [10], these two processes have been called slow neutron capture process (*s*-process) and the rapid neutron capture process (*r*-process) [11]. Since the formation path of the *s*-process lies along the valley of beta stability, most of the properties of relevant nuclei have been experimentally studied. Additionally, the astrophysical sites of the *s*-process are known (see, for example, Ref. [12] and references therein). On the other hand, the *r*-process involves thousands of neutron-rich nuclei that are currently beyond the reach of experimental studies, and the astrophysical events in which the *r*-process occurs remain elusive. The *r*-process requires neutron fluxes large enough for neutron capture reactions to dominate over beta decay. The only known sites capable of producing such large neutron fluxes are binary neutron star (BNS) mergers [13], binary black hole-neutron star (BH-NS) mergers [14, 15], and highly spinning core-collapse supernova [16].

One prediction of nuclei hypothesized to take part in the *r*-process is highlighted in red in Fig. 1.1 and the green arrow schematically represents an *r*-process synthesis trajectory. The predicted nuclei are neutron-rich and primarily take part in the *r*-process through β^- decay, neutron capture, photodisintegration, beta-delayed neutron emission, and nuclear fission.

To study the synthesis of heavy elements, one considers the nuclear abundances as a function of time during a simulation of one of the proposed astrophysical events. High-fidelity simulations of compact binary mergers and core-collapse supernovae are needed to study the abundances of nuclei produced at these sites [19–21]. Nuclear abundance histories are calculated by solving reaction networks which consist of a set of differential equations

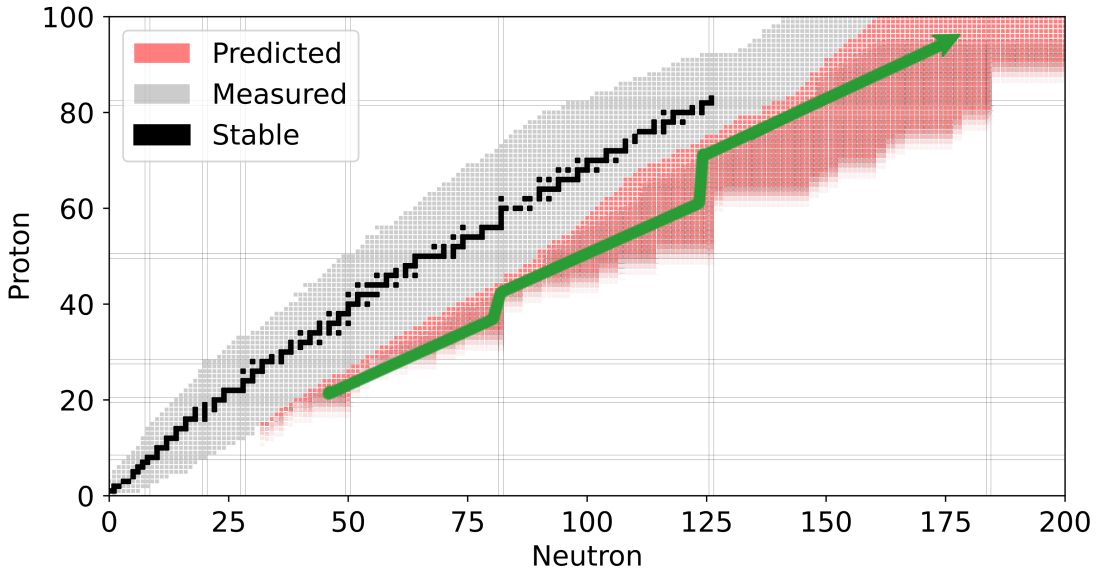


Figure 1.1: Partition of the nuclear chart highlighting relevant regions for r -process nucleosynthesis. The green arrow schematically represents the r -process trajectory through the region of the chart predicted to exist by FDRM2012 [17]. The black and gray squares label the stable and measured nuclei respectively [18]. The blurred red boundary schematically represents the approximate location of the neutron dripline.

given by [22],

$$\frac{dY_i}{dt} = f(Y_k, T, \lambda_k), \quad (i = 1, 2, \dots, N) \quad (1.1)$$

where Y_i labels the particle species abundance, and f is function of the temperature, T , and the rate of reactions or decays taking part in the evolution, λ_k . N denotes the total number of species in the network. Nuclear reaction and structure measurements or theoretical predictions in the form of reaction or decay rates and yields are necessary inputs for the reaction network. In particular, studies to date have shown that nuclear fission rates and fragment distributions influence the abundances of lighter nuclei produced in the r -process through the fission cycling mechanism [23–29]. However, fission observables are significant sources of uncertainty [30–32]. Many fissioning nuclei hypothesized to take part in the r -process lack

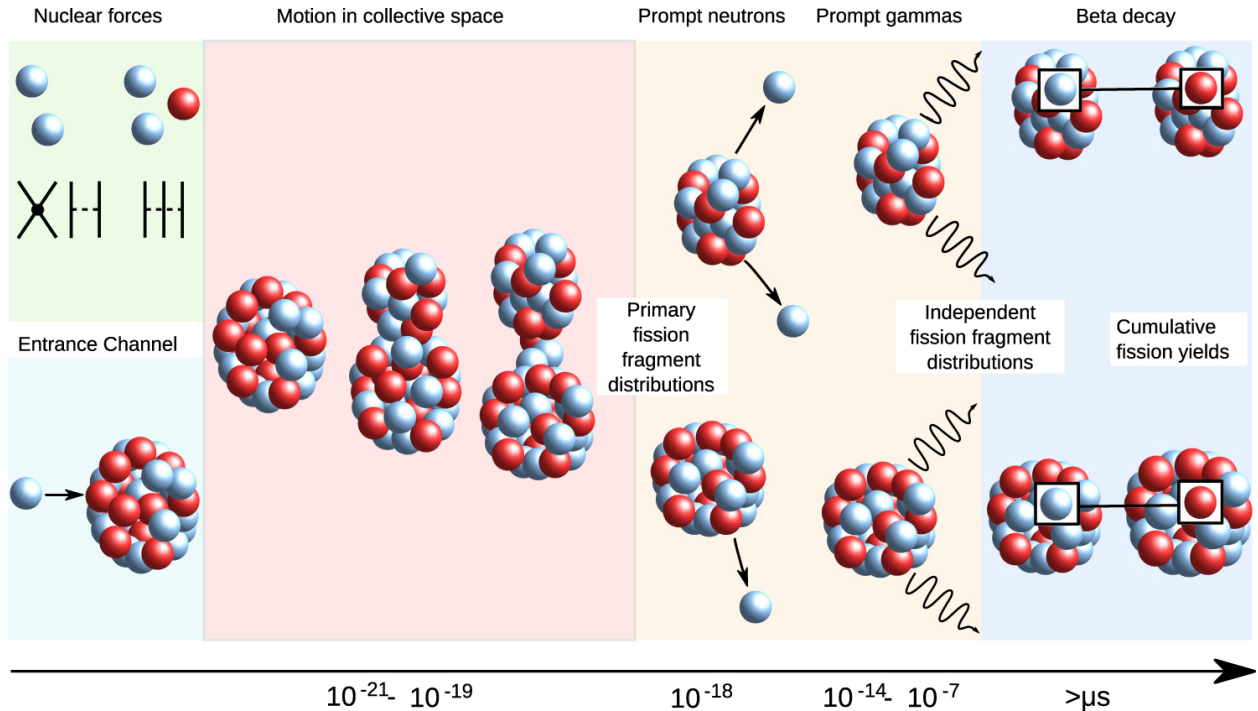


Figure 1.2: Schematic representation of the different stages of fission separated by time scale starting from an initial state to scission. Figure taken from Ref. [33].

experimental data. Therefore, to assess the impact of fission in the r -process, one must rely on theoretical predictions.

A complete quantum mechanical theory of fission is needed to systematically predict fission observables [33]. This theory must appropriately treat the nuclear interactions and the many-nucleon physics across a very wide time scale. Rather than solving the entire nuclear dynamics from initial state to final state, the process partitioned into stages separated by timescale. Fig. 1.2 from Ref. [33] shows typical time scale separations defining the different stages of fission. An overview of each stage is given in Ref. [33]. In this dissertation, we study the collective motion stage leading to nascent fission fragments to advance our theoretical models of nuclear fission.

1.1 Dissertation Organization

The dissertation is organized as follows: In Ch. 2 we overview the theoretical foundations

of the non-relativistic nuclear mean-field theory. In Ch. 3 we discuss how mean-field theory is used to study spontaneous fission and the methods used to calculate fission lifetimes. In Ch. 4 we apply this approach to select nuclei with competing modes of fission and discuss the methods used to calculate fission mass and charge yields. Ch. 5 discusses the many-body tunneling and the instanton method as a possible framework that extends beyond the mean-field approach introduced in Ch. 2. Finally, conclusions and future work is outlined in Ch. 6.

Chapter 2. Nuclear Mean-field Theory

2.1 Theoretical Foundations

Our description of fission is rooted in nuclear mean-field theory. This approach approximates many-body interactions with effective interactions and many-body wave-functions¹. We select the vacuum (also called a reference) state that minimizes the total energy of the many-body system,

$$|\Psi\rangle = \arg \min_{|\tilde{\Psi}\rangle} \frac{\langle \tilde{\Psi} | \hat{H} | \tilde{\Psi} \rangle}{\langle \tilde{\Psi} | \tilde{\Psi} \rangle} = \arg \min_{|\tilde{\Psi}\rangle} E [|\tilde{\Psi}\rangle] \quad (2.1)$$

where $|\tilde{\Psi}\rangle$ is an arbitrary state and \hat{H} is the many-body Hamiltonian in second quantization:

$$\hat{H} = \sum_{p,q=0}^{\infty} \langle p | \hat{z} | q \rangle \hat{\eta}_p^\dagger \hat{\eta}_q + \frac{1}{2} \sum_{p,q,r,s=0}^{\infty} \langle pq | \hat{v} | rs \rangle \hat{\eta}_p^\dagger \hat{\eta}_q^\dagger \hat{\eta}_s \hat{\eta}_r + \dots \quad (2.2)$$

E is referred to as the energy functional. The operator \hat{z} contains one-body interactions such as the kinetic energy operator, \hat{v} contains two-body interactions, and so on. $\hat{\eta}_p$ and $\hat{\eta}_p^\dagger$ are fermionic annihilation and creation operators defined on an anti-symmetrized Fock space \mathcal{F} satisfying anti-commutation relations

$$\{\hat{\eta}_p^\dagger, \hat{\eta}_q\} = \delta_{pq}, \quad \{\hat{\eta}_p, \hat{\eta}_q\} = \{\hat{\eta}_p^\dagger, \hat{\eta}_q^\dagger\} = 0 \quad (2.3)$$

If the minimization procedure is unrestricted in \mathcal{F} , then the optimization is equivalent to solving for the exact many-body ground state by the Rayleigh-Ritz variational principle [34]. This is computationally intractable as the cardinality of \mathcal{F} scales exponentially with

¹Unless otherwise stated, we use natural units $\hbar = c = 1$ and assume Einstein summation convention.

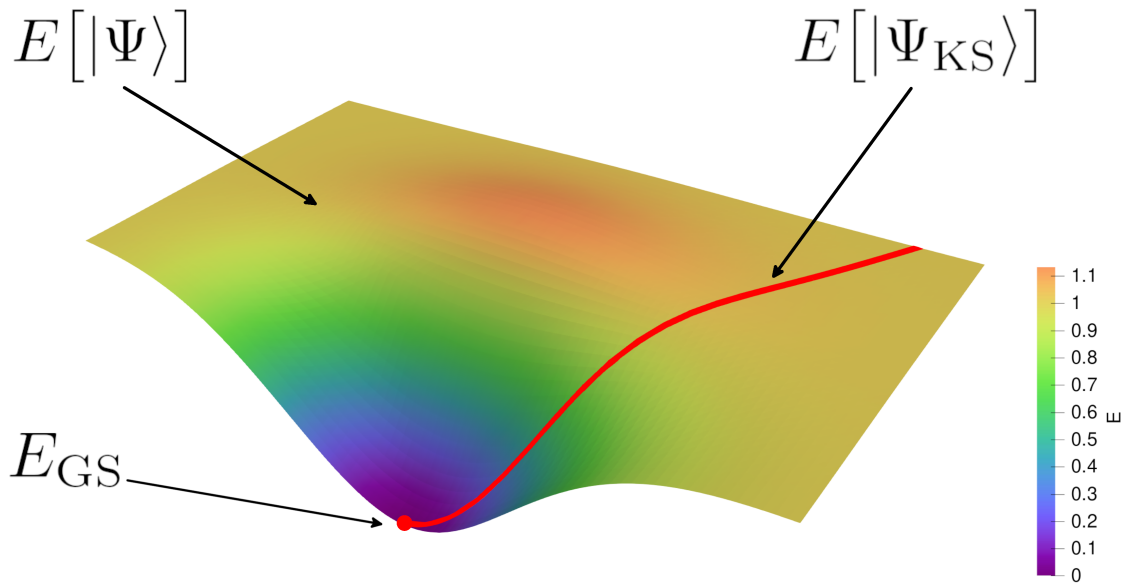


Figure 2.1: Schematic representation of the energy functional $E[|\Psi\rangle]$ over the space \mathcal{F} . $E[|\Psi\rangle_{\text{KS}}]$ is defined over the low dimensional Kohn-Sham domain indicated by the red curve. The Kohn-Sham subset contains a state that reproduces the ground state energy E_{GS} .

the number of nucleons [35].

An ansatz by Kohn and Sham [36] maps the minimization over \mathcal{F} to a minimization over a significantly smaller subspace spanned by states representing a fictitious non-interacting system of independent fermions. The Kohn-Sham domain is a small subset of \mathcal{F} and contains a non-interacting fermion state that reproduces the true many-body ground state energy. This is schematically represented in Fig. 2.1. The ansatz makes the minimization computationally tractable [37, 38]. In nuclear physics, the Kohn-Sham assumption is well motivated by the success of the independent particle picture underlying the nuclear shell model [39]. Further, ab initio studies of finite nuclei have shown that residual interactions from 3-body or higher forces are much smaller compared to the normal ordered one-body potentials [40–42]. Nevertheless, mean-field theory does not completely solve the nuclear many-body problem. Other approaches which attempt to go beyond the independent particle approximation

include using multi-reference states [43–46], the coupled-cluster approach [47–50], and the In-Medium-Similarity-Renormalization-Group (IMSRG) method [51–53]. We assume our many-body system is well represented by a single Kohn-Sham state.

One commonly used Kohn-Sham state is a particle-hole Slater determinant which yields the Hartree-Fock (HF) equation from the minimization of E . While this choice has been used extensively to describe nuclear ground states, excited states, and dynamics (for example, see Refs. [54, 55] and the references therein), the particle-hole Slater determinant neglects superfluid features observed in nuclei [34, 56]. For this reason, we assume a quasi-particle Slater determinant defined by the Bogoliubov transformation of particle-hole annihilation and creation operators [34],

$$\hat{\beta}_p^\dagger = \sum_q \left(U_{qp} \hat{\eta}_q^\dagger + V_{qp} \hat{\eta}_q \right), \quad \hat{\beta}_p = \sum_q \left(U_{qp}^* \hat{\eta}_q + V_{qp}^* \hat{\eta}_q^\dagger \right) \quad (2.4)$$

To preserve the fermionic anti-commutation relations, we require

$$\begin{aligned} U^\dagger U + V^\dagger V &= 1, & UU^\dagger + V^* V^T &= 1 \\ U^T V + V^T U &= 0, & UV^\dagger + V^* U^T &= 0. \end{aligned} \quad (2.5)$$

We denote a quasi-particle Slater determinant as

$$|\Phi\rangle = \prod_p \hat{\beta}_p |0\rangle \quad (2.6)$$

where $|0\rangle$ is true vacuum. If we assume there exists a one-to-one mapping between $|\Phi\rangle$ and a reduced one-body density \mathcal{R} (N -representability [37]), then define a generalized reduced

one-body density in quasi-particle vacuum as

$$\mathcal{R} = \begin{pmatrix} \rho & \kappa \\ -\kappa^* & 1 - \rho^* \end{pmatrix} \quad (2.7)$$

where the particle density ρ and pairing density κ are

$$\rho_{pq} = \langle \Phi | \overset{\square}{\eta}_p^\dagger \eta_q | \Phi \rangle = (VV^\dagger)_{pq}, \quad \kappa_{pq} = \langle \Phi | \overset{\square}{\eta}_p^\dagger | \Phi \rangle \eta_q = (UV^\dagger)_{pq}. \quad (2.8)$$

The Wick contraction $\overset{\square}{\dots}$ indicates a contraction with respect to quasi-particle vacuum. To ensure \mathcal{R} is a density operator, we enforce the idempotent condition $\mathcal{R}^2 = \mathcal{R}$. The minimization is equivalently taken over generalized densities,

$$\min_{|\tilde{\Phi}\rangle} E[|\tilde{\Phi}\rangle] = \min_{\tilde{\mathcal{R}}} E[\tilde{\mathcal{R}}] - \text{Tr}(\Lambda(\tilde{\mathcal{R}}^2 - \tilde{\mathcal{R}})) \quad (2.9)$$

where Λ is a matrix of Lagrange multipliers. Proof of the minimization Eq. (2.9) over N -representable densities is formalized by Levy and Lieb's constrained search [57–60].

Rather than representing the total energy $E[\mathcal{R}]$ in terms of a Hamiltonian, we instead represent it as an integral over a scalar function of reduced one-body densities and currents called an energy density functional (EDF) \mathcal{E} . This approach is the core of nuclear density functional theory (DFT) and is used in our non-relativistic mean-field description of fission. We overview the essential results from DFT used in this dissertation.

The foundations of DFT were derived by Hohenberg and Kohn in their seminal paper [61] for electronic systems. Their results can be summarized by two theorems:

Theorem 1. *There exists a mapping between a ground state density of the many-body system and a one-body potential. This map is unique up to an additive constant and defines a set of what are called V -representable densities for which this map exists.*

Theorem 2. *There exists a universal EDF of densities and currents such that it's global minimum corresponds to the exact ground state energy of the many-body system.*

The proofs can be found in Ref. [37]. Progress towards formal extensions of the Hohenberg-Kohn theorem for self-bound intrinsic systems have been made [62–65] and motivate using DFT for nuclear systems.

Minimizing the energy with respect to \mathcal{R} leads to the Hartree-Fock-Bogoliubov (HFB) mean-field equations

$$\mathcal{H} \begin{pmatrix} U_{pk} \\ V_{pk} \end{pmatrix} = E_k \begin{pmatrix} U_{pk} \\ V_{pk} \end{pmatrix} \quad (2.10)$$

where the HFB matrix \mathcal{H} is

$$\mathcal{H} = \begin{pmatrix} f & \Delta \\ -\Delta^* & -f^* \end{pmatrix}. \quad (2.11)$$

The matrix elements of \mathcal{H} are given by

$$f_{pq} = \frac{\partial E}{\partial \rho_{pq}}, \quad \Delta_{pq} = \frac{\partial E}{\partial \kappa_{pq}^*} \quad (2.12)$$

where f is the Fock matrix (also called the particle-hole Hamiltonian), and Δ is the pairing field.

The HFB equations have three crucial features. First, in the presence of pairing correla-

tions, \mathcal{H} does not commute with the particle-hole number operator $\hat{N} = \sum_p \hat{\eta}_p^\dagger \hat{\eta}_p$. Solutions to the HFB equations do not have definite particle number. This is discussed in more detail in section 2.3.1. Second, the HFB matrix admits conjugate solutions with eigenvalues $-E_k$. These are related to the positive energy solutions through complex conjugation of the eigenvectors in Eq. (2.10). It is conventional to solve for positive eigenvalues and eigenvectors and assume the negative eigenstates are occupied. Third, the spectrum of the HFB matrix is unbounded above and below. Due to the unbounded spectrum, physical bound states of the HFB matrix have some coupling to the quasi-particle continuum which must be treated carefully in numerical calculations. Typical methods for treating the quasi-particle continuum include discretization using vanishing Dirichlet boundary conditions in coordinate space [66–68], discretization by expanding solutions in a harmonic oscillator basis [69, 70], or treating the continuum in the Berggren basis (Gamow-HFB) [71].

The construction of the HFB matrix requires a model of nuclear interactions, as the Hohenberg-Kohn theorem only proves the existence of a universal EDF. The form of the universal functional is currently unknown. Much work has been done to derive EDFs from effective theories of nucleon-nucleon interactions [72–78]. Alternatively, the form of the EDF can be postulated, usually guided by symmetries or phenomenology. A few examples of postulated EDFs are the Skyrme-type [79–84], Gogny [85, 86], SeaLL1 [87], and Fayans [88, 89] functionals. In this dissertation we only consider Skyrme and Gogny EDFs. Phenomenological EDFs based on relativistic meson exchange models are discussed in section 5.

2.2 Structure of a Nuclear Energy Density Functional

The structure of the EDF depends on whether the nuclear system contains an odd or even number of particles. In odd nucleon systems, time-reversal symmetry is broken and time-odd parts of the EDF must be included [34, 90]. The classification based on time-reversal symmetry is used to identify parts of the EDF that are present for all nuclear systems. We only focus on nuclei with an even number of protons and neutrons due to the additional difficulties posed by odd nucleon systems [91, 92]. In the following, we overview the construction of EDFs for even-even systems.

Assume single quasi-particle states of the form $|p\rangle \in \mathcal{F}$ where p is the occupation quantum number. We label spin and isospin projections with s and τ ($\tau_n = -1/2$ for neutrons and $\tau_p = 1/2$ for protons) respectively. The position space representation of the reduced one-body particle density operator on \mathcal{F} has the form:

$$\begin{aligned} \hat{\rho}(\vec{r}_1, \vec{r}_2) &= \sum_{ij} \rho_{ij}(\vec{r}_1, \vec{r}_2) \sigma_i \otimes \tau_j \\ &= \frac{1}{4} \rho_0(\vec{r}_1, \vec{r}_2) \hat{I}_s \otimes \hat{I}_\tau + \frac{1}{4} \rho_1(\vec{r}_1, \vec{r}_2) \hat{I}_s \otimes \vec{\tau} + \frac{1}{4} \vec{s}_0(\vec{r}_1, \vec{r}_2) \vec{\sigma} \otimes \hat{I}_\tau + \frac{1}{4} \vec{s}_1(\vec{r}_1, \vec{r}_2) \vec{\sigma} \otimes \vec{\tau} \end{aligned} \quad (2.13)$$

where $\vec{\sigma}$ and $\vec{\tau}$ are the vector of Pauli matrices for spin and isotopic spin respectively [93]. Define isoscalar (labeled with $t = 0$) and isovector (labeled with $t = 1$) particle densities,

$$\rho_0(\vec{r}_1, \vec{r}_2) = \sum_{s_1 s_2 \tau = -1/2}^{1/2} \rho(\vec{r}_1, s_1, \tau, \vec{r}_2, s_2, \tau) \quad (2.14)$$

$$\rho_1(\vec{r}_1, \vec{r}_2) = \sum_{s_1 s_2 \tau = -1/2}^{1/2} (-1)^{2\tau+1} \rho(\vec{r}_1, s_1, \tau, \vec{r}_2, s_2, \tau) \quad (2.15)$$

and the isoscalar and isovector spin densities,

$$\vec{s}_0(\vec{r}_1, \vec{r}_2) = \sum_{s_1 s_2 \tau = -1/2}^{1/2} \rho(\vec{r}_1, s_1, \tau, \vec{r}_2, s_2, \tau) \langle s_1 | \vec{\sigma} | s_2 \rangle \quad (2.16)$$

$$\vec{s}_1(\vec{r}_1, \vec{r}_2) = \sum_{s_1 s_2 \tau_1 \tau_2 = -1/2}^{1/2} \rho(\vec{r}_1, s_1, \tau_1, \vec{r}_2, s_2, \tau_2) \langle s_1 | \vec{\sigma} | s_2 \rangle \cdot \langle \tau_1 | \vec{\tau} | \tau_2 \rangle \quad (2.17)$$

respectively. By taking traces of the reduced one-body densities, we define local densities and their derivatives. Relevant local densities and currents classified by their symmetry under time-reversal and their first and second derivatives are shown below

1. Time-even:

$$\rho_t(\vec{r}) = \int d^3 r' \delta^3(\vec{r}' - \vec{r}) \rho_t(\vec{r}, \vec{r}') \quad (\text{particle density}) \quad (2.18)$$

$$\tau_t(\vec{r}) = \int d^3 r' \delta^3(\vec{r}' - \vec{r}) \left(\vec{\nabla} \cdot \vec{\nabla}' \rho(\vec{r}, \vec{r}') \right) \quad (\text{kinetic density}) \quad (2.19)$$

$$J_{t,ij}(\vec{r}) = -\frac{i}{2} \int d^3 r' \delta^3(\vec{r}' - \vec{r}) \left(\nabla_i - \nabla'_j \right) s_j(\vec{r}, \vec{r}') \quad (\text{spin current density}) \quad (2.20)$$

2. Time-odd:

$$\vec{s}_t(\vec{r}) = \int d^3 r' \delta^3(\vec{r}' - \vec{r}) \vec{s}_t(\vec{r}, \vec{r}') \quad (\text{spin density}) \quad (2.21)$$

$$\vec{\mathcal{S}}_t(\vec{r}) = \int d^3 r' \delta^3(\vec{r}' - \vec{r}) \left(\vec{\nabla} \cdot \vec{\nabla}' \vec{s}_t(\vec{r}, \vec{r}') \right) \quad (\text{kinetic spin density}) \quad (2.22)$$

$$j_{t,i}(\vec{r}) = \int d^3 r' \delta^3(\vec{r}' - \vec{r}) \left(\nabla_i - \nabla'_j \right) \rho_t(\vec{r}, \vec{r}') \quad (\text{current density}). \quad (2.23)$$

Similar operators and densities can be defined with the replacement $\rho \rightarrow \kappa$. To build time-

even pairing EDFs, it is convenient to define a time-even form of the pairing densities [66],

$$\tilde{\rho}(\vec{r}_1, s_1, \tau_1, \vec{r}_2, s_2, \tau_2) = -2s_2\kappa(\vec{r}_1, s_1, \tau_1, \vec{r}_2, -s_2, \tau_2). \quad (2.24)$$

We use this form of the pairing density.

EDFs in quasi-particle vacuum have the general form [93],

$$\mathcal{E} = \mathcal{E}_{\text{kin}}[\rho] + \mathcal{E}_{\text{c.o.m}}[\rho] + \mathcal{E}_{\text{ph}}[\rho] + \mathcal{E}_{\text{pp}}[\rho, \kappa, \kappa^*] + \mathcal{E}_{\text{e.m}}[\rho] \quad (2.25)$$

where $\mathcal{E}_{\text{kin}}[\rho]$ is the kinetic energy density, $\mathcal{E}_{\text{c.o.m}}[\rho]$ is the center of mass functional, $\mathcal{E}_{\text{ph}}[\rho]$ is the particle-hole (also called the potential) term, $\mathcal{E}_{\text{pp}}[\rho, \kappa, \kappa^*]$ is the particle-particle (also called the pairing) term, and $\mathcal{E}_{\text{e.m}}[\rho]$ is the electromagnetic density. The kinetic energy functional is

$$\mathcal{E}_{\text{kin}}[\rho] = \sum_{t=0,1} \frac{\hbar^2}{2m_p} \tau_t[\rho] \quad (2.26)$$

where $t = 0, 1$ denote isoscalar and isovector respectively. We use the bare nucleon mass expression from Ref. [81],

$$\frac{\hbar^2}{2m_p} = 20.735530 \text{ MeV fm}^2. \quad (2.27)$$

The kinetic term is often paired with a center-of-mass density $\mathcal{E}_{\text{c.o.m}}[\rho]$ to correct for translational symmetry breaking by the mean-field in the intrinsic system. Rather than restoring

the symmetry completely, a simple approximation that is often used is [90]

$$\mathcal{E}_{\text{c.o.m.}}[\rho] = - \sum_{t=0,1} \frac{1}{2m_p A} \tau_t[\rho]. \quad (2.28)$$

This correction is not included in all EDFs and must be included in the calibration. The particle number is not additive in the exact center of mass correction and this poses a conceptual problem when modeling fission. Properly computing this relative contribution is difficult, as it reflects the entanglement between prefragments [94]. Because of these difficulties, the EDFs we consider do not include the center of mass correction.

The electromagnetic term contains the direct (Hartree) and exchange (Fock) term arising from the anti-symmetric nature of fermions,

$$\mathcal{E}_{\text{e.m.}}[\rho] = \mathcal{E}_{\text{e.m.}}^D[\rho] + \mathcal{E}_{\text{e.m.}}^E[\rho]. \quad (2.29)$$

The direct term is the classical Coulomb interaction,

$$\mathcal{E}_{\text{e.m.}}^D[\rho] = \frac{e^2}{2} \int d^3r' \frac{\rho_{\tau_p}(\vec{r}) \rho_{\tau_p}(\vec{r}')}{|\vec{r} - \vec{r}'|} \quad (2.30)$$

where ρ_{τ_p} is the local proton particle density. In numerical calculations, a singularity free representation proposed by Vautherin [95] or Dobaczewski et al. [67] is used. The time-even exchange term is [93]

$$\mathcal{E}_{\text{e.m.}}^E[\rho] = - \frac{e^2}{2} \int d^3r' \frac{\rho_{\tau_p}(\vec{r}, \vec{r}') \rho_{\tau_p}(\vec{r}', \vec{r})}{|\vec{r} - \vec{r}'|}. \quad (2.31)$$

The exchange term is more computationally expensive since it depends on the reduced one-

body density. While there exist numerical methods to compute this [96–98], the Slater approximation [99],

$$\mathcal{E}_{\text{e.m.}}^E[\rho] \approx -\frac{3e^2}{4} \left(\frac{3}{\pi}\right)^{1/3} \rho_{\tau p}^{4/3}(\vec{r}) \quad (2.32)$$

is often deployed due to its simplicity. The total difference between the Slater approximation and the exact expression of the exchange term in the calculation of nuclear ground states is on the order of 1 MeV [100]. We use the Slater approximation for all Skyrme calculations. We ignore pairing contributions to $\mathcal{E}_{\text{e.m.}}$ as it is ~ 100 keV [93, 100].

The particle-hole (ph) and particle-particle (pp) densities represent the nuclear interaction between independent particles and particle pairs respectively. Combinations of the basic densities in Eqs. (2.18)-(2.23) are multiplied by parameters optimized to reproduce experimental data such as nuclear masses, isomers, and nuclear matter properties [82]. The optimization depends on the training data selected as well the method used to treat broken symmetries of the nuclear system. Extrapolative predictions beyond the training data to all nuclei is an active field of research [28, 101, 102]. The Skyrme and the Gogny class of EDFs have been used to extrapolate fission predictions to actinides and trans-actinides and we briefly overview each one.

2.2.1 The Skyrme Functional

The original Skyrme EDF, proposed by Skyrme [103–105], is derived by calculating matrix elements of a phenomenological two-body contact potential. Modern versions of the Skyrme EDF are derived from the density matrix expansion proposed by Negele and Vautherin [106,

107] and have the form

$$\mathcal{E}_{\text{Sk}} = \mathcal{E}_{\text{kin}}[\rho] + \mathcal{E}_{\text{c.o.m}}[\rho] + \mathcal{E}_{\text{Sk,ph}}[\rho] + \mathcal{E}_{\text{Sk,pp}}[\rho, \kappa, \kappa^*] + \mathcal{E}_{\text{e.m}}[\rho]. \quad (2.33)$$

where $\mathcal{E}_{\text{c.o.m}}[\rho]$ maybe included depending on the calibration. The particle-hole sector contains time-even and time-odd isoscalar and isovector parts,

$$\mathcal{E}_{\text{Sk,ph}}[\rho] = \sum_{t=0,1} \left(\mathcal{E}_{t,\text{ph}}^{(\text{even})}[\rho] + \mathcal{E}_{t,\text{ph}}^{(\text{odd})}[\rho] \right) \quad (2.34)$$

The time-even part contains bilinear combinations of the densities and currents (from Eqs. (2.18)-(2.20)),

$$\mathcal{E}_{t,\text{ph}}^{(\text{even})} = C_t^{\rho\rho}[\rho]\rho_t^2 + C_t^{\rho\tau} \rho_t \tau_t + C_t^{J^2} J_{i,j,t} J_{i,j,t} + C_t^{\rho\Delta\rho} \rho_t \vec{\nabla}^2 \rho_t + C_t^{\rho\nabla J} (\varepsilon_{ijk} \partial_k J_{i,j,t}) \rho_t \quad (2.35)$$

where we suppress the spatial indices. Since we are only considering even-even nuclei, $\mathcal{E}_{t,\text{ph}}^{(\text{odd})} = 0$. The C coefficients are real numbers with the exception of

$$C_t^{\rho\rho}[\rho] = C_{t0}^{\rho\rho} + C_{tD}^{\rho\rho} \rho^\alpha \quad (2.36)$$

which has density dependence. $C_{t0}^{\rho\rho}[\rho]$ is an effective density dependent coupling meant to reproduce renormalized n -body forces. The particle-hole sector contains 13 tunable parameters,

$$\{C_{t0}^{\rho\rho}, C_{tD}^{\rho\rho}, C_t^{\rho\tau}, C_t^{J^2}, C_t^{\rho\Delta\rho}, C_t^{\rho\nabla J}, \alpha\} \quad (2.37)$$

for $t = 0, 1$. Relations between the parameter set in Eq. (2.37) and Skyrme interaction couplings are shown in Ref. [108]. In the pairing sector, one can define a similar density matrix expansion. A common simple zero-range pairing force of the form,

$$\mathcal{E}_{\text{Sk},pp}[\rho, \kappa, \kappa^*] = \sum_{\tau=-1/2}^{1/2} V_{\tau} \left(1 - \frac{\rho_0(\vec{r})}{\rho_{\text{ref}}}\right) \tilde{\rho}_{\tau}^2(\vec{r}) \quad (2.38)$$

where V_{τ} are fit parameters, and $\tilde{\rho}(\vec{r})$ is the time-even pairing density from Eq. (2.24) [90, 109]. This form of the pairing interaction is inspired by the t_0 and t_3 terms from the Skyrme potential [105]. The reference density ρ_{ref} classifies the type of pairing interaction. We use $\rho_{\text{ref}} = 0.16 \text{ fm}^3$ corresponding to “surface pairing”. Other values of ρ_{ref} have also been used in various calibrations of the Skyrme EDF [110]. The pairing functional in Eq. (2.38) is used in the UNEDF parameterization of the Skyrme functional [82, 111]. Other forms of the Skyrme functional such as the SkM* functional use a BCS-type of pairing functional [95]

$$\mathcal{E}_{\text{Sk-BCS},pp} = -2G \sum_i (n_i(1 - n_i))^{1/2} \quad (2.39)$$

where n_i are the occupation probabilities of state i and G is a fit parameter. Due to the zero-range behavior, both of the pairing functionals contain ultraviolet divergences. This requires a regularization scheme to render the pairing sector finite [67, 112].

Since the original Skyrme interaction was published, there have been many parameterizations of the Skyrme EDF published with different calibrations, treatments of pairing, and densities included (see Ref. [110] for a review of the various Skyrme EDF parameterizations). In this work, we use the UNEDF1_{HFB} [111] and SkM* [83] functionals. These are both calibrated with fission data. UNEDF1_{HFB} was fit including fission isomer excitation

energies of selected actinides and SkM* was fit to reproduce fission barrier heights of ^{240}Pu .

2.2.2 The Gogny Functional

The Gogny interaction combines the finite-range potentials from the phenomenological Brink and Boeker force [113] and the contact density dependence from the Skyrme interaction. The form of the Gogny two-body interaction is [85]

$$\begin{aligned}
V_{\text{Gogny}}(\vec{r}_1, \vec{r}_2) = & \sum_{j=1}^2 e^{-\frac{|\vec{r}_1 - \vec{r}_2|^2}{\mu_j^2}} \left(W_j + B_j \hat{P}_\sigma - H_j \hat{P}_\tau - M_j \hat{P}_\sigma \hat{P}_\tau \right) \\
& + t_3 (1 + x_0 \hat{P}_\sigma) \delta^3(\vec{r}_1 - \vec{r}_2) \rho^\alpha \left(\frac{\vec{r}_1 + \vec{r}_2}{2} \right) \\
& + i \left(W_{LS} (\vec{\sigma}_1 + \vec{\sigma}_2) \cdot \vec{k}^\dagger \right) \times \left(\delta^3(\vec{r}_1 - \vec{r}_2) \vec{k} \right)
\end{aligned} \tag{2.40}$$

where $\hat{P}_\sigma = \frac{1}{2}(I_2 + \vec{\sigma}_1 \cdot \vec{\sigma}_2)$ and $\hat{P}_\tau = \frac{1}{2}(I_2 + \vec{\tau}_1 \cdot \vec{\tau}_2)$ are the spin and isotopic spin exchange operators respectively and \vec{k} is the relative momentum operator,

$$\vec{k} = \frac{1}{2i} (\vec{\nabla} - \vec{\nabla}'). \tag{2.41}$$

Note that the conjugate momentum \vec{k}^\dagger acts on states to the left. The Gogny functional contains 14 fit parameters,

$$\{\mu_j, W_j, B_j, H_j, M_j, t_3, x_0, \alpha, W_{LS}\} \tag{2.42}$$

for $j = 0, 1$. The pairing sector is treated using the contact pairing from Eq. (2.38). Similar to the Skyrme EDF, there exist many parameterizations of the Gogny interaction [114]. The D1S parameterization [115] was fit to reproduce the barrier height of ^{240}Pu . This parameterization has been used to study fission of heavy and superheavy nuclei [114] and

this is the parameterization we use.

2.3 Symmetries and Constraints

When defining a mean-field state by minimizing the total energy functional E , one must decide to preserve symmetries before performing the energy minimization or restore them afterwards. Allowing the minimization to consider states that break symmetries may result in a lower mean-field energy resulting in an *unrestricted* HF or HFB vacuum, however, this state may not represent the physics of interest. Alternatively, enforcing symmetries results in a *restricted* HF or HFB vacuum which is not guaranteed to result in the global minimum energy configuration. This situation is called the mean-field theory "symmetry dilemma" in the literature [116–118].

The choice to preserve or break symmetries depends on the problem under consideration. There are two main strategies to treat the "symmetry dilemma". First, are symmetry restoration techniques. In this approach, an unrestricted minimization is performed, then the Kohn-Sham solution is projected onto the subspace where the symmetry is preserved. Second, is to introduce constraints to the energy minimization to preserve the symmetries relevant to the problem of interest. The EDF calibration must take into account how the symmetries are treated and must be used consistently in applications. We take the second approach and introduce constraints linearly by method of Lagrange multipliers. We overview the relevant symmetries and methods used to constrain them.

2.3.1 Particle Number and Pairing Fluctuations

Quasi-particle vacuum does not preserve particle number. This poses a problem when describing systems with definite numbers of protons and neutrons. Exact restoration of particle number can be done by projecting the Kohn-Sham solution onto a subspace with definite

proton and neutron numbers using the projection operator,

$$\hat{P}_{N_\tau} = \frac{1}{2\pi} \int_0^{2\pi} d\phi e^{i\phi(\hat{N}_\tau - N_\tau)} \quad (2.43)$$

where N_τ is the fixed number of protons ($\tau = 1/2$) or neutrons ($\tau = -1/2$). This approach is computationally expensive and has a small effect on the ground state properties of even-even nuclei [119].

A more practical and computationally cheaper alternative is to constrain the vacuum expectation value of the particle number operator for proton and neutron separately by introducing linear constraints,

$$L[\mathcal{R}, \lambda_\tau] = E[\mathcal{R}] - \sum_{\tau=-1/2}^{1/2} \lambda_\tau (\langle \hat{N}_\tau \rangle - N_\tau), \quad \langle \hat{N}_\tau \rangle = \langle \Phi | \hat{N}_\tau | \Phi \rangle \quad (2.44)$$

where λ_τ are Lagrange multipliers for protons and neutrons. λ_τ are interpreted as the chemical potentials defining the Fermi surface for protons and neutrons and must be calculated with the HFB equations simultaneously. Only solutions with $\lambda_\tau < 0$ are considered. These solutions correspond to localized HFB orbitals which are interpreted as bound state solutions to the HFB equations. Since the HFB matrix is unbounded below and above, eigenvalues with $E_{k,\tau} \notin [-|\lambda_\tau|, |\lambda_\tau|]$ are interpreted to be elements of the discretized continuum spectrum.

However, due to the presence of the pairing interaction, the expectation value of \hat{N}_τ^2 is not negligible in nuclei based on empirical evidence [120, 121]. The Lipkin-Nogami (LN)

method adds a constrain on \hat{N}_τ^2 [122],

$$L[\mathcal{R}, \lambda_\tau] = E[\mathcal{R}] - \sum_{\tau=-1/2}^{1/2} \lambda_\tau (\langle \hat{N}_\tau \rangle - N_\tau) - \sum_{\tau=-1/2}^{1/2} \lambda_{2\tau} \langle \hat{N}_\tau^2 \rangle \quad (2.45)$$

Constraining \hat{N}_τ^2 has been shown to prevent the collapse of the pairing energy gap [123]. The UNEDF1 functional [94] was calibrated with the Lipkin-Nogami procedure while UNEDF1_{HFB} [111] was not.

Pairing fluctuations about the HFB solution are directly related to the second moment of the particle number operator and the pairing gap [34, 124, 125]. The influence of pairing fluctuations on fission was explored using microscopic-macroscopic models [126]. Using DFT, Sadhukhan et. al [127] added an additional constraint on the second moment of the particle number operator to study pairing fluctuations,

$$L[\mathcal{R}, \lambda_\tau] = E[\mathcal{R}] - \sum_{\tau=-1/2}^{1/2} \lambda_\tau (\hat{N}_\tau - \langle \hat{N}_\tau \rangle) - \sum_{\tau=-1/2}^{1/2} \lambda_{2\tau} (\hat{N}_\tau^2 - \langle \hat{N}_\tau \rangle^2) \quad (2.46)$$

In Ref. [127], the Lagrange multipliers $\lambda_{2\tau}$ were treated as coordinates parameterizing the energy gap as nuclei fissioned. They showed that pairing fluctuations are not negligible in the calculations of fission lifetimes [127]. This is again investigated and discussed in Ch. 3.

2.3.2 Nuclear Deformation

Motivated by the liquid drop model proposed by Bohr and Wheeler [5], we represent the nuclear shape with constraints on multipole operators. The multipole operators in the intrinsic frame have the form

$$\hat{Q}_{\mu\nu} = \hat{r}^\mu \hat{Y}_{\mu\nu}^* \quad (2.47)$$

where \hat{r} is the radial position operator and $\hat{Y}_{\mu\nu}^*$ are scalar spherical harmonic operators. If the nuclear surface is represented as a smooth parametric function, it can be represented with a multipole expansion. Near scission, the surface develops non-smooth characteristics and the expansion begins to diverge. We are only interested fission before scission and we are justified to use multipole moments to parameterize the shape of the nucleus.

We solve the HFB equations adding constraints on various $\hat{Q}_{\mu\nu}$ operators to a set of expectation values,

$$L[\mathcal{R}, \lambda_{\mu\nu}] = E[\mathcal{R}] - \sum_{\mu\nu} \lambda_{\mu\nu} (\langle \hat{Q}_{\mu\nu} \rangle - Q_{\mu\nu}) \quad (2.48)$$

In our studies, we restrict to axially symmetric deformations, which implies $\langle \hat{Q}_{\mu\nu} \rangle = 0$ for all $\nu \neq 0$. It has been shown that constraining \hat{Q}_{22} has an influence on fission lifetimes near the ground state configuration [128] however we ignore this moment to reduce computational cost. Since the nuclear shapes before scission are compact, we only consider moments with $\mu \leq 4$ as these moments provide an adequate number of degrees of freedom to describe most compact deformations before scission. $\hat{Q}_{00} = \hat{N}$ is being constrained by the particle numbers for protons and neutrons separately. \hat{Q}_{10} is the dipole moment operator corresponding to the center of mass coordinate of the nucleus. The expectation of this operator is always constrained to 0 in our calculations. \hat{Q}_{20} is the quadrupole moment which parametrizes the elongation of the nuclear surface, \hat{Q}_{30} is the octupole moment which controls mass asymmetry of the nucleus, and \hat{Q}_{40} controls the geometry of the neck region as the nucleus deforms into two fragments [91].

2.4 Numerical Solution of the HFB Equations

To solve the non-linear HFB eigenvalue equations Eq. (2.10), we use the self-consistent mean-field (SCMF) method implemented two different code bases:

1. HFBTHOv3 [129] is a Fortran 95 code that solves the HFB equations by self-consistent iteration until a fixed point solution is reached. This code uses cylindrical coordinates and assumes axial symmetry. A harmonic oscillator or a transformed harmonic oscillator [130] basis is used. The number of basis states is parameterized by the number of harmonic oscillator shells. Time-odd terms are ignored. The SCMF method is implemented using a Broyden method [131, 132] to minimize the total energy and solve constraint equations. Solutions to a single particle Woods-Saxon Schrödinger equation are used for initialization. Particle number and multipole expectation constraints are introduced linearly. Possible multipole constraints up to Q_{80} are included with the possibility to leave multipole moments unrestricted to be optimized over. MPI and OpenMP paradigms are used to parallelize calculations of potential energy surfaces.
2. HFBaxial [133] is a Fortran code that uses a gradient descent method to minimize the energy with constraints in cylindrical coordinates in the harmonic oscillator basis. Similar to HFBTHOv3, this code ignores time-odd terms and considers only axial shapes. Constraints on the multipole moments and the number operators are introduced in a similar way as HFBTHOv3. MPI and OpenMP paradigms are also used.

Chapter 3. Spontaneous Nuclear Fission

3.1 Nuclear Fission as an Adiabatic Process

Assuming a quasi-particle vacuum, time-dependence is often introduced by the Dirac-Frenkel-McLachlan (DFM) variational principle [134, 135]:

$$S_{\text{DFM}}[|\Phi\rangle] = \langle \Phi(t) | i\partial_t - \hat{H} | \Phi(t) \rangle \quad (3.1)$$

Taking a variation with respect to $\langle \Phi(t) |$ leads to the time-dependent HFB (TDHFB) equations [136]. If one assumes $|\Psi(t)\rangle$ is normalized for all t , the action S_{DFM} is real. Other time-dependent variational principles have also been used (see [55] and references therein). The correspondence between a time-dependent many-body state and a time-dependent non-interacting system is proved by the Runge-Gross and Van Leeuwen theorems (see [38] for discussion about these theorems). Under mild assumptions, these theorems guarantee the existence of a non-interacting system that can reproduce the exact time-dependent reduced one-body densities [38].

For any unstable quantum system, quantum tunneling is often used to account for decay processes such as spontaneous fission [91, 137, 138]. However, it is unclear if the tunneling physics needed to describe fission decays is contained in the action functional Eq. (3.1). Restrictions on the normalization of $|\Phi(t)\rangle$ or the domain of S_{DFM} seem to obfuscate tunneling physics. For example, the TDHFB equation predicts a single deterministic history and is interpreted as a classical equation of motion that cannot predict tunneling. Because of this, TDHFB does not admit solutions representing tunneling decay. Nevertheless, one can parameterize $|\tilde{\Phi}\rangle$ to facilitate tunneling through a finite set of real, time-dependent collective

coordinates $\{q_i(t)\}_{i=1}^{N_q}$ where N_q is the total number of collective coordinates. We assume there exists a reparametrized trajectory

$$|\tilde{\Phi}(t)\rangle = |\tilde{\Phi}(\vec{q}(t), \vec{\xi})\rangle \in \mathcal{F} \quad (3.2)$$

that smoothly depends on time through $\vec{q}(t)$. The coordinates $\vec{\xi}$ are intrinsic variables representing single particle motion and we assume they are separable from the collective coordinates (see Ref. [139]). We will ignore the intrinsic variables throughout this chapter.

Assuming N-representability, this trajectory is equivalently represented by a generalized density matrix, $\mathcal{R}(\vec{q}(t))$:

$$\mathcal{R}(\vec{q}(t)) = \begin{pmatrix} \langle \tilde{\Phi}(\vec{q}(t)) | \bar{N}[\hat{\beta}_m^\dagger \hat{\beta}_n] | \tilde{\Phi}(\vec{q}(t)) \rangle & \langle \tilde{\Phi}(\vec{q}(t)) | \bar{N}[\hat{\beta}_r \hat{\beta}_s] | \tilde{\Phi}(\vec{q}(t)) \rangle \\ \langle \tilde{\Phi}(\vec{q}(t)) | \bar{N}[\hat{\beta}_m^\dagger \hat{\beta}_n^\dagger] | \tilde{\Phi}(\vec{q}(t)) \rangle & \langle \tilde{\Phi}(\vec{q}(t)) | \bar{N}[\hat{\beta}_r \hat{\beta}_s^\dagger] | \tilde{\Phi}(\vec{q}(t)) \rangle \end{pmatrix} \quad (3.3)$$

where $\bar{N}[\dots]$ indicates normal ordering with respect to quasi-particle vacuum. The set of states $\{|\tilde{\Phi}(\vec{q}(t))\rangle\}$ do not necessarily span a linear space and the superposition principle is not valid along the trajectory [140, 141]. Studying the tunneling trajectory is non-trivial since it evolves according to a nonlinear Hamiltonian (see Refs. [142–145] for nonlinear tunneling examples in single particle quantum mechanics). Instead of using the DFM action to define the fission trajectory, let us suppose there exists a generalized density $\mathcal{R}^{(0)}(\vec{q}(t))$ that is the solution to the constrained HFB equations defined by,

$$\mathcal{R}^{(0)}(\vec{q}(t)) = \arg \min_{\tilde{\mathcal{R}}} \left(E[\tilde{\mathcal{R}}] - \sum_{\tau=-1/2}^{1/2} \lambda_\tau (\langle \hat{N}_\tau \rangle - N_\tau) - \sum_{\mu} \lambda_\mu (\langle \hat{q}_\mu(t) \rangle - q_\mu(t)) \right) \quad (3.4)$$

for all t . Eq. (3.4) defines a set of instantaneously diagonal density matrices reparameterized

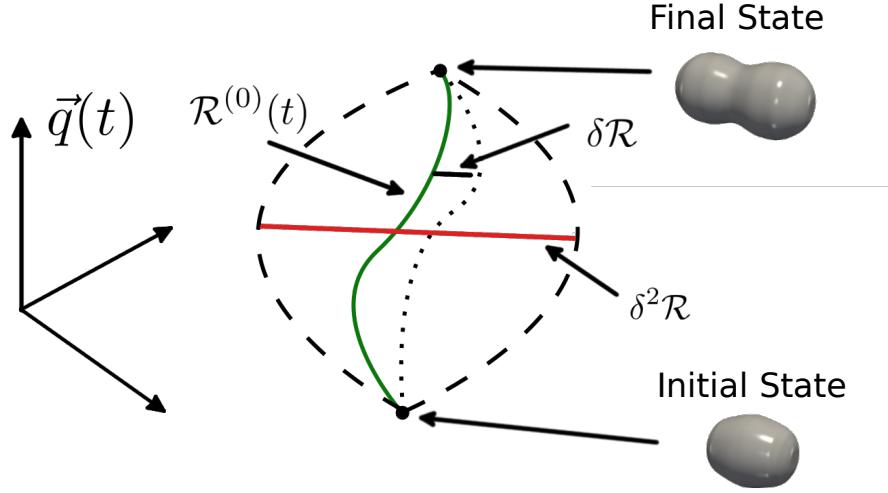


Figure 3.1: Schematic representation of the time-dependent fission trajectory in the many-body manifold \mathcal{F} . The green curve represents the adiabatic density trajectory $\mathcal{R}^{(0)}(t)$. The curvature about $\mathcal{R}^{(0)}(t)$ is schematically represented by the dashed lines. The local variations in the pathway $\delta\mathcal{R}$ are represented by the solid black line connecting to an alternate pathway denoted by the dotted line. The $\delta^2\mathcal{R}$ is schematically represented by the width between the dashed lines.

by $\vec{q}(t)$. Since the solution set $\mathcal{R}^{(0)}(t)$ corresponds to a minimum energy configuration of a nucleus for all t , we call it an *adiabatic* fission trajectory. Along this pathway, $\mathcal{R}^{(0)}(\vec{q}(t))$ is,

$$\mathcal{R}^{(0)}(\vec{q}(t)) = \begin{pmatrix} \langle \tilde{\Phi}(\vec{q}(t)) | \hat{\beta}_m^\dagger \hat{\beta}_n | \Phi(\vec{q}(t)) \rangle & \langle \tilde{\Phi}(\vec{q}(t)) | \hat{\beta}_r \hat{\beta}_s | \Phi(\vec{q}(t)) \rangle \\ \langle \tilde{\Phi}(\vec{q}(t)) | \hat{\beta}_m^\dagger \hat{\beta}_n^\dagger | \Phi(\vec{q}(t)) \rangle & \langle \tilde{\Phi}(\vec{q}(t)) | \hat{\beta}_r \hat{\beta}_s^\dagger | \Phi(\vec{q}(t)) \rangle \end{pmatrix} = \begin{pmatrix} 0 & 0 \\ 0 & I \end{pmatrix} \quad (3.5)$$

where I is the identity matrix. Assuming $|\tilde{\Phi}\rangle$ and $|\Phi\rangle$ are not orthogonal, we can relate them with the quasi-particle Thouless theorem [34]:

$$|\tilde{\Phi}(\vec{q}(t))\rangle = \exp\left(\frac{1}{2} \sum_{kk'} Z_{kk'}(t) \hat{\beta}_k^\dagger \hat{\beta}_{k'}^\dagger\right) |\Phi(\vec{q}(t))\rangle. \quad (3.6)$$

Expanding $\mathcal{R}(t)$ about the adiabatic pathway $\mathcal{R}^{(0)}(t)$ to second order in Z and using Wick's

theorem with respect to quasi-particle vacuum yields,

$$\mathcal{R}(\vec{q}(t)) = \mathcal{R}^{(0)}(\vec{q}(t)) + \begin{pmatrix} -Z^\dagger(t)Z(t) & -Z(t) \\ Z^\dagger(t) & Z^\dagger(t)Z(t) \end{pmatrix} \quad (3.7)$$

Figure 3.1 schematically shows the expansion of $\mathcal{R}(t)$ about $\mathcal{R}^{(0)}(t)$ in the full many-body manifold \mathcal{F} . The generalized density representing the fissioning nucleus starts in an initial compact shape and deforms into a final configuration state. $\delta\mathcal{R}$ and $\delta^2\mathcal{R}$ represent the local variations and curvature about $\mathcal{R}^{(0)}(t)$ respectively.

To study the curvature of the energy functional E along the trajectory due to the variations in $\mathcal{R}(t)$, we expand it about the adiabatic fission pathway to second order in $\mathcal{R}(t)$,

$$E[\mathcal{R}] \approx E[\mathcal{R}^{(0)}] + (\mathcal{R} - \mathcal{R}^{(0)})_{pq} \frac{\partial E}{\partial \mathcal{R}_{pq}} + (\mathcal{R} - \mathcal{R}^{(0)})_{pq} (\mathcal{R} - \mathcal{R}^{(0)})_{rs} \frac{\partial^2 E}{\partial \mathcal{R}_{pq} \partial \mathcal{R}_{rs}} \quad (3.8)$$

Inserting Eq. (3.7), and using the relationship to the HFB matrix

$$\frac{\partial E}{\partial \mathcal{R}_{pq}} = \mathcal{H}_{pq} \quad (3.9)$$

we have

$$E[\mathcal{R}] \approx E[\mathcal{R}^{(0)}] + \frac{1}{2} \begin{pmatrix} Z^\dagger & Z \end{pmatrix} B \begin{pmatrix} Z \\ Z^\dagger \end{pmatrix} \quad (3.10)$$

where B is the quasi-particle linear response matrix [136],

$$B = \begin{pmatrix} (E_p + E_r)\delta_{pr}\delta_{qs} - \frac{\partial^2 E}{\partial \mathcal{R}_{pq}\partial \mathcal{R}_{rs}} & \frac{\partial^2 E}{\partial \mathcal{R}_{pq}\partial \mathcal{R}_{rs}} \\ \frac{\partial^2 E}{\partial \mathcal{R}_{pq}^*\partial \mathcal{R}_{rs}^*} & (E_p + E_r)\delta_{pr}\delta_{qs} - \frac{\partial^2 E}{\partial \mathcal{R}_{pq}^*\partial \mathcal{R}_{rs}^*} \end{pmatrix} \quad (3.11)$$

The repeated indices in the definition of B do not indicate sums. From the adiabatic time-dependent HFB equations [136], the Z matrices are related to time derivatives of $\mathcal{R}^{(0)}$ through the linear response matrix,

$$\begin{pmatrix} \dot{\mathcal{R}}^{(0)} \\ \dot{\mathcal{R}}^{(0)\dagger} \end{pmatrix} = B \begin{pmatrix} Z \\ Z^\dagger \end{pmatrix} \quad (3.12)$$

Noting that $\mathcal{R}^{(0)}(t) = \mathcal{R}^{(0)}(\bar{q}(t))$ and using chain rule,

$$\frac{\partial \mathcal{R}^{(0)}}{\partial t} = \sum_{i=1}^{N_q} \dot{q}_i \frac{\partial \mathcal{R}^{(0)}}{\partial q_i} \quad (3.13)$$

results in the total energy having the form

$$E[\mathcal{R}] = E[\mathcal{R}^{(0)}] + \frac{1}{2} \dot{q}_i \dot{q}_j \mathcal{M}_{ij} \quad (3.14)$$

where we define the collective inertia matrix as

$$\mathcal{M}_{ij} = \begin{pmatrix} \frac{\partial \mathcal{R}}{\partial q_i} & \frac{\partial \mathcal{R}}{\partial q_i} \end{pmatrix} B^{-1} \begin{pmatrix} \frac{\partial \mathcal{R}}{\partial q_j} \\ \frac{\partial \mathcal{R}}{\partial q_j} \end{pmatrix}. \quad (3.15)$$

Eq. (3.14) has the form of a classical Hamiltonian in terms of collective coordinates $q_i(t)$

and collective momentum $p_i(t)$. If we "requantize" this using Dirac quantization,

$$q_i(t) \rightarrow \hat{q}_i(t), \quad p_i \rightarrow \frac{\partial}{\partial q_i} \quad (3.16)$$

and define the quantity $V(\vec{q}) = E[\mathcal{R}^{(0)}(\vec{q}(t))]$ to be the potential energy surface (PES) at a point $\vec{q}(t)$ we arrive at a collective Hamiltonian operator

$$\hat{H} = \frac{1}{2} \mathcal{M}_{ij}^{-1} \frac{\partial}{\partial q_i} \frac{\partial}{\partial q_j} + V(\vec{q}) \quad (3.17)$$

The collective inertia is computationally expensive to calculate since it requires the linear response matrix B and its inverse. In systems with axial symmetry, the rank of B is on the order of 10^5 . The finite amplitude method (FAM) was introduced as a fast and efficient way to compute the collective inertia [146, 147] and this has been implemented for fission in Ref. [148]. We use the cranking approximation which approximates \mathcal{M} by removing second derivatives of E from the linear response matrix [149]. Then, the collective inertia takes the form [149],

$$\mathcal{M}_{ij}(\vec{q}) = \frac{1}{2\dot{q}_i\dot{q}_j} \sum_{\alpha\beta} \frac{(F_{\alpha\beta}^{i*} F_{\alpha\beta}^j + F_{\alpha\beta}^i F_{\alpha\beta}^{j*})}{E_\alpha + E_\beta} \quad (3.18)$$

where $F_{\alpha\beta}^i$ are

$$\frac{F^i}{\dot{q}_i} = U^\dagger \frac{\partial \kappa^*}{\partial q_i} U^* + U^\dagger \frac{\partial \rho^*}{\partial q_i} V^* - V^\dagger \frac{\partial \rho}{\partial q_i} U^* - U^\dagger \frac{\partial \kappa}{\partial q_i} U^*. \quad (3.19)$$

The derivatives are computed using a three-point Lagrange approximation [128, 150]. Methods evaluating these derivatives by perturbation theory also exist however they have been

found to produce large variations in the fission lifetime compared to the non-perturbative methods [128, 149, 151]. We use the perturbative approach due to its small computational cost as well as non-perturbative formulations of the collective inertia in our studies.

3.2 Tunneling in the Reduced Space

Tunneling physics can be recovered by solving the collective Schrödinger equation,

$$\left(\frac{\epsilon^2}{2}\mathcal{M}_{ij}^{-1}\frac{\partial}{\partial q_i}\frac{\partial}{\partial q_j}+V(\vec{q})\right)\psi(\vec{q})=E_0\psi(\vec{q}) \quad (3.20)$$

where we inserted an expansion parameter ϵ . We solve Eq. (3.20) using leading order WKB theory [152] where we assume an asymptotic solution,

$$\psi(\vec{q})\sim\exp\left(\frac{1}{\epsilon}S_0(\vec{q})\right)\quad\text{as}\quad\epsilon\rightarrow 0 \quad (3.21)$$

Ignoring second order derivatives of S_0 , the resulting differential equation is a multi-dimensional eikonal equation,

$$\mathcal{M}_{ij}^{-1}\frac{\partial S_0}{\partial q_i}\frac{\partial S_0}{\partial q_j}=2(V(\vec{q})-E_0) \quad (3.22)$$

We look for exponentially damped solutions in the tunneling region $V(\vec{q})-E_0>0$. Consider the reparameterization $\vec{q}(s)$ with affine real parameter s satisfying $\vec{q}(0)=\vec{q}_{\text{in}}$, $\vec{q}(1)=\vec{q}_{\text{out}}$. Integrating along the curve, and using the line integral theorem leads to the classical action

$$S[L]=\int_0^1\sqrt{2\mathcal{M}_{\text{eff}}(s)(V(s)-E_0)}ds \quad (3.23)$$

where the effective mass is

$$\mathcal{M}_{\text{eff}}(s) = \mathcal{M}_{ij}(s) \frac{dq_i}{ds} \frac{dq_j}{ds} \quad (3.24)$$

and L represents the trajectory connecting \vec{q}_{in} and \vec{q}_{out} . We define the outer turning surface as $V(\vec{q}) = E_0$. Relevant contributions to the tunneling amplitude $\psi(\vec{q})$ correspond to pathways that minimize S ,

$$S[L] \geq \min \int_0^1 \sqrt{\mathcal{M}_{\text{eff}}(s)(V(s) - E_0)} ds \quad (3.25)$$

Stationary points of the classical action, $L = L_{\text{min}}$, produce the lower bounds of the classical action and are called least action pathways (LAPs). E_0 is taken to be the ground state potential energy $V(\vec{q}_{\text{gs}})$. In other studies, E_0 includes zero-point energy corrections associated with the ground state [91]. The classical action $S[L]$ can feature multiple stationary points depending on the form of \mathcal{M}_{eff} and V . This fact has consequences for fission and will be explored in section 4. LAPs are formally equivalent to instantons in the path integral formulation of quantum mechanics [153–155]. Mean-field instantons are discussed in section 5.

The spontaneous fission half-life is approximated using a semi-classical approximation,

$$t_{1/2} = \frac{\ln(2)}{nP}, \quad P = \frac{1}{1 + e^{2S(L_{\text{min}})}} \quad (3.26)$$

where P is the probability of tunneling through the potential barrier $V(\vec{q})$ [156, 157]. n is a phenomenological parameter representing the number of classical assaults on the barrier estimated by the zero-point energy of the ground state [156]. We use $n = 10^{-20.38} \text{ s}^{-1}$ from

Ref. [158].

To determine a fission trajectory, we calculate a PES $V(\vec{q})$ and the collective inertia $\mathcal{M}(\vec{q})$ using the constrained DFT approach outlined in section 2.3. Practically, this is done by computing the PES and collective inertia on a grid by constraining to various expectation values of deformation parameters \vec{q} . Since we do not apriori know where the fission trajectory is located in the collective space, we compute the PES and inertias on a sufficiently large domain of collective coordinates. In the next section, we discuss the numerical method used to find LAPs. The sections to follow largely draw from my own publication [159].

3.3 The Nudged Elastic Band Method

Previous studies of fission lifetimes used grid-based methods such as the dynamic programming method (DPM) [157] or the Ritz method [158] to minimize the action in Eq. 3.25. Because these algorithms are grid-based, accuracy of the calculated collective action and pathway were limited by the resolution of the grid. Further, the algorithm complexity scales exponentially as the number of grid points increase. The nudged elastic band (NEB) is an iterative method that does not suffer from these limitations. Originally developed for transition state theory in chemistry [160–165], we adapted the NEB method for applications to fission in Ref. [159]. We published an open-source software package implemented in Python named PyNEB (available at <https://pyneb.dev/>) as part of Ref. [159].

The NEB method discretizes the trajectory L into N points, called images, located at \vec{q}_i . $S[L]$ is subsequently discretized using the trapezoidal rule. Each image is regarded as a unit point mass obeying classical equations of motion in the presence of a net force \vec{F}_i^{opt}

$$\ddot{\vec{q}}_i = \vec{F}_i^{\text{opt}} \tag{3.27}$$

The net force on all images contain two terms,

$$\vec{F}_i^{\text{opt}} = \vec{F}_i^{(k)} + \vec{g}_i^\perp \quad (3.28)$$

$\vec{F}_i^{(k)}$ is a spring force coupling each image together,

$$\vec{F}_i^{(k)} = k \left(|\vec{q}_{i+1} - \vec{q}_i| - |\vec{q}_i - \vec{q}_{i-1}| \right) \vec{\tau}_i \quad (3.29)$$

where $\vec{\tau}_i$ is the tangent unit vector at point \vec{q}_i defined in Ref. [165]. The spring constant k is a tunable parameter that controls the strength of the spring force. We take the spring constant to be the same for all \vec{q}_i . The force \vec{g}_i^\perp is the optimization force chosen depending on the problem. $\vec{g}_i = \vec{\nabla}_i V$ can be chosen to find minimum energy pathways (MEPs) or $\vec{g}_i = \vec{\nabla}_i S_0(\vec{q})$ for LAPs. The components parallel to the curve are projected out using the Gram-Schmidt procedure to decouple the dynamics of the path from the tangent forces of the spring [166],

$$\vec{g}_i^\perp = \vec{g}_i - (\vec{g}_i \cdot \vec{\tau}_i) \vec{\tau}_i. \quad (3.30)$$

The forces on the boundary points of the discretized path \vec{q}_1 and \vec{q}_N are defined differently. First, the spring force is one-sided,

$$\vec{F}_1 = k|\vec{q}_2 - \vec{q}_1|, \quad \vec{F}_N = k|\vec{q}_N - \vec{q}_{N-1}| \quad (3.31)$$

Second, the end points \vec{q}_1 and \vec{q}_N need not be fixed to a single point. It is often desirable to constrain the end points to a particular equipotential surface $V(\vec{q}) = \text{constant}$. This is done

by adding a harmonic constraint. The total force on \vec{q}_N is,

$$\vec{F}_N^{\text{opt}} = \vec{F}_N^{(k)} - \left(\vec{F}_N^{(k)} \cdot \vec{f}_N(\vec{q}_N) - \eta[V(\vec{q}) - E] \right) \vec{f}(\vec{q}_N) \quad (3.32)$$

where $\vec{f}(\vec{q}_N) = -\nabla V/|\nabla V|$ and η is a parameter that determines the strength of the constraining force. A similar expression is enforced on \vec{q}_1 . In our applications, this constraint is useful for finding pathways to outer turning surfaces and optimal exit points.

Algorithm 1 Nudged Elastic Band

```

Define initial start and end point
Initialize images along some initial trajectory
for Steps do
  for Images do
    Update effective force
    Compute velocity of image
    Compute forces
    Translate image
  end for
  Compute collective action
  Check convergence
end for

```

To update the forces, various optimization routines have been used. Originally, a velocity Verlet algorithm [167, 168] was used to find MEPs for chemical reaction rates in transition state theory [160–165]. While this algorithm is numerically stable for our applications, it requires many iterations to find an LAP. The Fast Inertia Relaxation Engine (FIRE) was developed to improve the overall convergence speed of the Verlet algorithm [169, 170]. The FIRE algorithm features an adaptive acceleration step to reduce the number of iterations. We found it to be numerically stable and robust in the variation of the algorithm’s parameters for our application to fission. We implemented both the original velocity Verlet and FIRE algorithms in PyNEB and found that FIRE improved the convergence of the nudged elastic

band. The basic algorithm for PyNEB is shown in Algorithm 1.

3.4 Analytic Examples

PyNEB’s performance was bench-marked against grid-based methods DPM and Dijkstra’s algorithm (DA) [171] as well as numerical solutions to the Euler-Lagrange (EL) equations for the collective action. Using the Müller-Brown (MB) [172, 173] and symmetric/asymmetric six-camel back (CB) analytic surfaces [159, 174], the performance of the NEB method was assessed by comparing the LAP found using NEB (denoted as NEB-LAP) to the paths found using the DPM, DA, and EL approaches. We assume a constant inertia $\mathcal{M}_{ij} = \delta_{ij}$ for these cases. The details regarding the initialization, optimization, and PESs used are found in Ref. [159]. The calculated LAP action values for each method as well as the MEP calculated with NEB (denoted as NEB-MEP) are reproduced in Table 3.1. The LAPs computed with NEB,

Table 3.1: Action integrals for the 6-Camel-Back (CB-S and CB-A) and Müller-Brown (MB) surfaces. The integrals have been calculated using a linear spline interpolation evaluated at 500 points along each trajectory. Table taken from Ref. [159].

	NEB-MEP	NEB-LAP	DPM	EL	DA
CB-S	5.522	5.518	5.524	5.536	5.563
CB-A	6.793	6.404	6.405	6.407	6.886
MB	28.491	22.875	22.909	22.871	23.427

EL, DPM, and DA methods are very similar for all three surfaces. The DA trajectory tends to deviate from the others. DA is more constrained by the grid spacing as it can only consider its nearest neighbors. This is reflected in the actions displayed in Table 3.1. DPM does not have this constraint. For all cases, the NEB method consistently determines LAPs with slightly lower action values when compared to other methods. This shows that the NEB algorithm can accurately determine an LAP and is an improvement over established algorithms. It is important to note that the MEP action values are higher than the LAP actions on the CB-A and MB surfaces. This shows MEPs are not equivalent to the LAP in

general. Appendix A shows the conditions necessary for an LAP and MEP to be equivalent however MEPs should not be used to calculate tunneling trajectories in general.

3.5 Realistic Examples

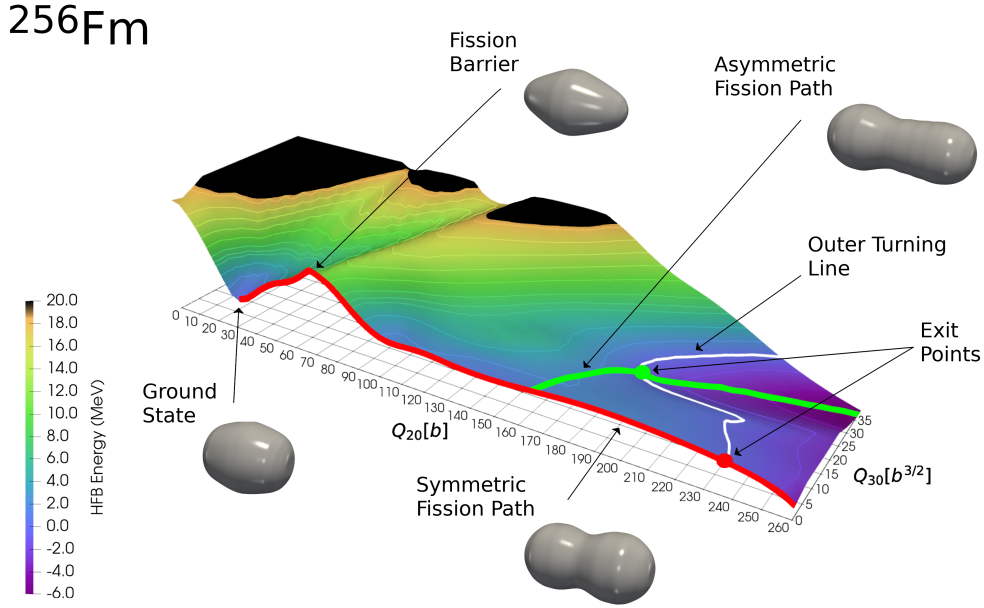


Figure 3.2: Calculated PES for ^{256}Fm parameterized by Q_{20} and Q_{30} using D1S EDF. Details are discussed in Ref. [159]. Figure taken from Ref. [159]

In most realistic calculations, we choose Q_{20} and Q_{30} as collective coordinates. As a visual example, Figure 3.2 shows a two-dimensional PES for ^{256}Fm calculated using the D1S EDF. The energy of the PES is shifted by the ground state energy; $V - E_{\text{gs}}$. Symmetric (red) and asymmetric (green) fission trajectories begin at the ground state at $E_0 = 0$ and progress through the barrier to the outer turning line shown in white. The red and green dots indicate the exit points where the pathways exit the barrier. Particle density profiles are shown along the symmetric and asymmetric trajectories. Notice that the profiles do not indicate well separated nascent fragments. Scission occurs outside the barrier at much larger deformations [91, 175].

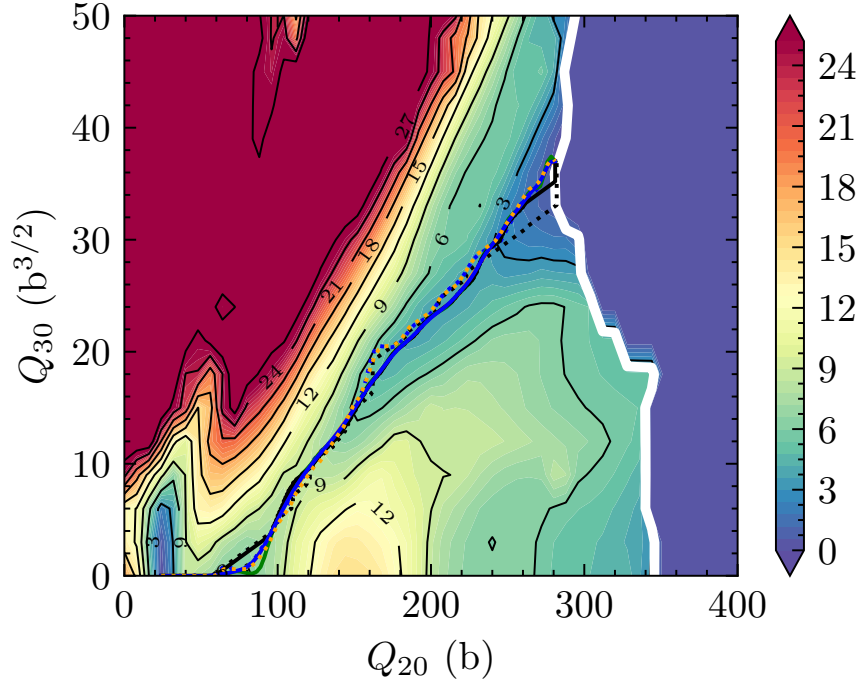


Figure 3.3: Calculated ^{232}U PES (in MeV) using the SkM* EDF. The solid lines correspond to pathways obtained using constant inertia while the dotted lines are those obtained with non-perturbative inertia. The blue, orange, purple, and black curves represent the LAPs calculated using the NEB, DPM, EL, and DA methods, respectively. The green curve is the MEP calculated using NEB and the outer turning line is shown in white. Figure taken from Ref. [159].

To assess the performance of the NEB method and other approaches to the LAP in realistic cases, we carried out nuclear DFT calculations for ^{232}U in two collective coordinates (Q_{20}, Q_{30}) and ^{240}Pu in three collective coordinates $(Q_{20}, Q_{30}, \lambda_2)$ using the Skyrme functional SkM* with the mixed density-dependent pairing EDF from Eq. (2.38). Here, $\lambda_2 = \lambda_{2n} + \lambda_{2p}$. DFT calculation details are discussed in Ref. [159].

To apply the NEB method, which involves derivatives at arbitrary values of collective coordinates, we interpolate the PES and the inertia tensor on the mesh. Because the grid is two dimensional and the PES is smooth, a cubic spline interpolator is sufficient. Technical details about the application of the NEB method on these two surfaces are in Ref. [159].

Fig. 3.3 shows the LAPs calculated with DPM, DA, the EL method, and the NEB with

constant and non-perturbative inertia. By visual inspection, all methods are finding similar pathways and exit points when the inertia tensor is constant. However, we notice small deviations in the trajectories when the non-perturbative inertia is used. The action values are shown in Table 3.2. The NEB consistently finds the path of least action compared to

Table 3.2: Action integrals for ^{232}U computed using DPM, DA, EL method, and the NEB. The paths are computed using constant and non-perturbative inertia tensor are labeled as “con.” and “n.-p.”, respectively. The actions were computed using a linear spline interpolation evaluated at 500 points along each trajectory. Table taken from [159]

		NEB-MEP	NEB-LAP	DPM	EL	DA
^{232}U	con.	174.5	174.2	174.2	174.9	175.8
	n.-p.	-	173.6	173.3	175.0	178.5
^{240}Pu	con.	19.09	18.98	19.21	19.01	22.85
	n.-p.	-	16.54	16.47	18.18	30.50

other methods demonstrating the robustness of the NEB method in a realistic case. Note that the MEP is in rough agreement with the LAP. This is expected as the MEP approximately satisfies the conditions needed to be equivalent to an LAP (see Appendix A for details).

Next, we studied the PES of ^{240}Pu parametrized by $(Q_{20}, Q_{30}, \lambda_2)$. Fig. 3.4 shows trajectories computed using DPM, EL method, and the NEB starting from the fission isomer. Pathways connecting the ground state of ^{240}Pu and its isomer were studied in Ref. [127]. With the addition of the dynamical pairing parameter λ_2 we see the constant inertia pathways are in qualitative agreement and their action integrals are similar with the exception of DA. However, when the inertia is not constant we see the pathways deviate appreciably. Despite this, the DPM and NEB trajectories have nearly the same action. This is because the PES is nearly flat in the λ_2 direction. Deviations in λ_2 direction produce small variations in the action.

If a PES is mostly flat, we noticed that the NEB required at least $\sim 10^5$ iterations to converge. This is because the gradients used to nudge the images in the direction of minimal

action are very small. In this case, DPM produces a slightly lower action than the NEB. The NEB converges to an even lower action if it is initialized with the DPM pathway. This suggests that for tunneling in more than two dimensions using DPM to initialize the NEB might reduce the number of iterations needed for convergence.

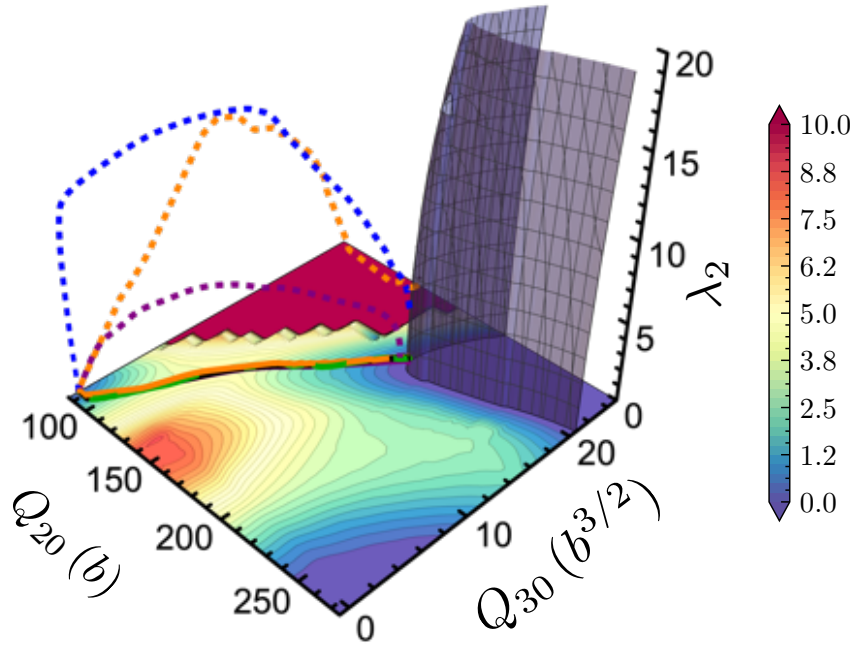


Figure 3.4: The PES (in MeV) for ^{240}Pu in the collective coordinates Q_{20} , Q_{30} and λ_2 . The 2D cross section of the PES of ^{240}Pu at $\lambda_2 = 0$ is shown. The blue, orange, and purple curves are the LAP, calculated using the NEB, DPM, and EL methods, respectively. The dashed curves are pathways computed with non-perturbative inertia. The outer turning surface is indicated by the dark blue meshed surface. Figure taken from Ref. [159].

Exit points disagree quite considerably in the λ_2 coordinate. However, the Q_{20} and Q_{30} coordinates of the exit points are very similar for all trajectories. In the calculation of fission fragment yields (see section 4) the multipole moments of the exit point are the only coordinates needed.

3.6 Summary

In this chapter, I reviewed how the adiabatic approach to spontaneous fission is derived by first highlighting the complications using the DFM action to describe a decay process with quantum tunneling. Then, I describe how we facilitate tunneling through the introduction of real, time-dependent collective coordinates $\vec{q}(t)$. I then reviewed the essential assumptions leading to re-quantization of the collective Hamiltonian and subsequent solution of the collective Schrödinger equation using WKB theory. I then discussed benchmarking the NEB leading to practical applications finding fission trajectories of ^{232}U and ^{240}Pu in two and three collective coordinates respectively. My explicit contributions in the development of PyNEB were implementations of numerical gradients to be used in the optimization routines, implementing the velocity Verlet and FIRE optimization routines, and implementation of the routine to find MEPs. I also contributed to the benchmarking of the NEB implementation by calculating MEPs and LAPs on analytic surfaces and calculated some of the LAPs for ^{232}U and ^{240}Pu . I also mathematically proved differences between MEPs and LAP and showed when they are equivalent (see Appendix A). After this initial study, we have applied the NEB method to more nuclei in two and three dimensions. This is explored in the next section.

Chapter 4. Modes of Spontaneous Fission

In the previous section, we presented the nudged elastic band as a general method for finding least action fission trajectories. The classical action Eq. (3.25) can feature multiple stationary pathways corresponding to different modes of fission. Fig. 3.2 shows one example of multimodal fission featuring symmetric and asymmetric modes. Each mode contributes to the overall tunneling amplitude through the fission barrier however, the pathways are not physical observables. In fact, each trajectory contributes to the experimentally measurable total mass and charge fission yield. This chapter presents a multimodal fission study carried out in my publication Ref. [176]. First, I discuss how we model the fission fragment mass and charge distributions. Then, I discuss the application of PyNEB and our fission fragment distribution approach to model the spontaneous fission of a Fermium isotope chain and superheavy nuclei.

4.1 Fission Fragment Distributions

Fission fragments emerge at a time near scission where the nucleus separates into fragments [91]. Leading up to scission, shell effects, dissipation, odd-even effects, decoherence, and phase space effects interplay to determine properties, such as charge and mass, of the nascent fragments [33, 91]. At the current time, there is no complete theory capable of predicting all fission fragment properties exactly however, there exist many different models that can be used to predict the mass and charge yield distributions. We briefly overview the models used in Ref. [176] to motivate the method we use to estimate mass and charge yields.

4.1.1 Time-dependent Approach

Starting with the DFM action from Eq. (3.1), TDHFB equations can be derived. If the evolution is initialized with configurations on the outer turning surface, the dynamics are

classically allowed. The mean-field is time evolved until separation and observables such as the total kinetic energy, fragment yields, and excitations energies can be calculated [177, 178]. This approach is appealing since the TDHFB evolution is equivalent to exact one-body density dynamics guaranteed by the Runge-Gross and Van Leeuwen theorems (see section 3.1). Non-adiabaticity and one-body dissipation in fission can be modeled in this framework [177, 179]. However since the evolution is considered classical, quantum fluctuations are lacking. TDHF (and by extension TDHFB) has been proven to underestimate the particle number fluctuations needed to calculate fragment distributions [55, 180, 181]. Because of this, TDHFB has difficulty predicting realistic fission yields. Time-dependent multi-reference techniques, which model the many-body state as a linear combination of particle-hole or quasi-particle Slater determinants, have recently been applied to calculate fission yields [182–184]. While this approach is promising, multi-reference approaches tend to be too computationally expensive for large scale studies of fission.

4.1.2 Stochastic Methods

To account for the lack of quantum fluctuations, stochastic mean field methods have been developed [181, 185]. These approaches essentially replace single a TDHF (or TDHFB) trajectory with a superposition of classical trajectories initialized with conditions that are sampled from a statistical distribution of initial values in a way that reproduces the fluctuations in the of observables of interest. Then, each initial condition is time evolved according to a classical equation of motion to reproduce quantum mean values and fluctuations dynamically. This method has been applied to calculate the fission yields of ^{258}Fm [186]. While progress with this approach has been made, the computational cost is also too high to use for large scale studies.

Starting from the stochastic mean-field approach, Ayik showed in Ref. [185] one can

reduce the mean-field equations of motion to a classical Langevin equation for a point particle in one dimension. One can extend this result to multiple dimensions via:

$$\frac{d}{dt} \left(\mathcal{M}_{ij}(\vec{q}) \dot{q}_j \right) + \frac{\partial V(\vec{q})}{\partial q_i} = -\gamma_{ij} \frac{dq_j}{dt} + \eta_{ij} \xi_j(t). \quad (4.1)$$

\mathcal{M} is the collective inertia defined in Eq. (3.15), V is the PES, γ_{ij} is the friction matrix, $\xi_j(t)$ is a time dependent random variable representing a stochastic force, and η_{ij} is the stochastic strength matrix. The Langevin equation has been widely used to model nuclear dynamics in dissipative systems (see Refs. [187, 188] for reviews). Kramers [189] showed that dissipative tunneling through collective barrier can be modeled as a diffusion process with a stochastic equation similar to Eq. (4.1). Diffusion is compatible with the adiabatic assumption made in section 3.1 as the intrinsic degrees of freedom are assumed to be decoupled from the collective motion. From this point of view, the system described by the space of collective states represents an open system while the intrinsic system represents an environment. Coupling these two systems together results in the collective system and the environment being able to exchange information and hence reproduce dissipative effects.

The friction matrix and stochastic strength matrix are related to the temperature of the nucleus as function of excitation energy and level density by the fluctuation-dissipation theorem [190]. The exact density of states is unknown and has been studied through analytical, configuration interaction, and statistical models [8, 33]. Modeling the strength and friction matrix has been explored in stochastic mean field theory [181, 185]. Rather than modeling the level density or the friction and strength matrices directly, phenomenological models have been used to predict fission yields, namely, Brownian shape motion (BSM) [191–194], scission point models (SPM) [195–197], and the semi-empirical general description of fission

observables (GEF) [198]. The BSM model phenomenologically treats stochastic motion in the collective space as the nucleus approaches scission while SPM only considers properties of the nucleus at scission. GEF is based on geometric and statistical properties of the nucleus as it deforms. All these models produce qualitative differences for many fissioning nuclei, such as the number of mass and charge yield peaks and their locations [197].

4.1.3 Hybrid Method

A hybrid approach that combines DFT input and statistical phenomenology to estimate the fission fragment yields was developed in Refs. [199, 200]. We use this model to calculate fission yields in this work and we review the essential ideas of this approach here.

When considering the exit point configurations, DFT allows one to produce an effective one-body picture of the distribution of protons and neutrons in a fissioning nucleus. To estimate the spatial distribution of nucleons, we use the nucleon localization function (NLF) [201, 202],

$$C_{\tau s} = \left[1 + \left(\frac{\tau_{\tau s} \rho_{\tau s} - \frac{1}{4} |\vec{\nabla} \rho_{\tau s}|^2 - |\vec{j}_{\tau s}|^2}{\rho_{\tau s} \tau_{\tau s}^{\text{TF}}} \right) \right]^{-1}, \quad \tau_{\tau s}^{\text{TF}} = \frac{3}{5} (6\pi^2)^{2/3} \rho_{\tau s}^{5/3} \quad (4.2)$$

where the subscripts τ and s label the isospin and spin projections respectively. τ^{TF} is the Thomas-Fermi kinetic energy density introduced as a reference density. The NLF represents the conditional probability of finding a particle at a spatial location \vec{r}_2 given a particle of the same species is located at \vec{r}_1 . An example NLF for protons and neutrons for ^{254}Fm at an asymmetric exit point configuration is shown in Fig. 4.1. Notice for both protons and neutrons, there are spatially well defined prefragments connected through a non-vanishing neck region. The method of identifying the prefragments is not a well defined procedure. First, we associate a center coordinate with each prefragment by choosing a local extremum

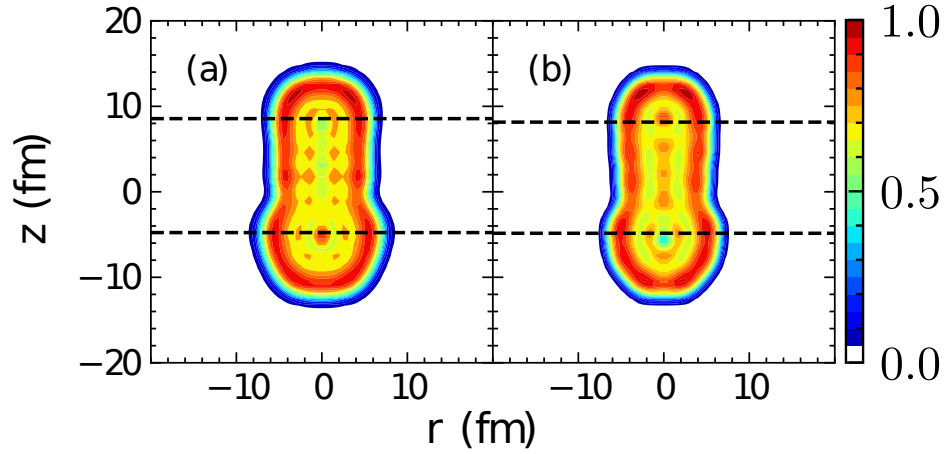


Figure 4.1: The nucleon localization functions calculated at an asymmetric exit point configuration of ^{254}Fm using the SkM* EDF. (a) and (b) are neutron and proton localizations respectively. Horizontal dashed lines denote the selected center of the prefragments.

around the center of each prefragment along the $r = 0$ axis by visual inspection [199]. In symmetric fission, the prefragments have no octopole deformation and this choice is made to preserve reflection symmetry. However, in general the prefragments can break reflection symmetry by asymmetric deformation and the center is no longer located at an extremum of the NLF. This results in a miscount when partitioning the number of nucleons into the neck and prefragment regions. For asymmetric configurations, we instead assume spherical prefragments and look for the maximal extent of the localization for each prefragment. The z -coordinate of this extent is taken to be the center rather than an extremum along the $r = 0$ axis.

The number of nucleons assigned to each prefragment is determined by integrating the proton and neutron particle densities upwards and downwards in the z -coordinate for the top and bottom prefragments respectively. Each integration is then multiplied by 2 assuming each prefragment is approximately spherical. The remaining nucleons are assumed to be in

the neck region of the fissioning nucleus. The neck nucleons are then distributed between the prefragments according to a microcanonical probability distribution proposed by Fong in Ref. [203],

$$P(A_1, A_2, E) \propto \frac{1}{2} \left(\frac{A_1^{5/3} A_2^{5/3}}{A_1^{5/3} + A_2^{5/3}} \right)^{3/2} \left(\frac{A_1 A_2}{A_1 + A_2} \right)^{3/2} \frac{(a_1 a_2)^2}{(a_1 + a_2)^{5/2}} \quad (4.3)$$

$$\times \left(1 - \frac{1}{2[(a_1 + a_2)E]^{1/2}} \right) E^{9/4} \exp \left(2\sqrt{(a_1 + a_2)E} \right).$$

A_1 and A_2 are the mass number of the fragments, E is the excitation energy of the nucleus, and $a_i = A_i/10 \text{ MeV}^{-1}$ are level density parameters [204]. E is estimated using a liquid drop model and classical Coulomb interaction [204]. Since A_i are discrete, the mass and charge yields are convolved with Gaussians and, for the charge yield, the odd and even Z yields are convolved separately to show the odd-even staggering effect [200]. The partitioning is not guaranteed to result in an integer number of particles in the neck or prefragment regions and we choose to round the integrated particle numbers to the nearest integer. This introduces a 2-particle uncertainty $N_i \pm 1$ and $Z_i \pm 1$ in the calculated fission fragment yields. This uncertainty is larger than the input used to calculate E and, within the particle uncertainty, experimental measurements of the yields agree well [199].

Each fission pathway is associated with a relative probability defined as,

$$P_i \approx \frac{e^{2S_i}}{\sum_k e^{2S_k}} \quad (4.4)$$

where S_i is the action of the i -th pathway. We assume the pathways are independent. The total fission yield is the sum over all fission yields calculated at every exit point weighted by

their respective relative probability,

$$Y_{\text{tot}} = \sum_{i=1}^n P_i Y_i \quad (4.5)$$

where Y_i is the yield calculated from i -th exit point and n is the total number of exit points.

4.2 Applications

4.2.1 The Fermium Isotope Chain

The even-even Fm isotopes with neutron numbers N , $154 \leq N \leq 160$ are known to undergo a transition from asymmetric fission, characteristic of lighter actinides, to symmetric fission as N increases towards $N = 164$. This transition is related to strong shell effects present in the prefragments as they approach the doubly magic nucleus ^{132}Sn . This transition in fission mode dominance has been investigated in numerous publications [178, 182, 199, 200, 205–219]. This motivates choosing the Fermium isotopic chain to study multimodal fission with PyNEB.

We calculated PESs for $^{254-260}\text{Fm}$ parameterized by coordinates (Q_{20}, Q_{30}) with the SkM*, UNEDF1_{HFB}, and D1S energy functionals. The PESs are shown in Fig. 4.2. Since triaxiality is ignored, one path along $Q_{30} \approx 0$ connects the ground state and the fission isomer in most cases. The path continues past the isomer, and then a bifurcation resulting in a coexistence of symmetric and asymmetric pathways takes place. Paths are smooth at the bifurcation point. We observe an additional asymmetric pathway present in the PES computed with SkM* that is not present in the other cases.

The relative probability P_s of the symmetric mode is shown in Table 4.1. All EDFs transition from an asymmetric-dominant to a symmetric-dominant fission path with increas-

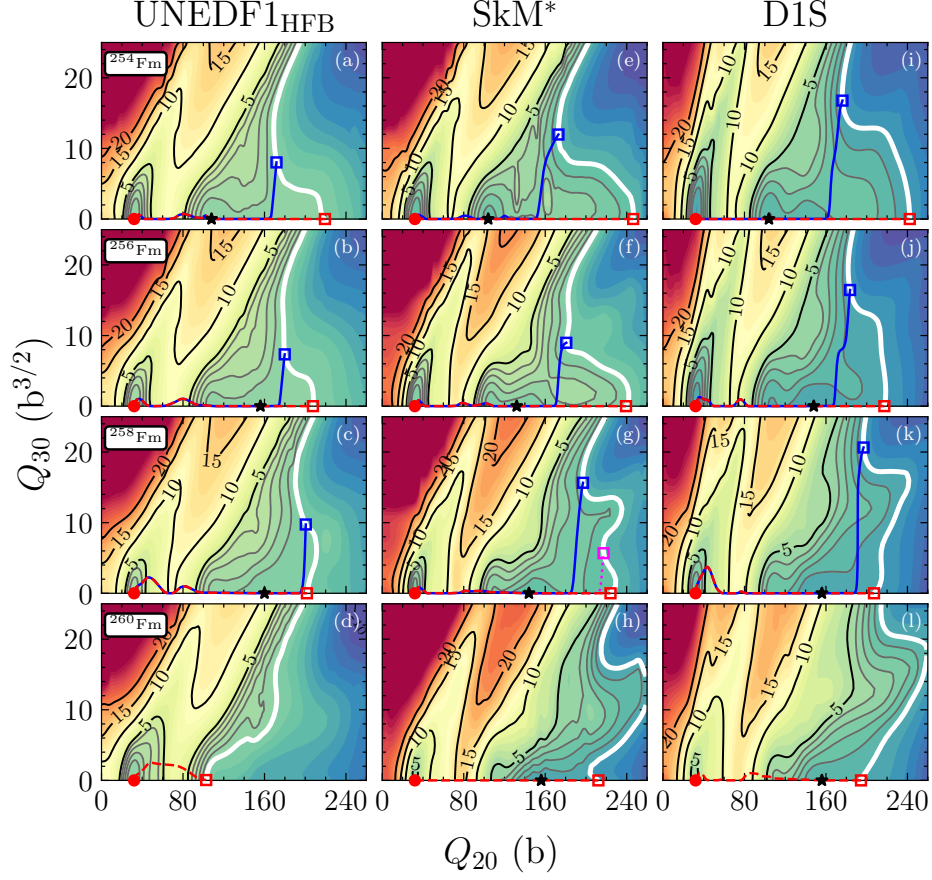


Figure 4.2: Potential energy surfaces of $^{254-260}\text{Fm}$ (in MeV) calculated using UNEDF1_{HFB} (left column), SkM* (center column), and D1S (right column) EDFs. The symmetric (dashed lines) and asymmetric (solid and dotted lines) least action paths are drawn from the ground state (solid circle) to the fission isomer (asterisk) to the exit point (open square). The white contour denotes the outer turning line. Gray contours are marked at 1-MeV intervals for $0 < V_{\text{eff}} < 5$ MeV. Figure taken from Ref. [176]

ing N . Competition between the modes is present in $^{256,258}\text{Fm}$ for UNEDF1_{HFB}, ^{258}Fm for SkM, and ^{256}Fm for D1S. The calculated yields are shown in Fig. 4.3 together with experimental data from Refs. [220–223]. The experimental data for $^{254,256}\text{Fm}$ show an asymmetric distribution, while distributions for ^{258}Fm are symmetric. The error bands in the calculated distributions are from the 2-particle uncertainty discussed in section 4.1.3. The UNEDF1_{HFB} results are in close agreement with the data for ^{254}Fm . Competition between modes for $^{256,258}\text{Fm}$ is present across all EDFs. However, the D1S model overestimates

Table 4.1: The relative probability P_s of the symmetric mode for the 2D calculation of Fm isotopes.

	^{254}Fm	^{256}Fm	^{258}Fm	^{260}Fm
UNEDF1 _{HFB}	≈ 0	0.12	0.79	1
SkM*	≈ 0	≈ 0	0.17	1
D1S	≈ 0	0.88	1	1

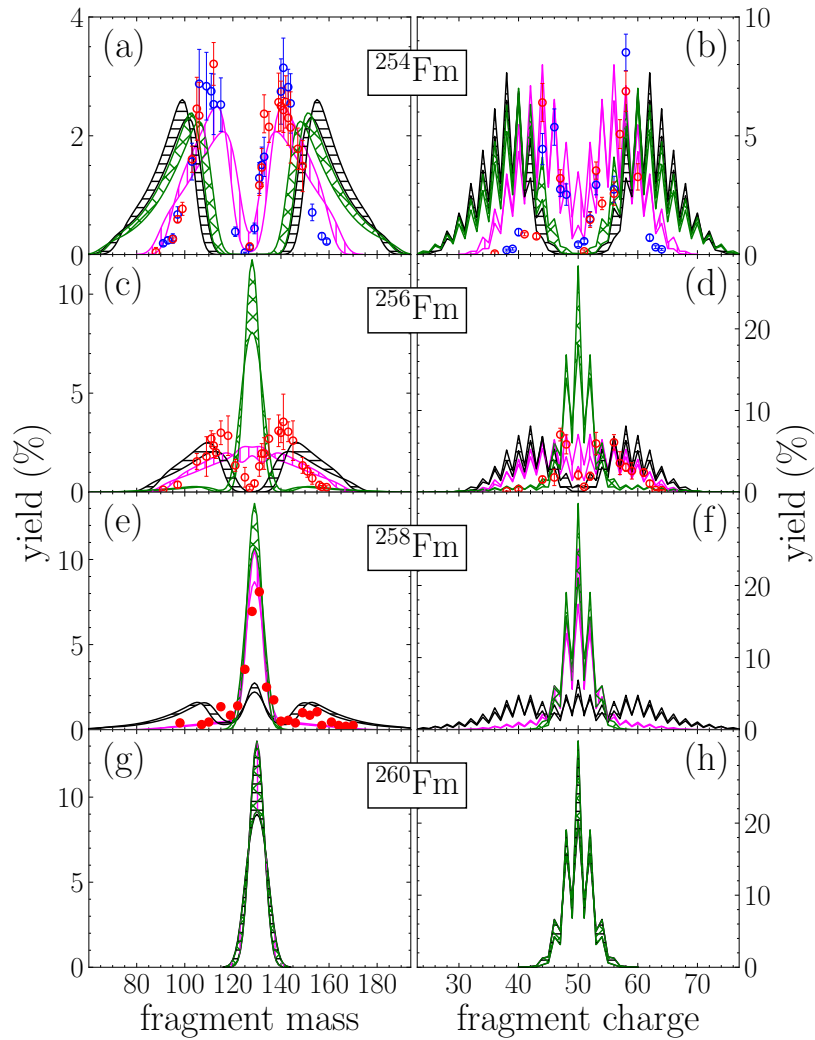


Figure 4.3: Fission fragment mass (left) and charge (right) yields for $^{254,256,258,260}\text{Fm}$ calculated with UNEDF1_{HFB} (magenta vertical patterns), SkM* (black horizontal patterns), and D1S (green \times patterns). Experimental yields (circles) [220–223] are shown where available. Figure taken from Ref. [176].

the symmetric contribution. All EDFs predict overlapping symmetric yields for ^{260}Fm . The transition from asymmetric to symmetric fission is clearly present, albeit at different neutron numbers for the EDFs. Despite the overestimation of the symmetric mode for ^{256}Fm , we conclude that UNEDF1_{HFB} provides the best description compared to the other EDFs.

We then extended the 2D surfaces into a 3D collective space parameterized by (Q_{20}, Q_{30}, Q_{40}) for $^{254,256,258}\text{Fm}$. We present the results for SkM* PES for ^{258}Fm . Discussion of UNEDF1_{HFB} and D1S results are in Ref. [176]. Fig. 4.4 shows the 3D PES for ^{258}Fm computed with SkM* and least action pathways. The part of the path from the ground state to the fission

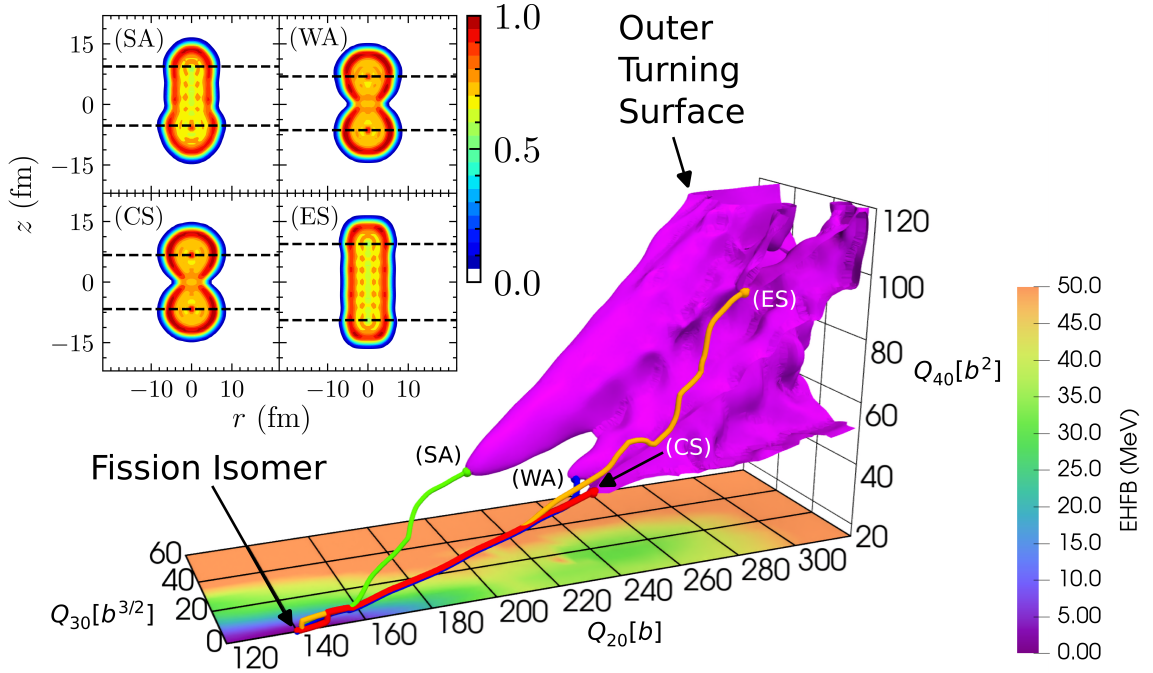


Figure 4.4: The least action paths in 3D for ^{258}Fm using SkM*. The outer turning surface is shown. A 2D PES is shown for constant $Q_{40} = 16 \text{ b}^2$. Neutron localizations for the identified precession configurations are shown in the insets. Figure adapted from Ref. [176].

isomer is not shown for clarity. Two symmetric modes are identified: the compact (CS) and elongated (ES) modes. Let \mathcal{C} denote the precession configuration at an exit point. \mathcal{C}_{ES} has larger Q_{40} than \mathcal{C}_{CS} , and hence the neck region for \mathcal{C}_{ES} is thicker. We also found two

asymmetric fission pathways: the weak (WA) and strong (SA) modes. \mathcal{C}_{WA} is characterized by a small ($Q_{30} < 10 \text{ b}^{3/2}$) octupole moment that were present in the 2D case. The ES mode is present due to the Q_{40} constraint, however, the probability associated with this pathway is negligibly small. The other modes are consistent with the 2D calculations. Fig. 4.5 shows

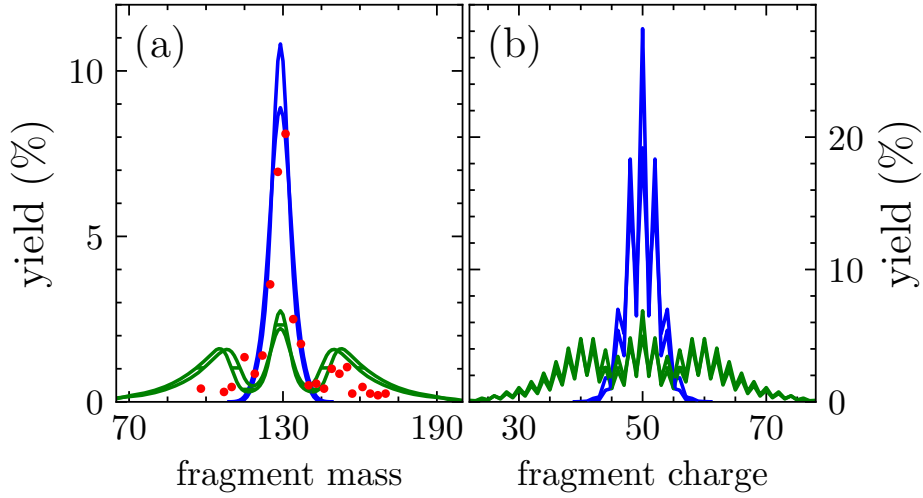


Figure 4.5: The fragment mass (left) and charge (right) yields for ^{258}Fm using SkM* calculated in the 2D (green solid lines) and 3D (blue lines) collective spaces. Experimental data from [223] is shown as red filled circles. Figure adapted from Ref. [176].

the corresponding SkM* fragment yields compared to the yields calculated in the 2D collective space. Due to the additional coordinate, agreement with experiment is improved due to the increase in the relative contribution of the symmetric mode. However, the tails of the distribution are suppressed and worsen the agreement with experiment. This suggests that additional collective coordinates should be considered when multiple fission modes are present. Their addition may induce or reduce competition between the modes.

4.2.2 Superheavy Nuclei

The superheavy nuclei are stabilized by quantum shell effects [9, 224, 225] making them short-lived. The dominant decay modes observed in superheavies are α decay and spontaneous fission [225–230]. Neutron-rich superheavy nuclei may decay directly via spontaneous fission

[27, 29, 194, 197, 198, 231, 232] marking the end of the r -process nucleosynthesis trajectory.

Multimodal fission has been studied in the superheavy region in Refs. [209, 231].

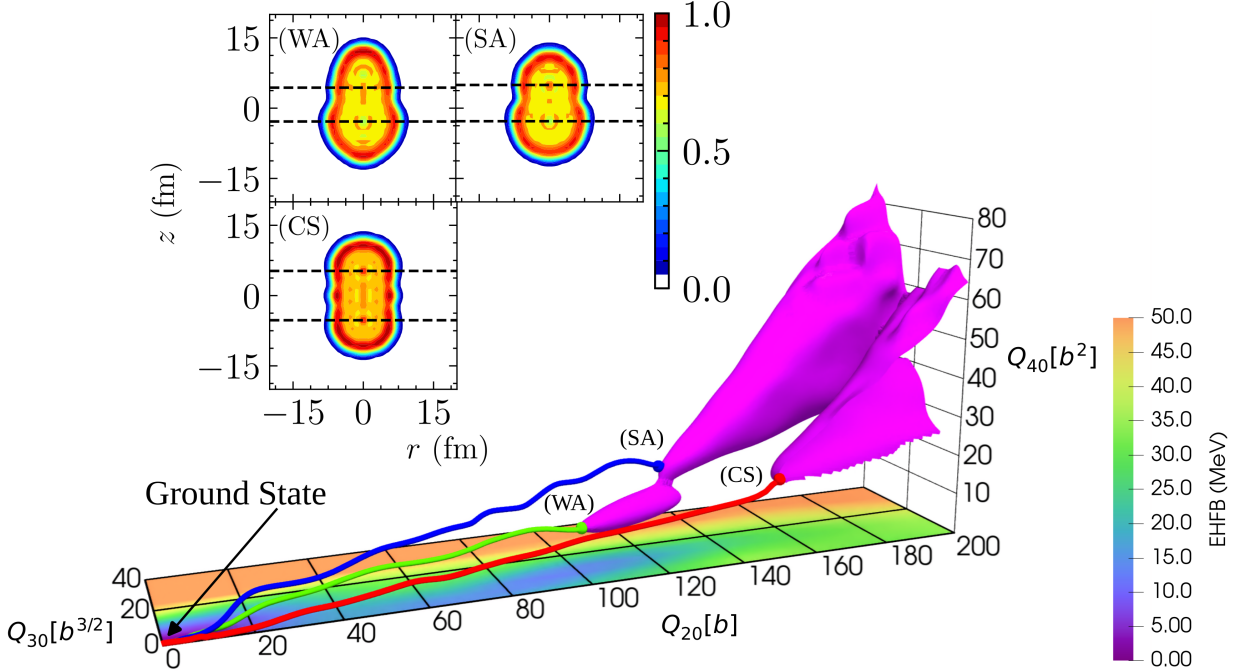


Figure 4.6: Similar as Fig. 4.4 but for $^{306}_{122}$. The 2D surface is at constant $Q_{40} = 0$. Figure adapted from Ref. [176].

In our study, LAP calculations were carried out in 2D for ^{258}Rf , ^{262}Sg , and ^{262}Hs using the UNEDF1_{HFB} and SkM* functionals. The calculated fragment yield peaks for each mode agrees between EDFs, but contributes differently due to their relative probabilities [176]. In comparison, SPM [197] and GEF [198] predict asymmetric yields for ^{258}Rf . BSM predicts asymmetric yields for ^{258}Rf and ^{262}Sg and symmetric yields for ^{262}Hs [194]. The large spread between theoretical predictions highlights the usefulness of multimodal fission for differentiating between models.

Finally, we consider $^{306}_{122}$, an undiscovered superheavy nucleus that is proposed to exhibit multimodal fission [194, 197, 231, 233–236]. Fig. 4.6 shows the PES and pathways

for $^{306}_{122}$ calculated with SkM*. A pronounced asymmetric valley forms beyond the outer turning surface leading to the cluster-decay channel, similar to ^{294}Og [237]. The fission yields show qualitative agreement between SkM* and UNEDF1_{HFB} EDFs [176]. As with ^{294}Og , the heavy fragment is close to the doubly magic nucleus ^{208}Pb . The calculated yields disagree with the symmetric yields predicted with the BSM model [194] however, SkM* results are consistent with those in Refs. [231, 233].

4.3 The Need for Reduced Order Modeling

Large scale calculations of fission properties are essential to study r -process as hundreds of fissioning nuclei are hypothesized to play a role (see section 1). Additionally, estimating uncertainties for fission lifetimes and yields within a Bayesian framework requires massive computational resources. Given the computational costs, using DFT with quantified uncertainties for fission is infeasible and the development of DFT emulators is necessary. Recently, feed-forward neural networks were used to emulate the PES and collective inertia tensor, parametrized by Q_{20} and Q_{30} [238]. The result was successful emulation of fission lifetimes for many r -process nuclei. Reduced order modeling and other dimensionality reduction techniques have recently been applied to problems in nuclear physics [239–243]. Ref. [244] has recently explored applications of reduced order modeling techniques to emulate DFT calculations needed for large scale studies of fission.

4.4 Summary

In this chapter, I applied PyNEB in systems with coexisting modes of fission. My explicit contributions to this work were computation of the PESs using the SkM* EDF and computation of LAPs and yields for this case. Individual modes are successfully classified with the nudged elastic band technique according to their relative probabilities. Using the fission yield

estimation schemes from Refs. [199, 200], we also computed the total fission fragment mass and charge yields for a Fermium isotope chain and various superheavy nuclei. A well defined transition from symmetric to asymmetric fission was observed in the Fermium chain however, the point of transition strongly depends on the EDF and the collective space. Overall, the UNEDF1_{HFB} functional produced results that best agreed with experiment. Our predicted fission yields tend to disagree with BSM and SPM approaches. The spontaneous of superheavy nuclei was also investigated. Qualitative agreement between fission yields calculated with SkM* and UNEDF1_{HFB} is observed, however, our results are not in agreement with BSM. This shows the usefulness of multimodal fission for differentiating between models. Given the computational costs of computing fission lifetimes and yields within the framework presented, I highlight the need for emulators to study fissioning r -process nuclei with quantified uncertainties and recent efforts build DFT emulators. I co-authored Ref. [238] where we developed of a neural network to emulate PESs and inertia tensors for to be used for large scale studies of spontaneous fission. Specifically, I contributed to the conception of the idea of using neural networks for emulation, development of the method used to train the neural network including the sampling of data, and network architecture.

Chapter 5. The Instanton Approach to Nuclear Fission Lifetimes

In section 3.1, we derived the adiabatic collective tunneling expressions for spontaneous fission. This required us to assume there exists a reparameterized minimum energy trajectory $\mathcal{R}^{(0)}(\vec{q}(t))$ that depends smoothly on time-dependent collective coordinates $\vec{q}(t)$. The collective coordinates are chosen a priori. These assumptions restrict the dynamics and do not include non-adiabatic features which are known to present in fission [177]. Additionally, the computational complexity of the adiabatic approach scales exponentially with the number of collective coordinates. The consequences of these assumptions systematically limit the accuracy of the calculated lifetime. A theory capable of computing lifetimes that does not require such limiting assumptions is desired.

Fission is a dynamic process and must incorporate quantum tunneling to account for decays. If a nucleus is unstable with respect to fission, the ground state must be metastable and not in the spectrum of the system's Hamiltonian. Due to metastability, a fissioning nucleus may be regarded as an open quantum system [138, 245]. If a system external to the nucleus is not considered, the decay results in non-unitary real-time evolution which represents information leaving the isolated system. Tunneling is one manifestation of this non-unitary evolution.

Decays in quantum mechanics are often treated with time-independent semi-classical approximations such as WKB theory. Understanding this phenomena in real-time setting is not entirely understood. Many-body dynamics can be derived from the DFM action (Eq. 3.1). The stationary points of this action are interpreted as classical trajectories and quantum tunneling is obscured. However, the meaning of "classical" in this context is not

clear. In WKB theory, classical mechanics emerges as a leading order term in the asymptotic expansion of the wavefunction in powers of \hbar as $\hbar \rightarrow 0$. From the expansion, the classical to quantum transition is more clearly displayed. However, the transition from classical to quantum is not completely understood, and is a widely studied foundational problem in quantum mechanics (See Ref. [245] for a review). Quantum decoherence, interference, and measurement give meaning to the notion of a classical trajectory and these concepts are more clearly represented within the sum over histories approach to quantum mechanics [246].

This chapter explores the classicality of mean-field fission trajectories within the sum over histories approach. Following closely the work in Refs. [247–251], we develop a mean-field description of tunneling in real and imaginary time that generalizes the adiabatic approach developed in section 3.1. First, we overview the path integral in single particle mechanics. Then, we derive a functional integral representation of a transition amplitude for a non-relativistic many-body system using the Hubbard-Stratonovich (HS) transformation in real and imaginary time. We extend these results to meson exchange models applicable to fission. A general algorithm is proposed to search for mean-field instantons for the non-relativistic and meson models.

5.1 Path Integral Representation

To introduce the sum over histories approach, we overview the path integral representation for single particle quantum mechanics in one spatial dimension. For detailed pedagogical introductions, see Refs. [246, 252–257].

A solution to the time-dependent Schrödinger equation can be expressed in terms of a

Green's function¹ G ,

$$\Psi(x_f, t) = \int dx_i G(x_f, x_i, t) \Psi(x_i, t) \quad (5.1)$$

where the Green's function is represented in the path integral formalism [246]:

$$G(x_f, x_i, t) = \int_{x(0)=x_i}^{x(t)=x_f} Dx e^{iS[x]}, \quad S[x] = \int_0^t dt \frac{1}{2} m \dot{x}^2 - V(x). \quad (5.2)$$

The leading order contributions to G satisfy $\delta S[x] = 0$, that is, Newtonian equations of motion

$$m\ddot{x} = -\frac{dV}{dx}. \quad (5.3)$$

Recently, Refs. [259, 260] have proposed redefining the Green function in Eq. (5.2) using Picard-Lefschetz theory [261, 262]. In this reformulation, the pathways $x(t)$ are analytically continued into the complex plane and the classical histories satisfying $\delta S[x] = 0$ play a central role in the evaluation of the path integral. Saddle points of S are recognized as the leading order term in an \hbar expansion of the path integral as $\hbar \rightarrow 0$ making the connection to classical physics clear. In the Picard-Lefschetz formulation, the saddle points of S are generally complex. Complex saddles have been proposed to contribute to the path integral in the past [257], however, more recently they have been shown to be related to real-time quantum tunneling at the classical level [259, 260, 263–268]. Fig. 5.1 shows a simple illustration of a classical trajectory connecting $x_0 = 0$ and $x_f = 5.5$; a point outside the barrier in the cubic potential $V(x) = \frac{1}{2}x^2 - \frac{1}{3}x^3$. We see there exists a pathway in the complex

¹See Ref. [258] for nomenclature.

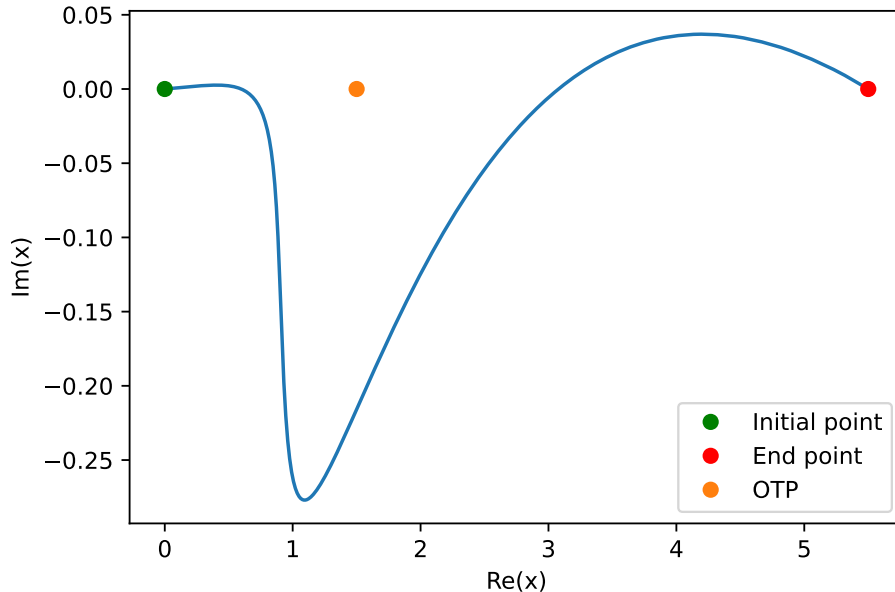


Figure 5.1: An example of a real-time saddle point of the action with a cubic potential. The outer turning point (OTP) of the barrier is denoted with the orange circle.

position plane that connects the two sides of the barrier and contributes to the transition amplitude. This suggests that for dynamics, complex saddle points can exist and extensions to semi-classical approximations in a many-body theory of dynamics should take them into consideration. These saddle points were at least partially understood to play a role in mean-field formulations of S -matrix theory for mean-field nuclear dynamics [269–273]. While there has been progress in understanding tunneling in real-time, many problems still persist (see Refs. [260, 274] for examples).

Static properties of metastable quantum systems can be calculated by analytically continuing Eq. (5.2) to complex time, $t = i\tau$. In particular, the partition function can be expressed as

$$\mathcal{Z} = \text{Tr} \left(e^{-\hat{H}\tau} \right) = \int_{x(0)=x_i}^{x(\beta_T)=x_f} Dx e^{-S[x]}, \quad S_E[x] = \int_0^{\beta_T} d\tau \frac{m}{2} \dot{x}^2 + V(x) \quad (5.4)$$

where we identify periodic imaginary time with the thermodynamic β , $\tau = \beta = 1/k_b T$. The partition function is now represented as a sum over all periodic trajectories starting and ending at a point x_i in imaginary time. If a system is metastable, the ground state energy is complex, $\varepsilon = E_0 - i\frac{\Gamma}{2}$ where E_0 is the real ground state energy and Γ is the decay width of the state. To leading order in \hbar , Refs. [275, 276] showed the decay width could be approximated by

$$\Gamma \propto e^{-S_E[x^*]} + \mathcal{O}(\hbar), \quad (5.5)$$

where x^* satisfies the saddle point equation:

$$m \frac{d^2 x}{d\tau^2} = + \frac{dV}{dx}, \quad x(0) = x(\beta_T) = x_i. \quad (5.6)$$

Eq. (5.6) is analogous to Eq. (5.3) but describes a particle propagating in imaginary time in an inverted potential. A periodic solution inside the inverted potential is referred to as a "bounce" trajectory comprised of an instanton (motion leading to the outer turning point) and anti-instanton (motion returning from the outer turning point back to x_i). The method of approximating the tunneling lifetime, by solving Eq. (5.6), is often referred to as the instanton method. Instantons are related to real time dynamics through analytic continuation. Refs. [263, 265] studied the analytic continuation of instantons in a double well potential. More detailed discussions and instanton examples are in Refs. [153, 252, 274–277]. The topics in the next sections contain formalism for constructing an instanton method for many-nucleon systems to describe fission.

5.2 Non-Relativistic Models

Analogous to the single particle case, we seek a sum over histories representation of the life-time for a many-body system. We first derive the semi-classical expression for the real-time transition amplitude, then analytically continue the result to imaginary time. Refs. [247, 250, 271] derived such expressions by assuming a simple two or three body Hamiltonian using the HS transformation to linearize the two or three body operators by introducing collective fields in particle-hole channel. The HS transformation leads to a semiclassical expansion which results in an effective one-body potential and is well suited for nuclear phenomenology. There are, however, limitations to this approach. First, the use of density dependent potentials is not clearly defined within the HS transformation for transition amplitudes. DFT models such as ones based on the Skyrme or Gogny energy density functionals (see 2.2) containing density dependence cannot simply be applied since the definition of a one-body density becomes ambiguous (see Refs. [89, 115]). For instance, calculating the amplitude between two arbitrary states

$$\langle \Psi_f | e^{-i\hat{H}[\rho]t} | \Psi_i \rangle, \quad (5.7)$$

where \hat{H} depends on the one-body density, yields different results depending on which state \hat{H} is applied to. This limits the number of models we can use within this framework at the current time. Progress in deriving potentials from effective actions has been made previously [78, 278, 279]. Second, the pairing field is introduced in the particle-particle channel separate from the particle-hole channel. To include fluctuations in both channels, we must integrate the overlapping domains of the fields and that can lead to over counting contributions [253,

280]. Despite these complications, we use the HS transformation in the particle-hole channel only. Extensions to include pairing in the particle-particle channel within this work are straightforward.

Assume our Hamiltonian only contains up to two-body operators and has the form,

$$\hat{H} = \sum_{p,q=1}^{\infty} f_{pq} \hat{\eta}_p^\dagger \hat{\eta}_q - \frac{1}{2} \sum_{p,q,r,s=1}^{\infty} v_{pqrs}^{(A)} \hat{\eta}_p^\dagger \hat{\eta}_s^\dagger \hat{\eta}_q \hat{\eta}_r \quad (5.8)$$

where p, q, r, s are arbitrary state labels in the occupation representation. We assume single particle orbitals (in position space),

$$\langle x|q\rangle = \begin{pmatrix} \psi_{q\tau_p\uparrow}(x) \\ \psi_{q\tau_p\downarrow}(x) \\ \psi_{q\tau_n\uparrow}(x) \\ \psi_{q\tau_n\downarrow}(x) \end{pmatrix}, \quad (5.9)$$

where $\tau_p = 1/2$ and $\tau_n = -1/2$ denote proton and neutron and \uparrow, \downarrow denote spin up and spin down respectively. f_{pq} and $v_{pqrs}^{(A)}$ are one-body and two-body anti-symmetrized matrix elements respectively in a generic basis defined as

$$f_{pq} = \langle p | \hat{f} | q \rangle, \quad v_{pqrs}^{(A)} = \langle pq | \hat{v} | rs \rangle - \langle pq | \hat{v} | sr \rangle, \quad (5.10)$$

where the superscript (A) indicates the anti-symmetrized matrix element. Define the one-body density operator as $\hat{\rho}_{pq} = \hat{\eta}_p^\dagger \hat{\eta}_q$,

$$\hat{H} = \sum_{pq=1}^{\infty} f_{pq} \hat{\rho}_{pq} - \frac{1}{2} \sum_{pqrs=1}^{\infty} v_{pqrs}^{(A)} \hat{\rho}_{ps} \hat{\rho}_{qr} = \hat{K} + \hat{V}. \quad (5.11)$$

5.2.1 Transition Amplitudes

In the Schrödinger picture, the time evolution operator $U(t_f, t_0)$ can be discretized into small time steps Δt ,

$$U(t_f, t_0) = \hat{\mathcal{T}} e^{-i \int_{t_0}^{t_f} \hat{H}(t) dt} \approx e^{-i \hat{H} \Delta t} \approx e^{-i \hat{K} \Delta t} e^{-i \hat{V} \Delta t} + \mathcal{O}(\Delta t) \quad (5.12)$$

as $\Delta t \rightarrow 0$. $\hat{\mathcal{T}}$ is the time-ordering operator. The interaction \hat{V} can be linearized in $\hat{\rho}$ using the HS transformation. To perform this transformation, we insert the functional form of the Dirac delta function [254, 281]

$$1 = \int D\sigma \delta[\sigma(t) - \rho] = \int D\sigma \int d\xi e^{i\xi(\sigma(t) - \rho)} \quad (5.13)$$

at every time slice t_k and integrate out the ξ variables,

$$\begin{aligned} \exp\left(i \frac{\Delta t}{2} \sum_{pqrs} v_{pqrs}^{(A)} \hat{\rho}_{ps} \hat{\rho}_{qr}\right) &= \sqrt{\det\left(\Delta t v_{pqrs}^{(A)}\right)} \int \prod_{ps} \frac{d\sigma_{ps}(t_k)}{\sqrt{2\pi i}} \\ &\times \exp\left(-\frac{i\Delta t}{2} \sum_{pqrs} \sigma_{ps}(t_k) v_{pqrs}^{(A)} \sigma_{qr}(t_k) + i\Delta t \sum_{pqrs} \sigma_{ps}(t_k) v_{pqrs}^{(A)} \hat{\rho}_{qr}\right). \end{aligned} \quad (5.14)$$

Taking the limit as the number of time steps $N \rightarrow \infty$ and $\Delta t \rightarrow 0$, the time-evolution operator has the form,

$$\begin{aligned} \hat{\mathcal{T}} e^{-i \int_{t_0}^{t_f} \hat{H}(t) dt} &= \\ \int \prod_{rs} D\sigma_{rs} \hat{\mathcal{T}} \exp\left(-\frac{i}{2} \int_{t_0}^{t_f} dt \sum_{pqrs} \sigma_{rs}(t) v_{rpqs}^{(A)} \sigma_{pq}(t)\right) \exp\left(i \int_{t_0}^{t_f} \hat{h}[\sigma] dt\right), \end{aligned} \quad (5.15)$$

where the integral measure is defined as

$$\prod_{ps} D\sigma_{ps} = \lim_{\substack{\Delta t \rightarrow 0 \\ N \rightarrow \infty}} \prod_{k=1}^N \sqrt{\det \left(\Delta t v_{pqrs}^{(A)} \right)} \prod_{ps} \frac{d\sigma_{ps}}{\sqrt{2\pi i}}. \quad (5.16)$$

The ‘‘mean-field’’ Hamiltonian $\hat{h}[\sigma]$ has the form

$$\hat{h}[\sigma] = \sum_{pq} \left(f_{pq} - \sum_{rs} \sigma_{rs}(t) v_{rppqs}^{(A)} \right) \hat{\rho}_{pq}. \quad (5.17)$$

This is recognized as the Hartree-Fock Hamiltonian expressed in an arbitrary single particle basis [34]. The transition amplitude between arbitrary initial and final many-body states $|\Psi_i\rangle$ and $|\Psi_f\rangle$ is

$$\langle \Psi_f | \hat{\mathcal{T}} e^{-i \int_{t_0}^{t_f} \hat{H}(t) dt} | \Psi_i \rangle = \int \prod_{rs} D\sigma_{rs} e^{i S_{\text{eff}}[\sigma]}, \quad (5.18)$$

where we define the effective action $S_{\text{eff}}[\sigma]$ as

$$S_{\text{eff}}[\sigma] = -\frac{1}{2} \int_{t_0}^{t_f} dt \sum_{pqrs} \sigma_{rs}(t) v_{rppqs}^{(A)} \sigma_{pq}(t) - i \ln \left[\langle \Psi_f | \hat{\mathcal{T}} \exp \left(i \int_{t_0}^{t_f} \hat{h}[\sigma] dt \right) | \Psi_i \rangle \right]. \quad (5.19)$$

It is important to note that the effective action S_{eff} is in general a complex valued function.

The saddle point approximation yields,

$$\langle \Psi_f | \hat{\mathcal{T}} e^{-i \int_{t_0}^{t_f} \hat{H}(t) dt} | \Psi_i \rangle \sim e^{i S_{\text{eff}}[\sigma^*]}, \quad (5.20)$$

where σ^* is a solution to $\delta S[\sigma] = 0$:

$$\sigma_{pq}^*(t) = \frac{\langle \Psi_f | \hat{U}[t_f, t; \sigma] \hat{\rho}_{pq} \hat{U}[t, t_0; \sigma] | \Psi_i \rangle}{\langle \Psi_f | \hat{U}[t_f, t_0; \sigma] | \Psi_i \rangle}. \quad (5.21)$$

Define time dependent states,

$$|\Psi_i(t)\rangle = U(t, t_0; \sigma) |\Psi_i\rangle, \quad |\Psi_f(t)\rangle = U^\dagger(t_f, t; \sigma) |\Psi_f\rangle. \quad (5.22)$$

Note that $U^\dagger(t_f, t; \sigma)$, $t_f > t$, describes backward time propagation from t_f to t .

$$\sigma_{pq}^*(t) = \frac{\langle \Psi_f(t) | \hat{\rho}_{pq} | \Psi_i(t) \rangle}{\langle \Psi_f(t) | \Psi_i(t) \rangle}. \quad (5.23)$$

The saddle point is the time evolved expectation of the reduced one-body density matrix.

Suppose $|\Psi_i\rangle$ and $|\Psi_f\rangle$ are single Slater determinants constructed from A orbitals in position space $\{\phi^{(i)}(x)\}$ and $\{\psi^{(f)}(x)\}$ respectively. The saddle point in position space is

$$\sigma^*(x_1, x_2, t) = \frac{\langle \Psi_f(t) | \hat{\rho}(x_1, x_2) | \Psi_i(t) \rangle}{\langle \Psi_f(t) | \Psi_i(t) \rangle}. \quad (5.24)$$

Assuming $|\Psi_i\rangle$ and $|\Psi_f\rangle$ are not orthogonal and using Wick's theorem with respect to true vacuum we get,

$$\sigma^*(x_1, x_2, t) = \frac{\langle \Psi_f(t) | \hat{\rho}(x_1, x_2) | \Psi_i(t) \rangle}{\langle \Psi_f(t) | \Psi_i(t) \rangle} = \sum_{jk} \psi_j^{(f)*}(x_1, t) \phi_k^{(i)}(x_2, t) \frac{C_{jk}(U(t))}{\det(U(t))}, \quad (5.25)$$

where $\psi^{(f)}(x_1, t)$ are the orbitals of the Slater determinant $|\Psi_f(t)\rangle$ and $\phi^{(i)}(x_2, t)$ are the orbitals of the Slater determinant $|\Psi_i(t)\rangle$. The matrix C_{jk} is the cofactor matrix of the

transformation matrix U ,

$$U_{jk}(t) = \int d^3x \psi_j^{(f)*}(x, t) \phi_k^{(i)}(x, t), \quad C_{jk}(t) = (-1)^{2j+k} M_{jk}(t), \quad (5.26)$$

M_{jk} is the matrix of minors of U . The final and initial state single particle orbitals evolve according to

$$-i\hbar \frac{\partial \psi_j^{(f)}}{\partial t} = h[\sigma] \psi_j^{(f)}, \quad i\hbar \frac{\partial \phi_k^{(i)}}{\partial t} = h[\sigma] \phi_k^{(i)} \quad (5.27)$$

with final and initial conditions $\psi_j^{(f)}(x_1, t_f) = \psi_j(x_1)$ and $\phi_k^{(i)}(x_2, t_0) = \phi_k(x_2)$ respectively.

These expressions are to be used for real-time mean-field dynamics.

The Hartree-Fock equations emerge as a special case. Let $|\Psi_f\rangle = |\Psi_i(t_f)\rangle$. The effective action is then

$$S_{\text{eff}}[\sigma] = -\frac{1}{2} \int_{t_0}^{t_f} dt \sum_{pqrs} \sigma_{rs}(t) v_{rpqs}^{(A)} \sigma_{pq}(t) - i \ln \left[\langle \Psi_i(t_f) | \hat{\mathcal{T}} \exp \left(i \int_{t_0}^{t_f} \hat{h}[\sigma] dt \right) | \Psi_i \rangle \right] \quad (5.28)$$

The saddle points in this case are

$$\sigma^*(x, t) = \frac{\langle \Psi_i(t) | \hat{\rho}(x) | \Psi_i(t) \rangle}{\langle \Psi_i(t_f) | \Psi_i(t_f) \rangle} = \sum_{k=1}^A \frac{\bar{\phi}_k(x, t) \phi_k(x, t)}{\langle \Psi_i(t_f) | \Psi_i(t_f) \rangle}, \quad (5.29)$$

where the orbitals evolve according to

$$i \frac{\partial}{\partial t} \phi_k(x, t) = \hat{h}[\sigma] \phi_k(x, t), \quad \phi_k(x, t_0) = \phi_k(x). \quad (5.30)$$

This defines the time-dependent Hartree-Fock (TDHF) equations and the action takes the form,

$$\begin{aligned}
S_{\text{eff}}[\sigma] &= -\frac{1}{2} \int_{t_0}^{t_f} dt \sum_{pqrs} \sigma_{rs}(t) v_{rpqs}^{(A)} \sigma_{pq}(t) - i \ln \left[\langle \Psi_i(t_f) | \hat{\mathcal{T}} \exp \left(i \int_{t_0}^{t_f} \hat{h}[\sigma] dt \right) | \Psi_i \rangle \right] \\
&= -\frac{1}{2} \int_{t_0}^{t_f} dt \sum_{pqrs} \sigma_{rs}(t) v_{rpqs}^{(A)} \sigma_{pq}(t) - i \ln \left[\langle \Psi_i(t_f) | \Psi_i(t_f) \rangle \right]
\end{aligned} \tag{5.31}$$

If $\Psi_i(t_f)$ is normalized, then the log term vanishes and S_{eff} is a real number. The transition probability is

$$\left| \langle \Psi_i(t_f) | \hat{\mathcal{T}} e^{-i \int_{t_0}^{t_f} \hat{H}(t) dt} | \Psi_i \rangle \right|^2 \sim |e^{i S_{\text{eff}}[\sigma^*]}|^2 = 1. \tag{5.32}$$

The TDHF equation emerges as a deterministic classical equation organized by the asymptotic expansion of the transition amplitude in powers of \hbar . Solutions to the TDHF equations result in a real effective action and cannot correspond to any tunneling trajectory if the time-evolved state $|\Psi_i(t)\rangle$ is normalized. If the many-body states are not normalized, the action can become complex.

5.2.2 The Bounce Equations

The sum over histories representation of tunneling in nuclear fission has been previously explored in a few studies [249, 251, 280, 282–285]. Our discussion closely follows Refs. [249] and [251]. To calculate the lifetime of a metastable system, the quantity of interest is the Fourier transform of the resolvent operator trace,

$$\text{Tr} \left(\frac{1}{\hat{H} - E} \right) = \int dt \text{Tr} \left(e^{i\hat{H}t} \right) e^{-iEt} \tag{5.33}$$

where the trace is performed over the entire Fock space \mathcal{F} . Continuing to imaginary time, we recognize this expression as the Fourier transform of the partition function,

$$\text{Tr} \left(\frac{1}{\hat{H} - E} \right) = \int dt \mathcal{Z} e^{-E\tau}, \quad \mathcal{Z} = \text{Tr} \left(e^{-\tau \hat{H}} \right) \quad (5.34)$$

To calculate the lifetime we look for complex energy poles in the Fourier transform of \mathcal{Z} . Performing a trace over \mathcal{F} is computationally infeasible since this is equivalent to solving the nuclear many-body problem. Similar to what was done in section 3.1, we restrict the trace of the resolvent operator to an A -particle subspace of \mathcal{F} spanned by a complete basis of Slater determinants $\{|\Psi_n\rangle\}$,

$$\text{Tr} \left(e^{-\beta \hat{H}} \right) = \sum_n \langle \Psi_n | e^{-\beta \hat{H}} | \Psi_n \rangle. \quad (5.35)$$

Each term in the trace can be represented as a sum over histories of a collective field σ by performing the HS transformation introduced in section 5.2,

$$\text{Tr} \left(e^{-\beta \hat{H}} \right) = \int D\sigma e^{-S_{\text{eff}}^{(E)}[\sigma]}, \quad (5.36)$$

where the superscript (E) denotes the Euclidean action and is defined as

$$S_{\text{eff}}^{(E)}[\sigma] = \frac{1}{2} \int_{\tau_0}^{\tau_f} d\tau \sum_{pqrs} \sigma_{rs}(\tau) v_{rpqs}^{(A)} \sigma_{pq}(\tau) - \ln \left[\sum_n \langle \Psi_n | \hat{\mathcal{T}} e^{-\int_{\tau_0}^{\tau_f} d\tau \hat{h}[\sigma]} | \Psi_n \rangle \right]. \quad (5.37)$$

σ satisfies periodic boundary conditions $\sigma(\tau_0 + \beta_T) = \sigma(\tau_0)$ for $\beta_T = \tau_f - \tau_0$. The saddle point equations $\delta S_{\text{eff}}^{(E)} = 0$, are

$$\sigma^*(x, \tau) = \sum_n \sum_{k=1}^A \frac{\bar{\phi}_{n_k}(x, \tau) \phi_{n_k}(x, \tau)}{\mathcal{N}}, \quad \mathcal{N} = \sum_m \langle \Psi_m | e^{-\int_{\tau_0}^{\tau_f} d\tau \hat{h}[\sigma]} e^{-\int_{\tau_0}^{\tau} d\tau \hat{h}[\sigma]} | \Psi_m \rangle, \quad (5.38)$$

where the orbitals $\phi_{n_k}(x, \tau)$ evolve according to the imaginary time-dependent HF equation,

$$\frac{\partial}{\partial \tau} \phi_{n_k}(x, \tau) = \hat{h}[\sigma] \phi_{n_k}(x, \tau), \quad \phi_{n_k}(x, \tau_0) = \phi_{n_k}(x, \tau_f) = \phi_{n_k}(x). \quad (5.39)$$

If the state $\phi_{n_k}(x, \tau)$ is to be normalized, we require

$$\int d^3x \bar{\phi}_{n_k}(x, \tau) \phi_{n_k}(x, \tau) = \int d^3x \phi_{n_k}(x, 0) e^{\hat{h}[\sigma]\tau} e^{-\hat{h}[\sigma]\tau} \phi_{n_k}(x, 0) = 1. \quad (5.40)$$

This implies the conjugate orbital is the imaginary time reversed state, $\bar{\phi}_{n_k}(\tau) = \phi_{n_k}(-\tau)$ and evolves according to

$$-\frac{\partial}{\partial \tau} \phi_{n_k}(x, \tau) = \hat{h}[\sigma] \phi_{n_k}(x, \tau), \quad \phi_{n_k}(x, \tau_0) = \phi_{n_k}(x, \tau_f) = \phi_{n_k}(x). \quad (5.41)$$

Eq. (5.41) resembles an inverse diffusion equation and is not mathematically well-posed as initial value problem [286, 287]. The mean-field σ^* is well defined and finite since it is a product of exponentially growing and decaying functions. However, in practical calculations, constructing σ^* is numerically unstable. Rather than considering the imaginary time evolution as an initial value problem, we transform the evolution into an eigenvalue-eigenvector

problem.

Considering the partition function, assume $|\Psi_n\rangle$ is an eigenstate of the evolution operator $\hat{\mathcal{T}}e^{-\int_{\tau_0}^{\tau_f} d\tau \hat{h}[\sigma]}$. The sum in the second term of Eq. (5.37) becomes,

$$\sum_n \langle \Psi_n | \hat{\mathcal{T}}e^{-\int_{\tau_0}^{\tau_f} d\tau \hat{h}[\sigma]} | \Psi_n \rangle = \sum_n \exp\left(-\sum_{k=1}^A \alpha_{n_k}[\sigma]\right). \quad (5.42)$$

The trace over all A -particle Slater determinants becomes a sum over all possible combinations of eigenvalues α_{n_k} . The partition function is then

$$\begin{aligned} \mathcal{Z} &= \sum_n \int D\sigma \exp\left(\frac{1}{2} \int_{\tau_0}^{\tau_f} d\tau \sum_{pqrs} \sigma_{rs}(\tau) v_{rpqs}^{(A)} \sigma_{pq}(\tau) - \sum_{k=1}^A \alpha_{n_k}[\sigma]\right) \\ &= \sum_n \int D\sigma e^{-S_{\text{eff}}^{(E)}[\sigma, \alpha_n]} \end{aligned} \quad (5.43)$$

The sum over n scales exponentially and is infeasible to compute. In the low temperature limit ($\tau \rightarrow \infty$), the lowest action configuration of α_{n_k} becomes dominant. This will truncate the sum over n and will reduce the number of combinations of eigenvalues needed in the sum.

To diagonalize $\hat{\mathcal{T}}e^{-\int_{\tau_0}^{\tau_f} d\tau \hat{h}[\sigma]}$ for all $\tau \in [\tau_0, \tau_f]$, consider the action of the time-evolution operator

$$\hat{U}[\sigma, \beta_T] = \hat{\mathcal{T}}e^{-\int_{\tau_0}^{\tau_f} d\tau \hat{h}[\sigma]} \quad (5.44)$$

on a single particle orbital,

$$|\phi_{n_k}(\tau_f)\rangle = \hat{U}[\sigma, \beta_T] |\phi_{n_k}(\tau_0)\rangle. \quad (5.45)$$

We transform ϕ_k into the Floquet form [288, 289],

$$|\phi_{n_k}(\tau)\rangle = e^{-\alpha_{n_k}[\sigma, \beta_T]\tau} |\chi_{n_k}(\tau)\rangle, \quad (5.46)$$

where α_{n_k} are Floquet indices. The states $|\chi_{n_k}\rangle$ are imaginary time-periodic $|\chi_{n_k}(\tau + \beta_T)\rangle = |\chi_{n_k}(\tau)\rangle$. For any $\tau < \beta_T$, the orbitals evolve according to

$$U(\tau, 0)|\phi_{n_k}(0)\rangle = e^{-\alpha_{n_k}[\sigma, \tau]\tau} |\phi_{n_k}(0)\rangle = e^{-\alpha_{n_k}[\sigma, \tau]\tau} |\chi_{n_k}(0)\rangle. \quad (5.47)$$

Using the Floquet form of the single particle orbitals leads to an eigenvalue problem,

$$\left(\partial_\tau - \hat{h}[\sigma]\right)\chi_{n_k}(x, \tau) = \alpha_{n_k}[\sigma, \beta_T]\chi_{n_k}(x, \tau) \quad (5.48)$$

with boundary conditions

$$\chi_{n_k}(x, \tau_0) = \chi_{n_k}(x, \tau_f) = \chi_{n_k}(x), \quad \lim_{|x| \rightarrow \infty} \chi_{n_k}(x, \tau) = 0. \quad (5.49)$$

This defines a non-hermitian eigenvalue problem since σ is complex. Eq. (5.48) is the Floquet representation of Eq. (5.39). Saddle points of $S_{\text{eff}}^{(E)}$ are derived in the same way as the real time case,

$$\sigma(x, \tau) = \sum_{k=1}^A \chi_k(x, -\tau)\chi_k(x, \tau), \quad (5.50)$$

which is the local one-body density matrix in imaginary time.

Ref. [249] solved Eq. (5.48) using the self-consistent mean-field theory method by adding

constrains on multipole moments to get non-trivial solutions. In section 5.4, we propose an alternative algorithm to find saddle points of the effective action in Eq. (5.43) that avoids the self-consistent mean-field method. Despite developing a new algorithm to find mean-field bounce trajectories, the number of non-relativistic models we can use for fission lifetime estimations is currently small. In the next section, we extend the formalism developed thus far to meson exchange models.

5.3 Meson Exchange Models

The Walecka model [290] and the NL3 model [291] are two meson exchange models that have been used extensively to predict nuclear observables (see Ref. [292] for a review). Both of these models have been shown to reduce to Skyrme-like effective potentials in the low momentum limit [291]. To extend the formalism developed in section 5.2, we consider a Yukawa theory with a scalar-isoscalar σ meson with electromagnetic interactions. The formalism presented here can be extended to include additional mesons in a straightforward way. The classical field Lagrangian under consideration in $(+, -, -, -)$ Minkowski metric signature² is

$$\begin{aligned} \mathcal{L} = & \bar{\Psi} \left(i\gamma^\mu \partial_\mu - M - g_\sigma \sigma - e\gamma_\mu A^\mu \left(\frac{1 + \tau_3}{2} \right) \right) \Psi \\ & + \frac{1}{2} \partial_\mu \sigma \partial^\mu \sigma + \frac{1}{2} m_\sigma^2 \sigma^2 - \frac{1}{3} g_2 \sigma^2 - \frac{1}{4} g_3 \sigma^4 \\ & - \frac{1}{4} F_{\mu\nu} F^{\mu\nu}. \end{aligned} \tag{5.51}$$

²Note we use Greek indices to label spacetime coordinates 0,1,2,3 and Latin indices to label spatial coordinates 1,2,3.

The field Ψ is a 8×1 spinor field of the form

$$\Psi = \begin{pmatrix} \psi_{\tau_p} \\ \psi_{\tau_n} \end{pmatrix} \quad (5.52)$$

where $\tau_p = 1/2$ and $\tau_n = -1/2$ label proton and neutron respectively. $\psi_{\tau_p}, \psi_{\tau_n}$ are Dirac spinors, M is the bare nucleon mass, and γ^μ are the gamma matrices (see Ref. [254]). The operator $\frac{1}{2}(1 + \tau_3)$ is the isospin projection operator onto the proton field ψ_{τ_p} . A^μ is the electromagnetic four-potential, the electromagnetic field tensor is given by

$$F_{\mu\nu} = \partial_\mu A_\nu - \partial_\nu A_\mu, \quad (5.53)$$

and σ is a scalar-isoscalar meson. This model contains coupling constants g_σ, g_2, g_3 taken to be fit parameters. Standard field quantization using the coherent basis can be used to derive a sum over field histories representation of the partition function [253, 255, 256, 280].

To describe finite nuclear systems, two challenges must be overcome in the field representation. First, the couplings are not known and must be fit to experimental data. It has been shown that the couplings are large, and perturbative expansions in powers of coupling constants are dubious. Second, the fermion fields must be constrained such that the number of protons and neutrons are fixed. Particle number constraints are commonly used in the canonical ensemble approach in lattice field theory [293–296]. This approach requires repeated Fourier transforms of the fermion functional determinant, which for large systems becomes numerically challenging to perform. While the canonical ensemble method has been successfully used to study finite density quantum chromodynamics, we do not use this method in this work. Instead we pursue an occupation representation similar to what was

used in section 5.2. This approach leads to the “relativistic mean-field theory” approach for finite nuclei [72, 73, 290–292, 297, 298]. We start with deriving the expression for a real time transition amplitude between two many-body states.

5.3.1 Transition Amplitudes

In the Hamiltonian picture, we consider fermions coupled to a scalar meson and the electromagnetic field. Define the Fock space

$$\mathcal{F} = \mathcal{F}_f \otimes \mathcal{F}_b, \quad (5.54)$$

where \mathcal{F}_f is the fermion sector Fock space and \mathcal{F}_b is the boson sector Fock space. To define a many-body Hamiltonian operator on \mathcal{F} , consider a many-body time-independent Dirac equation in position space,

$$\sum_{k=1}^A \left((\hat{h}_{\text{Dirac},k} + \beta\sigma(x_k, t) + e\beta\gamma^\mu A_\mu(x_k, t) \left(\frac{1 + \tau_3}{2} \right) \right) \psi(x_1, x_2, \dots, x_A) = E\psi(x_1, x_2, \dots, x_A) \quad (5.55)$$

where the Dirac Hamiltonian is

$$\hat{h}_{\text{Dirac},k} = -i(\alpha^j \partial_j)_k + \beta M_k \quad (5.56)$$

σ is the scalar meson field, and A_μ is the electromagnetic four potential. $\alpha^i = \gamma^0 \gamma^i$ and $\beta = \gamma^0$ are the Dirac matrices and e is the electric charge. Using second quantization, we introduce fermionic operators,

$$\hat{\eta}_p^\dagger = \hat{\eta}_p^\dagger \otimes \hat{I}_b, \quad \text{and} \quad \hat{\eta}_p = \hat{\eta}_p \otimes \hat{I}_b, \quad (5.57)$$

where \hat{I}_b is the identity operator on the boson sector \mathcal{F}_b . The many-body Dirac equation can now be written as

$$\hat{H}_\Psi = \sum_{pq} \int d^3x \bar{\psi}_p(x) \left(-i\alpha^k \partial_k + \beta M + g_\sigma \beta \hat{\sigma}(x, t) + e\beta\gamma^\mu A_\mu(x_k, t) \left(\frac{1 + \tau_3}{2} \right) \right) \psi_q(x) \hat{\eta}_p^\dagger \hat{\eta}_q. \quad (5.58)$$

Here, the single particle orbitals are isospin doublets of Dirac spinors,

$$\langle x|q\rangle = \psi_q(x) = \begin{pmatrix} \phi_{q\tau p\uparrow}(x) \\ \phi_{q\tau p\downarrow}(x) \\ \chi_{q\tau p\uparrow}(x) \\ \chi_{q\tau p\downarrow}(x) \\ \psi_{q\tau n\uparrow}(x) \\ \psi_{q\tau n\downarrow}(x) \\ \chi_{q\tau n\uparrow}(x) \\ \chi_{q\tau n\downarrow}(x) \end{pmatrix}. \quad (5.59)$$

ϕ and χ denote particle and anti-particle wave-functions respectively. The many-body Hamiltonian under consideration is then

$$\begin{aligned} \hat{H}_{\text{Yuk}} = \sum_{pq} \int d^3x \bar{\psi}_p(x) \left(-i\alpha^j \partial_j + \beta M + \beta g_\sigma \hat{\sigma}(x, t) + e\beta\gamma^\mu A_\mu(x_k, t) \left(\frac{1 + \tau_3}{2} \right) \right) \psi_q(x) \hat{\eta}_p^\dagger \hat{\eta}_q \\ + \hat{H}_\sigma + \hat{H}_{\text{e.m.}}. \end{aligned} \quad (5.60)$$

The σ and A^μ are quantized using equal-time canonical quantization. The σ Hamiltonian is

$$\hat{H}_\sigma = \int d^3x \left[\frac{1}{2} \hat{\pi}_\sigma^2 + \frac{1}{2} (\partial_i \hat{\sigma})^2 + \frac{1}{2} m^2 \hat{\sigma}^2 + \frac{1}{3} g_2 \hat{\sigma}^3 + \frac{1}{4} g_3 \hat{\sigma}^4 \right] \quad (5.61)$$

and the electromagnetic Hamiltonian is

$$\hat{H}_{\text{e.m.}} = \int d^3x \frac{1}{2} (\hat{E}^2 + \hat{B}^2) + \int d^3x \vec{J} \cdot \vec{A} \quad (5.62)$$

in the Coulomb gauge acting on the proton sector. We refer the reader to standard texts on scalar field and electromagnetic field quantization such as Ref. [252] for more details.

Using the Hamiltonian Eq. (5.60), we express the real-time transition amplitude

$$\langle \Psi_f | \mathcal{T} e^{-i\hat{H}_{\text{Yuk}} t} | \Psi_i \rangle = \int D\sigma D A^\mu e^{iS_{\text{eff}}[\sigma, A^\mu]}, \quad (5.63)$$

where the action is

$$S_{\text{eff}}[\sigma, A^\mu] = S[\sigma] + S[A^\mu] - i \ln [\langle \Psi_f | \hat{\mathcal{T}} e^{-i \int_{t_0}^t dt \hat{h}[\sigma, A^\mu]} | \Psi_i \rangle]. \quad (5.64)$$

The mean-field Hamiltonian has the form,

$$\hat{h}[\sigma, A^\mu] = \int d^3x \sum_{pq} \bar{\psi}_p(x) \left(-i\alpha^k \partial_k + \beta M + g_\sigma \beta \sigma(x, t) + e\beta \gamma^\mu A_\mu(x_k, t) \left(\frac{1 + \tau_3}{2} \right) \right) \psi_q(x) \hat{\eta}_p^\dagger \hat{\eta}_q \quad (5.65)$$

and the σ field action is

$$S[\sigma] = \int d^4x \frac{1}{2} \partial_\mu \sigma \partial_\mu \sigma - \frac{1}{2} m^2 \sigma^2 - \frac{1}{3} g_2 \sigma^3 - \frac{1}{4} g_3 \sigma^4 \quad (5.66)$$

and the electromagnetic action is

$$S[A^\mu] = -\frac{1}{4} F_{\mu\nu} F^{\mu\nu}. \quad (5.67)$$

Appendix B contains a detailed derivation of the transition amplitude for a linear Yukawa theory that extends to the derivation of Eq. (5.63). It is interesting to compare the form of the meson effective action in Eq. (5.64) to the non-relativistic action in Eq. (5.28). If one removes the kinetic, cubic, and quartic terms of the σ action and reduce the electromagnetic interactions to Coulomb potentials in Eq. (5.64), we recover an action of the same form as the non-relativistic effective action in Eq. (5.28). Integrating out the mesons and taking a low momentum limit, results in a density dependent effective potential containing powers of ρ and a nuclear spin-orbit term.

The saddle point equations for configurations of the fields σ and A^μ are,

$$\partial_\mu \partial^\mu \sigma - m^2 \sigma - g_2 \sigma^2 - g_3 \sigma^3 = -g_\sigma \sum_{jk} \bar{\psi}_j^{(f)}(x_1, t) \phi_k^{(i)}(x_2, t) \frac{C_{jk}(U(t))}{\det(U(t))} \quad (5.68)$$

$$\partial_\mu F^{\mu\nu} = -e \sum_{jk} \bar{\psi}_j^{(f)}(x_1, t) \gamma^\nu \phi_k^{(i)}(x_2, t) \frac{C_{jk}(U(t))}{\det(U(t))} \quad (5.69)$$

$$\left(i\gamma^\mu \partial_\mu - M - g_\sigma \sigma(x, t) - e\gamma^\mu A_\mu \left(\frac{1 + \tau_3}{2} \right) \right) \phi_k^{(i)}(x, t) = 0 \quad (5.70)$$

$$\left(i\gamma^\mu \partial_\mu - M - g_\sigma \sigma(x, t) - e\gamma^\mu A_\mu \left(\frac{1 + \tau_3}{2} \right) \right) \psi_k^{(f)}(x, t) = 0 \quad (5.71)$$

where the orbitals satisfy initial and final conditions $\phi_k^{(i)}(x, 0) = \phi_k^{(i)}(x)$, $\psi_k^{(f)}(x, t_f) = \psi_k^{(f)}(x)$ respectively. These saddle point equations are of the same form as the relativistic mean-field equations where the fermion single particle orbitals are the source terms in the meson and electromagnetic saddle point equations [72, 73, 290–292, 297, 298].

5.3.2 Bounce Equations

Following the steps taken in section 5.2.2, we express the partition function as,

$$\mathcal{Z} = \int D\sigma DA^\mu e^{-S_{\text{eff}}^{(E)}[\sigma, A^\mu]}, \quad (5.72)$$

where the Euclidean effective action in imaginary time is

$$S_{\text{eff}}^{(E)} = S[\sigma] + S[A^\mu] - \ln \left[\sum_n \langle \Psi_n | \hat{\mathcal{T}} e^{-\int_{\tau_0}^{\tau_f} d\tau \hat{h}[\sigma, A^\mu]} | \Psi_n \rangle \right]. \quad (5.73)$$

We express the Euclidean effective action in terms of the eigenvalues of the time ordered mean-field operator as was done in section 5.2.2,

$$\sum_n \langle \Psi_n | \hat{\mathcal{T}} e^{-\int_{\tau_0}^{\tau_f} d\tau \hat{h}[\sigma]} | \Psi_n \rangle = \sum_n \exp \left(- \sum_{k=1}^A \alpha_{n_k}[\sigma] \right). \quad (5.74)$$

The eigenvalues α are determined by

$$\left(\gamma_E^\mu \partial_\mu - M - g_\sigma \sigma(x, \tau) - e\gamma^\mu A_\mu \left(\frac{1 + \tau_3}{2} \right) \right) \chi_{n_k}(x, \tau) = \alpha_{n_k}[\sigma, A^\mu, \beta_T] \chi_{n_k}(x, \tau), \quad (5.75)$$

where

$$|\phi_{n_k}(\tau)\rangle = e^{-\alpha_{n_k}[\sigma, A^\mu, \beta_T]\tau} |\chi_{n_k}(\tau)\rangle \quad (5.76)$$

and γ_E are the gamma matrices in Euclidean signature,

$$\gamma_E^0 = \gamma^0, \quad \gamma_E^k = i\gamma^k \quad (5.77)$$

The imaginary time saddle point equations for the σ meson are,

$$\partial_\mu \partial^\mu \sigma - m^2 \sigma - g_2 \sigma^2 - g_3 \sigma^3 = -g_\sigma \sum_{k=1}^A \chi_{n_k}(x, -\tau) \chi_{n_k}(x, \tau), \quad (5.78)$$

for the electromagnetic field,

$$\partial_\mu F^{\mu\nu} = -e \sum_{k=1}^A \chi_{n_k}(x, -\tau) \gamma^\nu \chi_{n_k}(x, \tau), \quad (5.79)$$

and for fermion single particle orbitals,

$$\left(\gamma_E^\mu \partial_\mu - M - g_\sigma \sigma(x, \tau) - e \gamma^\mu A_\mu \left(\frac{1 + \tau_3}{2} \right) \right) \phi_{n_k}(x, \tau) = \alpha_{n_k}[\sigma, \beta_T] \phi_{n_k}(x, \tau) \quad (5.80)$$

$$\left(\bar{\gamma}_E^\mu \partial_\mu - M - g_\sigma \bar{\sigma}(x, \tau) - e \gamma^\mu A_\mu \left(\frac{1 + \tau_3}{2} \right) \right) \phi_{n_k}(x, -\tau) = \bar{\alpha}_{n_k}[\sigma, \beta_T] \phi_{n_k}(x, -\tau). \quad (5.81)$$

These mean-field equations define the instanton trajectories and the fission lifetime. Inspecting the low-momentum limit, we find that the meson models easily provide sophisticated description of nuclear forces. Because of this, using a meson model is immediately capable of calculating realistic fission lifetimes using the instanton method. While the physics is extensive, the meson bounce equations (Eqs. (5.78) - (5.80)) are still nonlinear and the properties of these equations are not well studied. The self-consistent mean-field method is not expected to succeed in solving these equations as difficulties using this method were seen in the non-relativistic case. A new numerical method is needed to solve the meson

bounce equations to find bounce trajectories. In the next section, we suggest a new general algorithm for finding bounce trajectories.

5.4 Bounce Search Algorithm

One of the persisting problems with instanton or bounce trajectory searches in mean-field theory is the ineffectiveness of the self-consistent mean field approach to solve the imaginary time-dependent mean-field equations from Eq. (5.48). Additionally, construction of the mean field σ is numerically unstable due to the exponential growth and decay of the functions used to construct it. In this section, we overview a new approach that replaces the self-consistent mean-field method with a method that directly finds stationary points of a given action without needing to construct the mean-field explicitly.

The effective actions for the bounce trajectories under consideration in this work have the form,

$$S_{\text{eff}}[\sigma, A^\mu] = S[\sigma] + S[A^\mu] - \sum_{k=1}^A \alpha_k[\sigma, A^\mu]. \quad (5.82)$$

By discretizing the effective action onto a lattice, S_{eff} becomes a high dimensional function of complex variables. To find saddle points, we need to solve a set of equations

$$\vec{\nabla} S_{\text{eff}} = 0 \quad (5.83)$$

for each field. There are two primary challenges in searching for stationary points of the effective action. First, we need to solve Eq. (5.83), a very high dimensional set of non-linear equations. Second, we need to compute the eigenvalues α_k . To address the first challenge, there are techniques from lattice field theory that can be applied. One common method

used to find stationary points of the action is Newton or quasi-Newton methods [299]. These methods can be adapted to equations of complex variables and can explore the domain of S_{eff} to find saddle points. However, there is no guarantee that the saddle points found with this method are relevant. The relevance of a saddle point is determined by its intersection number [261, 262, 264]. Determining the intersection number for a saddle point is, in general, a very difficult task. Intersection numbers can be computed by solving the holomorphic flow equations over complex space [300–303]. This is also a very demanding task.

To overcome difficulties in determining the relevance of a saddle point, one can use the parallel tempering technique [304, 305] to initialize a distribution of configurations and then minimize $\text{Re}(S)$. If $\text{Re}(S)$ for the dynamic saddle point is greater than $\text{Re}(S)$ of the static solution, then the saddle point is deemed irrelevant. Using the minimal $\text{Re}(S)$ fields, we initialize a Newton or quasi-Newton method. It is also possible to use existing solutions from the adiabatic approach to fission to initialize the saddle point search.

Eigenvalues α_{n_k} need to be computed at every iteration. This requires a solution of the eigenvalue-eigenvector equation (5.48) for non-relativistic systems or equations (5.78)–(5.80) for the meson models. All these equations have periodic boundary conditions in τ and vanishing Dirichlet conditions in x defining a boundary value problem. These equations are solved using the pseudo-spectral B-Spline method [306–309] in coordinate space. Finally to find the lifetime, one needs to study the Fourier transform

$$\text{Tr}\left(\frac{1}{\hat{H} - E}\right) \sim -i \int e^{-iE\tau} e^{-S_{\text{eff}}[\sigma^*, A^{\mu*}]} d\tau \quad (5.84)$$

to search for poles in the complex energy plane.

5.5 Summary

In this chapter I developed formalism for nuclear mean-field dynamics and tunneling by extending the sum over histories approach to a many-body system. First we reviewed the sum over histories approach in single particle quantum mechanics and made the connection between complex classical trajectories and tunneling in real time. In imaginary time, Sidney Coleman's instanton formalism [153, 275, 276] was mentioned to approximate decay lifetimes for metastable states. Next, by following Ref. [249, 251], we developed a formalism for many-body dynamics using the HS transform to derive an effective action in terms of a collective variable σ in the particle-hole channel. Saddle points of the effective action in real-time yielded Hartree-Fock like equations that could in general yield trajectories resulting in a complex action. These trajectories are interpreted as tunneling trajectories. Analytic continuation of these results to imaginary time yielded bounce equations that approximate the partition function which in turn allows one to approximate complex energies of a many-body system by Fourier transform. Since nuclear DFT is not so easily applied in the non-relativistic case, we extend the formalism to a meson model consisting of a scalar-isoscalar mesons and electromagnetic interactions. Similar real-time and imaginary expressions were derived. Finally, we discussed a new algorithm to search for a bounce or instanton trajectory that replaces the self-consistent mean-field method and avoids numerical instabilities when calculating mean-fields.

Chapter 6. Future Investigations

The work presented in this thesis focused on developing numerical methods for computing fission lifetimes and yields and formalism to improve our models of nuclear fission. Building off these developments, a number of future directions are being pursued. These are outlined in this section.

6.1 Nuclear Fission Lifetimes and Yields with DFT

Within a stationary DFT framework, I developed an implementation of the nudged elastic band method into a python package called PyNEB. This was published in Ref. [159] and presented in section 3.3. This publication presents an extensible, modular tool constructed to identify least action and minimum energy pathways for arbitrary potential energy surfaces. I developed and benchmarked the numerical implementation of the nudged elastic band technique and used this package to efficiently estimate the fission mass and charge yields and lifetimes of various even-even actinides in two and three dimensional collective spaces. Additionally, I provided mathematical foundations for the application of the technique to nuclear fission by proving the equivalence between MEPs and LAPS. Further, I used this tool to identify the contributions from different fission modes in selected actinide and trans-actinide nuclei in two and three dimensional spaces in Ref. [176].

Aside from finding fission pathways in higher dimensional collective spaces, modeling fission lifetimes and yields at finite temperature is desired. Using existing DFT models [71, 310], the impact temperature has on fission half-lives and yields using the nudged elastic band method can be studied. DFT results can be compared with predictions from Landau's Fermi liquid theory [311]. Additionally, theoretical descriptions of nuclear fission at finite temperature also contain conceptual and technical difficulties [33]. Extending DFT to in-

clude continuum and internal degrees of freedom crucial for descriptions of fission at finite temperature and for nuclei far from stability [32, 71, 111, 204].

In Ref. [238], neural networks were shown to successfully emulate PESs and collective inertias across the r -process region of the nuclear chart. This accuracy translates to reasonable predictions in the half-life and the primary fission fragment yields. Further emulator development is discussed in Ref. [244]. With extensive emulators, large scale studies of fission in the r -process are possible. One impactful application of both dimensionality reduction and the DFT approach to fission is to compute fission lifetimes and yields across the r -process region of the nuclear chart to be used in reaction network calculations. This will provide some insight about the role nuclear fission plays in the nucleosynthesis of heavy and superheavy nuclei.

6.2 Instanton and Mean-field Extensions

Section 5 dealt with developing formalism in real and complex time for describing many-body tunneling at the mean-field level. Many-body transition amplitudes in real and complex time can be used to derive mean-field theories of nuclear dynamics and stability respectively. One clear future work direction is developing a complete numerical implementation of the methods mentioned in section 5.4. Extensions of the instanton framework to include pairing effects are needed for realistic fission lifetime predictions. This can be accomplished by including collective fields in the particle-particle channel when constructing the effective action with the HS transform. With numerical implementations of the instanton method, realistic calculations of fission lifetimes without the adiabatic assumption will be possible. Further, more developments are needed to improve the non-relativistic instanton formalism. Constructing effective theories from which nuclear DFT can be derived is one way to do this

[75, 78]. Extensions of the mean-field instanton dynamics formalism to include temperature and environmental effects for induced fission studies are also desired. Investigating the existence of complex saddle points in real-time nuclear dynamics can improve mean-field approximations of cross-sections vital to reaction studies.

In open quantum systems such as nuclei far from stability, couplings between nuclear degrees of freedom and an environment are essential [33, 312]. Continuum effects have shown to be crucial for understanding the structure of superheavy elements and other weakly bound nuclei [9, 71, 313]. In a broader context, the inclusion of an environment is necessary to understand quantum decoherence and the transition between classical and quantum systems [245]. Decoherence has been shown to play a role in determining quantum state lifetimes [314–317]. Considering decoherence, it is unclear if actinide and trans-actinide nuclear decays are influenced by an environment or if the environment contributes to dissipative effects in fission. Development of nuclear mean-field formalism and numerical methods that will enable studies of how environmental effects impact nuclear stability is desired.

6.3 Dimensionality Reduction for Nuclear Physics

The computational cost of static and dynamic DFT calculations makes uncertainty quantification and large scale studies difficult. The development of emulators capable of reducing the computational cost are needed. I contributed to the development of an emulator based on neural networks that can reproduce two dimensional potential energy surfaces and inertia tensors [238]. The result was successful emulation of fission yields and lifetimes for r -process nuclei. More recent applications of reduced order modeling to problems in nuclear physics have been promising [239, 240, 242–244]. I would like to explore applications of intrusive and data-driven dimensionality reduction techniques such as dynamic mode decomposition [318],

reduced basis methods [319], and parametric matrix models [320] to emulate nuclear dynamics, reaction networks and fission observables. Given the recent interest of reduced order modeling within the nuclear physics community (see for example Refs. [321–324]), I think applications of reduced order modeling techniques to emulate dynamics and nuclear observables relevant for r -process nucleosynthesis are areas that lead to impactful advancements in nuclear physics.

APPENDIX A

Minimum Energy and Least Action

Pathways

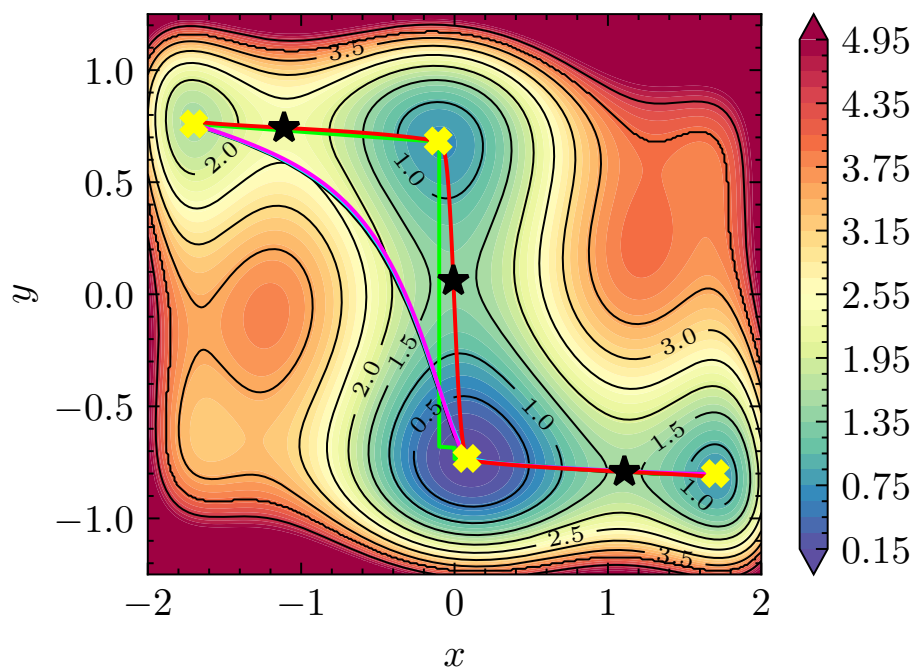


Figure A.1: The asymmetric camel-back surface $V_{CB-A}(x, y)$ with the calculated NEB-MEP (red), NEB-LAP (magenta), DPM (black), EL (cyan), and DA (lime) trajectories. Black stars indicate saddle points and yellow crosses mark local minima. Figure taken from Ref. [159]

Here we discuss the equivalence between LAPs and MEPs. Fig. A.1 shows the asymmetric camelback surface defined in Ref. [159]. We observe a significant difference in the LAPs and MEPs in their location on the PES and calculated action (see Table 3.1). The MEP is

obtained by computing the steepest descent flow on the PES, and the LAP is determined by minimizing the collective action. Similar to Ref. [325], we define the MEP as a gradient curve $\vec{\gamma}(\tau)$ satisfying the differential equation

$$\dot{\vec{\gamma}} = \sigma(\tau) \vec{\nabla} V_{\text{eff}}(\vec{\gamma}(\tau)), \quad (\text{A.1})$$

with boundary conditions $\vec{\gamma}(0) = \vec{q}_{\text{in}}$ and $\vec{\gamma}(1) = \vec{q}_{\text{out}}$. τ is an arbitrary monotonic parametrization of the curve, while $\dot{\vec{\gamma}}$ represents the local velocity of the trajectory. $\sigma(\tau)$ is a factor to account for the transformation of arc length to the parameter τ to be used in the Euler-Lagrange equations. Solutions to Eq. (A.1) define a trajectory made by a collection of steepest descents and ascents between \vec{q}_{in} and \vec{q}_{out} in terms of the parameter τ .

On the other hand, the LAP trajectory $\vec{q}(\tau)$ is derived by finding a stationary point of the action integral Eq. (3.25). By Beltrami's theorem, one can transform Eq. (3.25) into

$$\begin{aligned} \tilde{S} &= \int_0^1 \left(V_{\text{eff}}(\vec{q}) - E_0 \right) M_{\mu\nu}(\vec{q}) \dot{q}^\mu \dot{q}^\nu d\tau \\ &= \int_0^1 g_{\mu\nu} \dot{q}^\mu \dot{q}^\nu d\tau. \end{aligned} \quad (\text{A.2})$$

This action is analogous to the action of a free particle in a curved space with metric $g_{\mu\nu}$. The stationary points of this action satisfy the Euler-Lagrangian equations for the functional (3.25) however, the converse of this statement is not true. The Euler-Lagrange equations are derived by varying Eq. (A.2),

$$(V_{\text{eff}} - E_0) \ddot{\vec{q}} = \frac{1}{2} |\dot{\vec{q}}|^2 \vec{\nabla} V_{\text{eff}} - (\dot{\vec{q}} \cdot \vec{\nabla} V_{\text{eff}}) \dot{\vec{q}}, \quad (\text{A.3})$$

with the boundary condition $\vec{q}(0) = \vec{q}_{\text{in}}$ and $\vec{q}(1) = \vec{q}_{\text{out}}$. We assumed constant inertia $\mathcal{M}_{\mu\nu} \propto \delta_{\mu\nu}$.

Suppose there exists a trajectory $\vec{q}(\tau)$ satisfying $\vec{\nabla}V_{\text{eff}}[\vec{q}(\tau)] \propto \dot{\vec{q}}$, i.e, the tangent vectors of the solution $\vec{q}(\tau)$ are parallel to the surface gradient $\vec{\nabla}V_{\text{eff}}$ evaluated along the curve. Since $\vec{\nabla}V_{\text{eff}}$ and $\dot{\vec{q}}$ are parallel, Eq. (A.3) would imply that $\ddot{\vec{q}} \propto \dot{\vec{q}}$ along the trajectory. This further implies that the tangent vectors of the solution $\vec{q}(\tau)$ are always in the same direction as its acceleration. From this we conclude that in order for the MEP to also be a solution of Eq. (A.3), such trajectory $\vec{q}(\tau)$ can only be composed of straight lines. Critical points of the PES where $V_{\text{eff}} = E_0$ and $\vec{\nabla}V_{\text{eff}}$ both vanish are the only locations on the surface where the trajectory can bend non-smoothly and still obey Eq. (A.3).

These results significantly restrict the types of PESs for which an MEP can be an LAP. Such conditions on the surface can be obtained by the use of Eq. (A.1) as an ansatz for the equation of motion Eq. (A.2). We first note that, if the trajectory solves Eq. (A.1), then:

$$\ddot{\vec{\gamma}}(\tau) = \dot{\sigma} \vec{\nabla}V_{\text{eff}} + \sigma \frac{\partial \vec{\nabla}V_{\text{eff}}}{\partial \vec{\gamma}} \frac{\partial \vec{\gamma}}{\partial \tau}, \quad \frac{\partial \vec{\nabla}V_{\text{eff}}}{\partial \vec{\gamma}} \frac{\partial \vec{\gamma}}{\partial \tau} = H[\vec{\gamma}(\tau)] \dot{\vec{\gamma}}, \quad (\text{A.4})$$

where H is the Hessian matrix of second derivatives of the PES evaluated along the gradient curve $\vec{\gamma}$. For such a trajectory, the acceleration along the curve is

$$\ddot{\vec{\gamma}}(\tau) = \dot{\sigma} \vec{\nabla}V_{\text{eff}} + \sigma^2 H \vec{\nabla}V_{\text{eff}}. \quad (\text{A.5})$$

Substituting this into the the geodesic equation we obtain

$$H \vec{\nabla}V_{\text{eff}} = - \left(\frac{|\vec{\nabla}V_{\text{eff}}|^2}{2(V_{\text{eff}} - E)} + \frac{\dot{\sigma}}{\sigma^2} \right) \vec{\nabla}V_{\text{eff}}. \quad (\text{A.6})$$

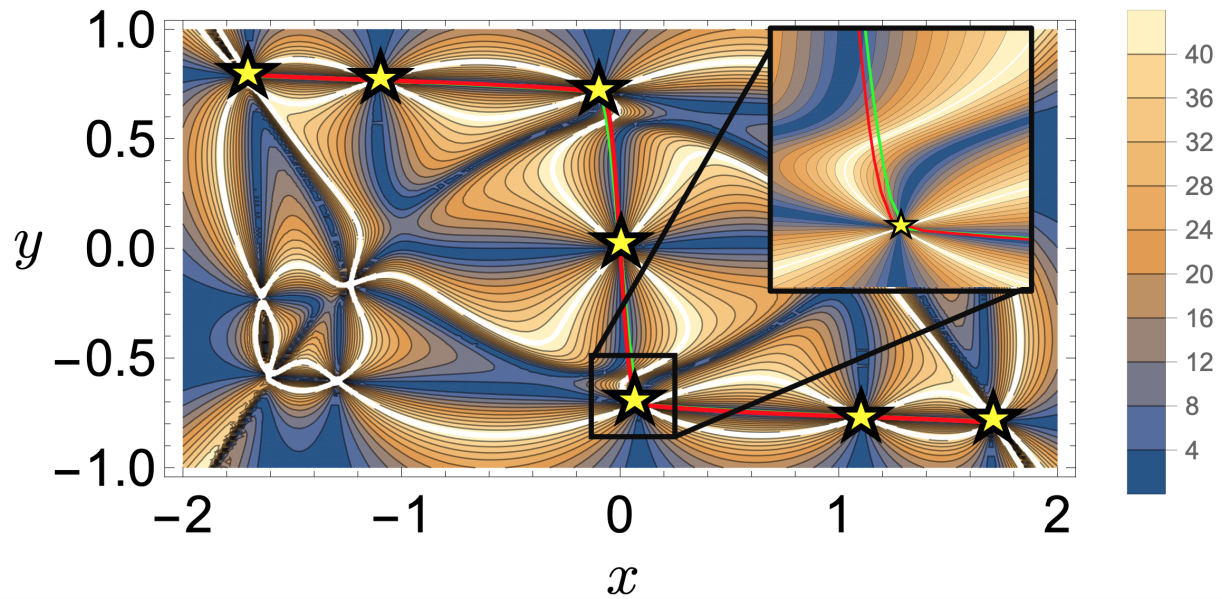


Figure A.2: Absolute value of the minimum angle (in degrees) between the gradient of V and the eigenvectors of the Hessian H for the CB-S surface. The NEB-MEP is shown in red and NEB-LAP is shown in green. The yellow stars indicate critical points of the surface. The inset zooms-in on one region where there is a slight difference in the MEP path compared to the LAP. Figure taken from Ref. [159].

We see that the gradient $\vec{\nabla}V_{\text{eff}}[\vec{\gamma}(\tau)]$ must be an eigenvector of the Hessian $H[\vec{\gamma}(\tau)]$ for all τ . This shows that the eigenvectors of H , or principal directions of the surface V_{eff} , must also be parallel to the gradient curve tangents along the trajectory. Since we know that if $\vec{\gamma}(\tau)$ is to be a solution of (A.6), then $\dot{\vec{\gamma}}(\tau) \propto \ddot{\vec{\gamma}}(\tau)$; again showing that the curve $\vec{\gamma}(\tau)$ must be a straight line. In regions where the gradient curve is not parallel to the Hessian eigenvectors, there will be an acceleration along the gradient curve perpendicular to its tangents. In this situation, the function $\vec{\gamma}(\tau)$ cannot be a solution to (A.3) since $\ddot{\vec{q}}(\tau) \not\propto \dot{\vec{q}}(\tau)$ for all τ .

Equation (A.6) allows us to identify whether an MEP is an exact stationary path by checking if the gradient descent trajectory on the surface V_{eff} misaligns at any point with the eigenvectors of the surface's Hessian H . Figure A.2 shows the smallest angle between the gradient and the Hessian's eigenvectors for the CB-S surface. In the regions where the

angle is small (stationary path can be approximated by straight lines) the MEP are LAP are close. From this analysis, we conclude that in many situations the MEP will not coincide with the LAP. However, in cases where a stationary path can be approximated by straight lines, such as in the CB-S surface, the MEP might well approximate the LAP. Since the LAP is a stationary path, small deviations from the LAP could translate into very small errors in the action value. Still, the MEP can be used for finding critical points (minima and saddles) on the surface.

APPENDIX B

Derivation of Yukawa Path Integral

This appendix explicitly derives a hybrid sum over histories approach representative of the one stated in section 5.3.1. To simplify the derivation, we only consider a linear Yukawa model described by Hamiltonian,

$$\hat{H} = \hat{H}_\psi + \hat{H}_{\psi\sigma} + \hat{H}_\sigma \quad (\text{B.1})$$

where

$$\hat{H}_\psi = \sum_{pq} \int d^3x \bar{\psi}_p(x) \left(\alpha^i \partial_i - \beta M \right) \psi_{q,\tau}(x) \hat{\eta}_{p\tau}^\dagger \hat{\eta}_q \quad (\text{B.2})$$

$$\hat{H}_{\psi\sigma} = \sum_{pq} \int d^3x \bar{\psi}_p(x) \left(-\beta g_\sigma \hat{\sigma}(x, t) \right) \psi_q(x) \hat{\eta}_{p\tau}^\dagger \hat{\eta}_q \quad (\text{B.3})$$

$$\hat{H}_\sigma = \int d^3x \left[\frac{1}{2} \hat{\pi}_\sigma^2(x, t) + \frac{1}{2} (\partial_i \hat{\sigma}(x))^2 + \frac{1}{2} m^2 \hat{\sigma}^2(x, t) \right] \quad (\text{B.4})$$

It is assumed the operators act on their respective sectors. The scalar field operator $\hat{\sigma}(x, t)$ operates at different times on the boson sector of the Fock space $\mathcal{F} = \mathcal{F}_f \otimes \mathcal{F}_b$. The time evolution operator on \mathcal{F} has the form

$$\hat{U}(t_0, t_f) = \hat{\mathcal{T}} \exp \left(-i \int_{t_0}^{t_f} \hat{H}(t') dt' \right) \quad (\text{B.5})$$

where $\hat{\mathcal{T}}$ is the time-ordering operator. The amplitude for an initial state $|\Psi\rangle_0 \otimes |\sigma\rangle_0$ at time t_0 to evolve to a state $|\Psi\rangle_f \otimes |\sigma\rangle_f$ at time t_f , $t_f > t_0$ is,

$$\left(\langle\Psi|_f \otimes \langle\sigma|_f\right) \hat{\mathcal{T}} \exp\left(-i \int_{t_0}^{t_f} \hat{H}(t') dt'\right) \left(|\Psi\rangle_0 \otimes |\sigma\rangle_0\right) \quad (\text{B.6})$$

To obtain the sum over histories representation, we adapt the construction given in [254] for a scalar field theory. First, we divide the time interval into $N + 1$ partitions.

$$\hat{\mathcal{T}} \exp\left(-i \int_{t_0}^{t_f} \hat{H}(t') dt'\right) \approx e^{-i\hat{H}(t_f-t_{N+1})} e^{-i\hat{H}(t_{N+1}-t_N)} \dots e^{-i\hat{H}(t_1-t_0)} \quad (\text{B.7})$$

where we assume N is large enough so that $t_{k+1} - t_k$ is small. The product is time ordered so that $t_{k+1} > t_k$ for all $k < N + 1$. The discretized amplitude is then,

$$\left(\langle\Psi|_f \otimes \langle\sigma|_f\right) e^{-i\hat{H}(t_f-t_{N+1})} e^{-i\hat{H}(t_{N+1}-t_N)} \dots e^{-i\hat{H}(t_1-t_0)} \left(|\Psi\rangle_0 \otimes |\sigma\rangle_0\right) \quad (\text{B.8})$$

In between each interval, we insert a resolution of the \mathcal{F} identity operator, So we insert the following form of the identity operator at every time-step

$$\hat{I}_f \otimes \hat{I}_b = \hat{I}_f \otimes \int D\sigma_k |\sigma_k\rangle \langle\sigma_k| \quad (\text{B.9})$$

where the definition of the measure $D\sigma_k$ is given in [254]. We keep the identity for the fermion sector fixed at the identity since the fermion operators do not depend on time and satisfy time-independent anti-commutation relations

$$\{\hat{\eta}_p^\dagger, \hat{\eta}_q\} = \delta_{pq}, \quad \{\hat{\eta}_p, \hat{\eta}_q\} = \{\hat{\eta}_p^\dagger, \hat{\eta}_q^\dagger\} = 0 \quad (\text{B.10})$$

The σ field on the other hand obey equal time commutation relations for a fixed time t_k .

$$[\hat{\pi}_\sigma(x, t_k), \hat{\sigma}(y, t_k)] = i\delta^3(x - y), \quad [\hat{\sigma}(x, t_k), \hat{\sigma}(y, t_k)] = [\hat{\pi}_\sigma(x, t_k), \hat{\pi}_\sigma(y, t_k)] = 0 \quad (\text{B.11})$$

Inserting Eq. (B.9) at every timestep we arrive at

$$\begin{aligned} & \left(\langle \Psi |_f \otimes \langle \sigma |_f \right) \hat{\mathcal{T}} \exp \left(-i \int_{t_0}^{t_f} \hat{H}(t') dt' \right) \left(|\Psi \rangle_0 \otimes |\sigma \rangle_0 \right) \\ &= \left(\langle \Psi |_f \otimes \langle \sigma |_f \right) e^{-i\hat{H}(t_f - t_{N+1})} \left(\hat{I}_f \otimes \int D\sigma_{N+1} |\sigma_{N+1} \rangle \langle \sigma_{N+1}| \right) e^{-i\hat{H}(t_{N+1} - t_N)} \\ & \times \left(\hat{I}_f \otimes \int D\sigma_N |\sigma_N \rangle \langle \sigma_N| \right) \dots \left(\hat{I}_f \otimes \int D\sigma_1 |\sigma_1 \rangle \langle \sigma_1| \right) e^{-i\hat{H}(t_1 - t_0)} \left(|\Psi \rangle_0 \otimes |\sigma \rangle_0 \right). \end{aligned} \quad (\text{B.12})$$

Since the tensor product is bilinear, we can factor out the integrals from each tensor,

$$\begin{aligned} & \left(\langle \Psi |_f \otimes \langle \sigma |_f \right) \hat{\mathcal{T}} \exp \left(-i \int_{t_0}^{t_f} \hat{H}(t') dt' \right) \left(|\Psi \rangle_0 \otimes |\sigma \rangle_0 \right) \\ &= \int \prod_{k=1}^{N+1} D\sigma_k \left(\langle \Psi |_f \otimes \langle \sigma |_f \right) e^{-i\hat{H}(t_f - t_{N+1})} \left(\hat{I}_f \otimes |\sigma_{N+1} \rangle \langle \sigma_{N+1}| \right) \\ & \times \dots \left(\hat{I}_f \otimes |\sigma_1 \rangle \langle \sigma_1| \right) e^{-i\hat{H}(t_1 - t_0)} \left(|\Psi \rangle_0 \otimes |\sigma \rangle_0 \right) \end{aligned} \quad (\text{B.13})$$

To evaluate this, we look at the k th insertion,

$$\dots \left(\hat{I}_f \otimes |\sigma_{k+1} \rangle \langle \sigma_{k+1}| \right) e^{-i\hat{H}(t_{k+1} - t_k)} \left(\hat{I}_f \otimes |\sigma_k \rangle \langle \sigma_k| \right) \dots \quad (\text{B.14})$$

If we assume $t_{k+1} - t_k$ is small for all k , then

$$e^{-i\hat{H}(t_{k+1}-t_k)} \sim I_f \otimes I_b - i\hat{H}(t_{k+1} - t_k) + \mathcal{O}\left((t_{k+1} - t_k)^2\right) \quad (\text{B.15})$$

Then,

$$\begin{aligned} & \left(\hat{I}_f \otimes |\sigma_{k+1}\rangle\langle\sigma_{k+1}| \right) e^{-i\hat{H}(t_{k+1}-t_k)} \left(\hat{I}_f \otimes |\sigma_k\rangle\langle\sigma_k| \right) \\ &= \left(\hat{I}_f \otimes |\sigma_{k+1}\rangle\langle\sigma_{k+1}| \right) I_f \otimes I_b \left(\hat{I}_f \otimes |\sigma_k\rangle\langle\sigma_k| \right) \\ & \quad - i(t_{k+1} - t_k) \left(\hat{I}_f \otimes |\sigma_{k+1}\rangle\langle\sigma_{k+1}| \right) \hat{H} \left(\hat{I}_f \otimes |\sigma_k\rangle\langle\sigma_k| \right) \end{aligned} \quad (\text{B.16})$$

We evaluate the first term of Eq. (B.16),

$$\begin{aligned} & \left(\hat{I}_f \otimes |\sigma_{k+1}\rangle\langle\sigma_{k+1}| \right) I_f \otimes I_b \left(\hat{I}_f \otimes |\sigma_k\rangle\langle\sigma_k| \right) \\ &= \hat{I}_f \otimes |\sigma_{k+1}\rangle\langle\sigma_{k+1}| \sigma_k \langle\sigma_k| = \hat{I}_f \otimes |\sigma_{k+1}\rangle\langle\sigma_k| \delta[\sigma_{k+1} - \sigma_k] \end{aligned} \quad (\text{B.17})$$

where

$$\delta[\sigma_{k+1} - \sigma_k] = \prod_{\vec{x}} \delta\left(\sigma_{k+1}(x) - \sigma_k(x)\right) \quad (\text{B.18})$$

We can write the delta function in the Fourier representation,

$$\prod_{\vec{x}} \delta\left(\sigma_{k+1}(x) - \sigma_k(x)\right) = \prod_{\vec{x}} \int_{-\infty}^{\infty} \frac{d\pi_k}{2\pi} e^{i\pi_k(x)(\sigma_{k+1}(x) - \sigma_k(x))} \quad (\text{B.19})$$

To evaluating the second term in Eq. (B.16), we note the Hamiltonian has the form,

$$\hat{H} = \hat{H}_\psi \otimes I_b + \int d^3x \sum_{pq} \bar{\psi}_p(x) \beta \left(I_f \otimes \hat{\sigma}(x, t) \right) \psi_q(x) \left(\hat{\eta}_p^\dagger \otimes I_b \right) \left(\hat{\eta}_q \otimes I_b \right) + I_f \otimes \hat{H}_\sigma \quad (\text{B.20})$$

The second term in Eq. (B.16) is then,

$$\begin{aligned} & \left(\hat{I}_f \otimes |\sigma_{k+1}\rangle\langle\sigma_{k+1}| \right) \left[\hat{H}_\psi \otimes I_b \right. \\ & \left. + \int d^3x \sum_{pq} \bar{\psi}_p(x) \beta \left(I_f \otimes \hat{\sigma}(x, t) \right) \psi_q(x) \left(\hat{\eta}_p^\dagger \otimes I_b \right) \left(\hat{\eta}_q \otimes I_b \right) + I_f \otimes \hat{H}_\sigma \right] \left(\hat{I}_f \otimes |\sigma_k\rangle\langle\sigma_k| \right) \end{aligned} \quad (\text{B.21})$$

We evaluate each term in Eq. (B.21). First,

$$\left(\hat{I}_f \otimes |\sigma_{k+1}\rangle\langle\sigma_{k+1}| \right) \left(\hat{H}_\psi \otimes I_b \right) \left(\hat{I}_f \otimes |\sigma_k\rangle\langle\sigma_k| \right) = \hat{H}_\psi \otimes |\sigma_{k+1}\rangle\langle\sigma_k| \delta[\sigma_{k+1} - \sigma_k] \quad (\text{B.22})$$

The next term,

$$\begin{aligned} & \left(\hat{I}_f \otimes |\sigma_{k+1}\rangle\langle\sigma_{k+1}| \right) \int d^3x \sum_{pq} \bar{\psi}_p(x) \left(I_f \otimes \hat{\sigma}(x, t) \right) \psi_q(x) \left(\hat{\eta}_p^\dagger \otimes I_b \right) \left(\hat{\eta}_q \otimes I_b \right) \left(\hat{I}_f \otimes |\sigma_k\rangle\langle\sigma_k| \right) \\ & = \int d^3x \left(\sum_{pq} \bar{\psi}_p(x) \beta \psi_q(x) \hat{\eta}_p^\dagger \hat{\eta}_q \right) \otimes \left(\sigma(x, t_k) \delta[\sigma_{k+1} - \sigma_k] |\sigma_{k+1}\rangle\langle\sigma_k| \right). \end{aligned} \quad (\text{B.23})$$

Last equality is the form used to quantize the free scalar field Hamiltonian from Ref. [254].

The result is,

$$\begin{aligned} & \left(\hat{I}_f \otimes |\sigma_{k+1}\rangle\langle\sigma_{k+1}| \right) \hat{H}_\sigma \left(\hat{I}_f \otimes |\sigma_k\rangle\langle\sigma_k| \right) = \hat{I}_f \otimes |\sigma_{k+1}\rangle\langle\sigma_{k+1}| \hat{H}_\sigma |\sigma_k\rangle\langle\sigma_k| \\ & = \hat{I}_f \otimes \int D\pi_{\sigma,k} H[\pi_{\sigma,k}, \sigma_k] \exp \left(i \int d^3x \pi_{\sigma,k}(x) (\sigma_{k+1}(x) - \sigma_k(x)) \right) |\sigma_{k+1}\rangle\langle\sigma_k| \end{aligned} \quad (\text{B.24})$$

Using these results, the k -th slice becomes

$$\begin{aligned} & \hat{I}_f \otimes |\sigma_{k+1}\rangle\langle\sigma_k| - i(t_{k+1} - t_k) \left[\hat{H}_\psi \otimes |\sigma_{k+1}\rangle\langle\sigma_k| \int D\pi_{\sigma,k} \exp \left(i \int d^3x \pi_{\sigma,k}(x) (\sigma_{k+1}(x) - \sigma_k(x)) \right) \right. \\ & + \int d^3x \left(\sum_{pq} \bar{\psi}_p(x) \beta \psi_q(x) \hat{\eta}_p^\dagger \hat{\eta}_q \right) \otimes \left(\sigma(x, t_k) |\sigma_{k+1}\rangle\langle\sigma_k| \right) \left. \int D\pi_{\sigma,k} \exp \left(i \int d^3x \pi_{\sigma,k}(x) (\sigma_{k+1}(x) - \sigma_k(x)) \right) \right) \\ & + \hat{I}_f \otimes \int D\pi_{\sigma,k} H[\pi_{\sigma,k}, \sigma_k] \exp \left(i \int d^3x \pi_{\sigma,k}(x) (\sigma_{k+1}(x) - \sigma_k(x)) \right) |\sigma_{k+1}\rangle\langle\sigma_k| \end{aligned} \quad (\text{B.25})$$

where we used the Fourier representation of the functional delta functions. If we factor out

$$I_f \otimes |\sigma_{k+1}\rangle\langle\sigma_k|,$$

$$\begin{aligned} & (I_f \otimes |\sigma_{k+1}\rangle\langle\sigma_k|) \int D\pi_{\sigma,k} \left[I_f \otimes I_b - i(t_{k+1} - t_k) \left(H_\psi \otimes I_b \right. \right. \\ & + \left. \left. \int d^3x \sum_{pq} \bar{\psi}_p \beta (I_f \otimes \sigma(x, t_k)) \psi_q(x) (\hat{\eta}_p^\dagger \otimes I_b) (\hat{\eta}_q \otimes I_b) + I_f \otimes H[\pi_{\sigma,k}, \sigma_k] \right) \right] \\ & \times \exp \left(i \int d^3x \pi_{\sigma,k}(x) (\sigma_{k+1}(x) - \sigma_k(x)) \right) \\ & = (I_f \otimes |\sigma_{k+1}\rangle\langle\sigma_k|) \int D\pi_{\sigma,k} \left[I_f \otimes I_b - i(t_{k+1} - t_k) H[\pi_{\sigma,k}, \sigma, \hat{\eta}_p^\dagger, \hat{\eta}_q] \right] \\ & \times \exp \left(i \int d^3x \pi_{\sigma,k}(x) (\sigma_{k+1}(x) - \sigma_k(x)) \right) \end{aligned} \quad (\text{B.26})$$

Since $t_{k+1} - t_k$ is small, we replace $I - i(t_{k+1} - t_k)H$ by $e^{-i(t_{k+1} - t_k)H}$,

$$\begin{aligned}
&= \int D\pi_{\sigma,k} \exp \left(i \int d^3x \pi_{\sigma,k}(x) (\sigma_{k+1}(x) - \sigma_k(x)) - i(t_{k+1} - t_k)H[\pi_{\sigma,k}, \sigma_k, \hat{\eta}_p^\dagger, \hat{\eta}_q] \right) \\
&\times \hat{I}_f \otimes |\sigma_{k+1}\rangle \langle \sigma_k| \tag{B.27}
\end{aligned}$$

Considering every insertion, we have

$$\begin{aligned}
&\left(\langle \Psi |_f \otimes \langle \sigma |_f \right) \hat{\mathcal{T}} \exp \left(-i \int_{t_0}^{t_f} \hat{H}(t') dt' \right) \left(|\Psi\rangle_0 \otimes |\sigma\rangle_0 \right) = \\
&\lim_{N \rightarrow \infty} \int \prod_{k=1}^N D\sigma_k \prod_{j=0}^N D\pi_{\sigma,j} \langle \Psi_f | \hat{\mathcal{T}} \exp \left(i \Delta t \sum_{j=0}^N \int d^3x \pi(x, t_j) \frac{(\sigma_{j+1} - \sigma_j)}{\Delta t} - H[\pi_j, \sigma_j, \hat{\eta}_p^\dagger, \hat{\eta}_q] \right) |\Psi_0\rangle \\
&= \int D\sigma D\pi \langle \Psi_f | \hat{\mathcal{T}} \exp \left(i \int_{t_0}^{t_f} dt \int d^3x [\pi(x, t) \dot{\sigma}(x, t) - H[\pi_\sigma, \sigma, \hat{\eta}_p^\dagger, \hat{\eta}_q]] \right) |\Psi_0\rangle \tag{B.28}
\end{aligned}$$

We can do the integral over momentum π_σ ,

$$\begin{aligned}
&\left(\langle \Psi |_f \otimes \langle \sigma |_f \right) \hat{\mathcal{T}} \exp \left(-i \int_{t_0}^{t_f} \hat{H}(t') dt' \right) \left(|\Psi\rangle_0 \otimes |\sigma\rangle_0 \right) \\
&= \int D\sigma \langle \Psi_f | \hat{\mathcal{T}} \exp \left(i \int d^4x \mathcal{L}[\sigma, \hat{\eta}_p^\dagger, \hat{\eta}_q] \right) |\Psi_0\rangle \tag{B.29}
\end{aligned}$$

where the Lagrangian \mathcal{L} is

$$\mathcal{L} = - \sum_{pq} \bar{\psi}_p(x) \left(\alpha^i \partial_i - \beta M - \beta g_\sigma \sigma(x, t) \right) \psi_q(x) \hat{\eta}_p^\dagger \hat{\eta}_q + \left[\frac{1}{2} \partial_\mu \sigma \partial_\mu \sigma + \frac{1}{2} m^2 \sigma^2 \right] \tag{B.30}$$

This completes the derivation.

Bibliography

- [1] E. Fermi et al. “Azione di sostanze idrogenate sulla radioattivit a provocata da neutroni. I.” In: *Ric. Scientifica* 5 (1934), pp. 282–283.
- [2] O. Hahn and F. Strassmann. “ ber den Nachweis und das Verhalten der bei der Bestrahlung des Urans mittels Neutronen entstehenden Erdalkalimetalle”. In: *Naturwissenschaften* 27.11 (1939).
- [3] L. Meitner and O. R. Frisch. “Disintegration of Uranium by Neutrons: a New Type of Nuclear Reaction”. In: *Nature* 143.3615 (Feb. 1939), pp. 239–240. DOI: 10.1038/143239a0.
- [4] L. Meitner and O. R. Frisch. “Products of the Fission of the Uranium Nucleus”. In: *Nature* 143.3620 (Mar. 1939), pp. 471–472. DOI: 10.1038/143471a0.
- [5] N. Bohr and J. A. Wheeler. “The Mechanism of Nuclear Fission”. In: *Phys. Rev.* 56 (5 Sept. 1939), pp. 426–450. DOI: 10.1103/PhysRev.56.426.
- [6] P. Armbruster. “On the quest of production of superheavy nuclei in reactions of ^{48}Ca with the heaviest actinide targets”. In: *The European Physical Journal A - Hadrons and Nuclei* 7.1 (Jan. 2000), pp. 23–33. DOI: 10.1007/s100500050006.
- [7] Y. T. Oganessian and V. K. Utyonkov. “Super-heavy element research”. In: *Reports on Progress in Physics* 78.3 (Mar. 2015), p. 036301. DOI: 10.1088/0034-4885/78/3/036301.
- [8] K.-H. Schmidt and B. Jurado. “Review on the progress in nuclear fission—experimental methods and theoretical descriptions”. In: *Reports on Progress in Physics* 81.10 (Sept. 2018), p. 106301. DOI: 10.1088/1361-6633/aacfa7.
- [9] O. R. Smits et al. “The quest for superheavy elements and the limit of the periodic table”. In: *Nature Reviews Physics* 6.2 (Feb. 2024), pp. 86–98. DOI: 10.1038/s42254-023-00668-y.
- [10] J. J. Cowan et al. “Origin of the heaviest elements: The rapid neutron-capture process”. In: *Rev. Mod. Phys.* 93 (1 Feb. 2021), p. 015002. DOI: 10.1103/RevModPhys.93.015002.
- [11] C. Iliadis. *Nuclear physics of stars*. John Wiley & Sons, 2015.
- [12] F. K appeler et al. “The s process: Nuclear physics, stellar models, and observations”. In: *Rev. Mod. Phys.* 83 (1 Apr. 2011), pp. 157–193. DOI: 10.1103/RevModPhys.83.157.

- [13] F.-K. Thielemann et al. “Neutron Star Mergers and Nucleosynthesis of Heavy Elements”. In: *Annual Review of Nuclear and Particle Science* 67. Volume 67, 2017 (2017), pp. 253–274. DOI: <https://doi.org/10.1146/annurev-nucl-101916-123246>.
- [14] R. Fernández et al. “Dynamics, nucleosynthesis, and kilonova signature of black hole—neutron star merger ejecta”. In: *Classical and Quantum Gravity* 34.15 (July 2017), p. 154001. DOI: [10.1088/1361-6382/aa7a77](https://doi.org/10.1088/1361-6382/aa7a77).
- [15] S. Wanajo et al. “Actinide-Boosting r Process in Black-Hole–Neutron-Star Merger Ejecta”. In: *Phys. Rev. Lett.* 133 (24 Dec. 2024), p. 241201. DOI: [10.1103/PhysRevLett.133.241201](https://doi.org/10.1103/PhysRevLett.133.241201).
- [16] M. Reichert et al. “Nucleosynthesis in magneto-rotational supernovae”. In: *Monthly Notices of the Royal Astronomical Society* 501.4 (Jan. 2021), pp. 5733–5745. DOI: [10.1093/mnras/stab029](https://doi.org/10.1093/mnras/stab029).
- [17] P. Möller et al. “Nuclear ground-state masses and deformations: FRDM(2012)”. In: *Atomic Data and Nuclear Data Tables* 109-110 (2016), pp. 1–204. DOI: <https://doi.org/10.1016/j.adt.2015.10.002>.
- [18] E. McCutchan et al. *National Nuclear Data Center Nuclear Wallet Cards*. 2023. URL: <https://www.nndc.bnl.gov/walletcards/>.
- [19] C. J. e. a. Horowitz. “ r -process nucleosynthesis: connecting rare-isotope beam facilities with the cosmos”. In: *Journal of Physics G: Nuclear and Particle Physics* 46.8 (July 2019), p. 083001. DOI: [10.1088/1361-6471/ab0849](https://doi.org/10.1088/1361-6471/ab0849).
- [20] S. Rosswog and O. Korobkin. “Heavy Elements and Electromagnetic Transients from Neutron Star Mergers”. In: *Annalen der Physik* 536.2 (2024), p. 2200306. DOI: <https://doi.org/10.1002/andp.202200306>.
- [21] S. Rosswog et al. “Fast dynamic ejecta in neutron star mergers”. In: *Monthly Notices of the Royal Astronomical Society* 538.2 (Feb. 2025), pp. 907–924. DOI: [10.1093/mnras/staf324](https://doi.org/10.1093/mnras/staf324).
- [22] C. Winteler. “Light element production in the big bang and the synthesis of heavy elements in 3D MHD jets from core-collapse supernovae”. PhD thesis. University of Basel, 2013.
- [23] I. Panov and F.-K. Thielemann. “Final r -process yields and the influence of fission: The competition between neutron-induced and β -delayed fission”. In: *Nuclear Physics A* 718 (2003), pp. 647–649. DOI: [https://doi.org/10.1016/S0375-9474\(03\)00875-3](https://doi.org/10.1016/S0375-9474(03)00875-3).

- [24] M. R. Mumpower, G. McLaughlin, and R. Surman. “Formation of the rare-earth peak: Gaining insight into late-time r-process dynamics”. In: *Physical Review C—Nuclear Physics* 85.4 (2012), p. 045801.
- [25] H. M. Devaraja et al. “New studies and a short review of heavy neutron-rich transfer products”. In: *The European Physical Journal A* 56.9 (Sept. 2020), p. 224. DOI: 10.1140/epja/s10050-020-00229-2.
- [26] J.-F. Lemaître et al. “Fission fragment distributions and their impact on the r-process nucleosynthesis in neutron star mergers”. In: *Phys. Rev. C* 103 (2 Feb. 2021), p. 025806. DOI: 10.1103/PhysRevC.103.025806.
- [27] S. A. Giuliani, G. Martínez-Pinedo, and L. M. Robledo. “Fission properties of super-heavy nuclei for r-process calculations”. In: *Phys. Rev. C* 97 (3 Mar. 2018), p. 034323. DOI: 10.1103/PhysRevC.97.034323.
- [28] P. Giuliani et al. “Model orthogonalization and Bayesian forecast mixing via principal component analysis”. In: *Phys. Rev. Res.* 6 (3 Sept. 2024), p. 033266. DOI: 10.1103/PhysRevResearch.6.033266.
- [29] S. Goriely. “The fundamental role of fission during r-process nucleosynthesis in neutron star mergers”. In: *Eur. Phys. J. A* 51.2 (Feb. 2015), p. 22. DOI: 10.1140/epja/i2015-15022-3.
- [30] Y. Zhu et al. “Californium-254 and kilonova light curves”. In: *The Astrophysical Journal Letters* 863.2 (2018), p. L23. DOI: 10.3847/2041-8213/aad5de.
- [31] T. Sprouse, E. Holmbeck, et al. “Using excitation-energy dependent fission yields to identify key fissioning nuclei in r-process nucleosynthesis”. In: *Journal of Physics G: Nuclear and Particle Physics* 46.6 (2019), p. 065202. DOI: 10.1088/1361-6471/ab0bea.
- [32] Y. Zhu et al. “Modeling kilonova light curves: dependence on nuclear inputs”. In: *The Astrophysical Journal* 906.2 (2021), p. 94.
- [33] M. Bender et al. “Future of nuclear fission theory”. In: *Journal of Physics G: Nuclear and Particle Physics* 47.11 (Oct. 2020), p. 113002. DOI: 10.1088/1361-6471/abab4f.
- [34] P. Ring and P. Schuck. *The nuclear many-body problem*. Springer Science & Business Media, 2004.
- [35] B. R. Barrett, P. Navrátil, and J. P. Vary. “Ab initio no core shell model”. In: *Progress in Particle and Nuclear Physics* 69 (2013), pp. 131–181. DOI: <https://doi.org/10.1016/j.pnpnp.2012.10.003>.

- [36] W. Kohn and L. J. Sham. “Self-Consistent Equations Including Exchange and Correlation Effects”. In: *Phys. Rev.* 140 (4A Nov. 1965), A1133–A1138. DOI: 10.1103/PhysRev.140.A1133.
- [37] R. M. Martin. *Electronic structure: basic theory and practical methods*. Cambridge university press, 2020.
- [38] C. A. Ullrich. “Time-dependent density-functional theory: concepts and applications”. In: (2011).
- [39] K. L. Heyde and K. L. Heyde. *The nuclear shell model*. Springer, 1994.
- [40] G. Hagen et al. “Coupled-cluster theory for three-body Hamiltonians”. In: *Phys. Rev. C* 76 (3 Sept. 2007), p. 034302. DOI: 10.1103/PhysRevC.76.034302.
- [41] R. Roth et al. “Medium-Mass Nuclei with Normal-Ordered Chiral $NN+3N$ Interactions”. In: *Phys. Rev. Lett.* 109 (5 July 2012), p. 052501. DOI: 10.1103/PhysRevLett.109.052501.
- [42] E. Gebrerufael, A. Calci, and R. Roth. “Open-shell nuclei and excited states from multireference normal-ordered Hamiltonians”. In: *Phys. Rev. C* 93 (3 Mar. 2016), p. 031301. DOI: 10.1103/PhysRevC.93.031301.
- [43] K. Goeke and P.-G. Reinhard. “The generator-coordinate-method with conjugate parameters and the unification of microscopic theories for large amplitude collective motion”. In: *Annals of Physics* 124.2 (1980), pp. 249–289. DOI: [https://doi.org/10.1016/0003-4916\(80\)90210-9](https://doi.org/10.1016/0003-4916(80)90210-9).
- [44] F. Dönau, J.-y. Zhang, and L. Riedinger. “On the solution to the large amplitude collective motion of finite interacting Fermi systems”. In: *Nuclear Physics A* 496.2 (1989), pp. 333–345. DOI: [https://doi.org/10.1016/0375-9474\(89\)90178-4](https://doi.org/10.1016/0375-9474(89)90178-4).
- [45] B. Bally. “Description of odd-mass nuclei by multi-reference energy density functional methods”. Theses. Université de Bordeaux, June 2014. URL: <https://theses.hal.science/tel-01023059>.
- [46] P. Marević, D. Regnier, and D. Lacroix. “Multiconfigurational time-dependent density functional theory for atomic nuclei: technical and numerical aspects”. In: *The European Physical Journal A* 60.1 (Jan. 2024), p. 10. DOI: 10.1140/epja/s10050-024-01231-8.
- [47] D. J. Dean and M. Hjorth-Jensen. “Coupled-cluster approach to nuclear physics”. In: *Phys. Rev. C* 69 (5 May 2004), p. 054320. DOI: 10.1103/PhysRevC.69.054320.

- [48] G. Hagen et al. “Ab initio coupled-cluster approach to nuclear structure with modern nucleon-nucleon interactions”. In: *Phys. Rev. C* 82 (3 Sept. 2010), p. 034330. DOI: 10.1103/PhysRevC.82.034330.
- [49] G. Hagen et al. “Coupled-cluster computations of atomic nuclei”. In: *Reports on Progress in Physics* 77.9 (Sept. 2014), p. 096302. DOI: 10.1088/0034-4885/77/9/096302.
- [50] P. Piecuch and K. Kowalski. “The State-Universal Multi-Reference Coupled-Cluster Theory: An Overview of Some Recent Advances”. In: *International Journal of Molecular Sciences* 3.6 (2002), pp. 676–709. DOI: 10.3390/i3060676.
- [51] H. Hergert et al. “The In-Medium Similarity Renormalization Group: A novel ab initio method for nuclei”. In: *Physics Reports* 621 (2016). Memorial Volume in Honor of Gerald E. Brown, pp. 165–222. DOI: <https://doi.org/10.1016/j.physrep.2015.12.007>.
- [52] H. Hergert et al. “In-Medium Similarity Renormalization Group Approach to the Nuclear Many-Body Problem”. In: *An Advanced Course in Computational Nuclear Physics: Bridging the Scales from Quarks to Neutron Stars*. Ed. by M. Hjorth-Jensen, M. P. Lombardo, and U. van Kolck. Cham: Springer International Publishing, 2017, pp. 477–570. DOI: 10.1007/978-3-319-53336-0_10.
- [53] H. Hergert. “In-medium similarity renormalization group for closed and open-shell nuclei”. In: *Physica Scripta* 92.2 (Dec. 2016), p. 023002. DOI: 10.1088/1402-4896/92/2/023002.
- [54] K. Sekizawa. “Multinucleon Transfer Reactions and Quasifission Processes in Time-Dependent Hartree-Fock Theory”. PhD thesis.
- [55] C. Simenel and A. Umar. “Heavy-ion collisions and fission dynamics with the time-dependent Hartree-Fock theory and its extensions”. In: *Progress in Particle and Nuclear Physics* 103 (2018), pp. 19–66. DOI: <https://doi.org/10.1016/j.ppnp.2018.07.002>.
- [56] R. A. Broglia and V. Zelevinsky. *Fifty years of nuclear BCS: pairing in finite systems*. World Scientific, 2013.
- [57] M. Levy. “Universal variational functionals of electron densities, first-order density matrices, and natural spin-orbitals and solution of the v-representability problem”. In: *Proceedings of the National Academy of Sciences* 76.12 (1979), pp. 6062–6065. DOI: 10.1073/pnas.76.12.6062.
- [58] M. Levy. “Electron densities in search of Hamiltonians”. In: *Phys. Rev. A* 26 (3 Sept. 1982), pp. 1200–1208. DOI: 10.1103/PhysRevA.26.1200.

- [59] E. H. Lieb. “Density functionals for coulomb systems”. In: *International Journal of Quantum Chemistry* 24.3 (1983), pp. 243–277. DOI: <https://doi.org/10.1002/qua.560240302>.
- [60] R. M. Dreizler and J. da Providência. *Density functional methods in physics*. Vol. 123. Springer Science & Business Media, 2013.
- [61] P. Hohenberg and W. Kohn. “Inhomogeneous Electron Gas”. In: *Phys. Rev.* 136 (3B Nov. 1964), B864–B871. DOI: [10.1103/PhysRev.136.B864](https://doi.org/10.1103/PhysRev.136.B864).
- [62] W. Kohn. “ v -Representability and Density Functional Theory”. In: *Phys. Rev. Lett.* 51 (17 Oct. 1983), pp. 1596–1598. DOI: [10.1103/PhysRevLett.51.1596](https://doi.org/10.1103/PhysRevLett.51.1596).
- [63] J. Engel. “Intrinsic-density functionals”. In: *Phys. Rev. C* 75 (1 Jan. 2007), p. 014306. DOI: [10.1103/PhysRevC.75.014306](https://doi.org/10.1103/PhysRevC.75.014306).
- [64] B. G. Giraud, B. K. Jennings, and B. R. Barrett. “Existence of a density functional for an intrinsic state”. In: *Phys. Rev. A* 78 (3 Sept. 2008), p. 032507. DOI: [10.1103/PhysRevA.78.032507](https://doi.org/10.1103/PhysRevA.78.032507).
- [65] B. G. Giraud. “Density functionals in the laboratory frame”. In: *Phys. Rev. C* 77 (1 Jan. 2008), p. 014311. DOI: [10.1103/PhysRevC.77.014311](https://doi.org/10.1103/PhysRevC.77.014311).
- [66] J. Dobaczewski, H. Flocard, and J. Treiner. “Hartree-Fock-Bogolyubov description of nuclei near the neutron-drip line”. In: *Nuclear Physics A* 422.1 (1984), pp. 103–139. DOI: [https://doi.org/10.1016/0375-9474\(84\)90433-0](https://doi.org/10.1016/0375-9474(84)90433-0).
- [67] J. Dobaczewski et al. “Mean-field description of ground-state properties of drip-line nuclei: Pairing and continuum effects”. In: *Phys. Rev. C* 53 (6 June 1996), pp. 2809–2840. DOI: [10.1103/PhysRevC.53.2809](https://doi.org/10.1103/PhysRevC.53.2809).
- [68] J. C. Pei, A. T. Kruppa, and W. Nazarewicz. “Quasiparticle continuum and resonances in the Hartree-Fock-Bogoliubov theory”. In: *Phys. Rev. C* 84 (2 Aug. 2011), p. 024311. DOI: [10.1103/PhysRevC.84.024311](https://doi.org/10.1103/PhysRevC.84.024311).
- [69] M. V. Stoitsov et al. “Quadrupole deformations of neutron-drip-line nuclei studied within the Skyrme Hartree-Fock-Bogoliubov approach”. In: *Phys. Rev. C* 61 (3 Feb. 2000), p. 034311. DOI: [10.1103/PhysRevC.61.034311](https://doi.org/10.1103/PhysRevC.61.034311).
- [70] M. V. Stoitsov et al. “Systematic study of deformed nuclei at the drip lines and beyond”. In: *Phys. Rev. C* 68 (5 Nov. 2003), p. 054312. DOI: [10.1103/PhysRevC.68.054312](https://doi.org/10.1103/PhysRevC.68.054312).

- [71] N. Michel, K. Matsuyanagi, and M. Stoitsov. “Gamow-Hartree-Fock-Bogoliubov method: Representation of quasiparticles with Berggren sets of wave functions”. In: *Phys. Rev. C* 78 (4 Oct. 2008), p. 044319. DOI: 10.1103/PhysRevC.78.044319.
- [72] P.-G. Reinhard. “The relativistic mean-field description of nuclei and nuclear dynamics”. In: *Reports on Progress in Physics* 52.4 (Apr. 1989), p. 439. DOI: 10.1088/0034-4885/52/4/002.
- [73] P. Ring. “Relativistic mean field theory in finite nuclei”. In: *Progress in Particle and Nuclear Physics* 37 (1996), pp. 193–263. DOI: [https://doi.org/10.1016/0146-6410\(96\)00054-3](https://doi.org/10.1016/0146-6410(96)00054-3).
- [74] J. Dobaczewski. “Ab initio derivation of model energy density functionals”. In: *Journal of Physics G: Nuclear and Particle Physics* 43.4 (Feb. 2016), 04LT01. DOI: 10.1088/0954-3899/43/4/04LT01.
- [75] R. J. Furnstahl. “Turning the nuclear energy density functional method into a proper effective field theory: reflections”. In: *The European Physical Journal A* 56.3 (Mar. 2020), p. 85. DOI: 10.1140/epja/s10050-020-00095-y.
- [76] F. Marino et al. “Nuclear energy density functionals grounded in ab initio calculations”. In: *Phys. Rev. C* 104 (2 Aug. 2021), p. 024315. DOI: 10.1103/PhysRevC.104.024315.
- [77] L. Zurek et al. “Optimized nuclear energy density functionals including long-range pion contributions”. In: *Phys. Rev. C* 109 (1 Jan. 2024), p. 014319. DOI: 10.1103/PhysRevC.109.014319.
- [78] P. Sharma and R. J. Furnstahl. *Testing Variational Perturbation Theory for Effective Actions Using the Gaudin-Yang Model*. 2025. URL: <https://arxiv.org/abs/2506.02919>.
- [79] D. Vautherin and D. M. Brink. “Hartree-Fock Calculations with Skyrme’s Interaction. I. Spherical Nuclei”. In: *Phys. Rev. C* 5 (3 Mar. 1972), pp. 626–647. DOI: 10.1103/PhysRevC.5.626.
- [80] E. Chabanat et al. “A Skyrme parametrization from subnuclear to neutron star densities”. In: *Nuclear Physics A* 627.4 (1997), pp. 710–746. DOI: [https://doi.org/10.1016/S0375-9474\(97\)00596-4](https://doi.org/10.1016/S0375-9474(97)00596-4).
- [81] E. Chabanat et al. “A Skyrme parametrization from subnuclear to neutron star densities Part II. Nuclei far from stabilities”. In: *Nuclear Physics A* 635.1 (1998), pp. 231–256. DOI: [https://doi.org/10.1016/S0375-9474\(98\)00180-8](https://doi.org/10.1016/S0375-9474(98)00180-8).

- [82] M. Kortelainen et al. “Nuclear energy density optimization”. In: *Phys. Rev. C* 82 (2 Aug. 2010), p. 024313. DOI: 10.1103/PhysRevC.82.024313.
- [83] J. Bartel et al. “Towards a better parametrisation of Skyrme-like effective forces: A critical study of the SkM force”. In: *Nuclear Physics A* 386.1 (1982), pp. 79–100. DOI: [https://doi.org/10.1016/0375-9474\(82\)90403-1](https://doi.org/10.1016/0375-9474(82)90403-1).
- [84] G. Grams et al. “Skyrme–Hartree–Fock–Bogoliubov mass models on a 3D mesh: IV. Improved description of the isospin dependence of pairing”. In: *The European Physical Journal A* 61.2 (Feb. 2025), p. 35. DOI: 10.1140/epja/s10050-025-01503-x.
- [85] J. Dechargé and D. Gogny. “Hartree-Fock-Bogolyubov calculations with the *D1* effective interaction on spherical nuclei”. In: *Phys. Rev. C* 21 (4 Apr. 1980), pp. 1568–1593. DOI: 10.1103/PhysRevC.21.1568.
- [86] J. Berger, M. Girod, and D. Gogny. “Time-dependent quantum collective dynamics applied to nuclear fission”. In: *Computer Physics Communications* 63.1 (1991), pp. 365–374. DOI: [https://doi.org/10.1016/0010-4655\(91\)90263-K](https://doi.org/10.1016/0010-4655(91)90263-K).
- [87] A. Bulgac et al. “Minimal nuclear energy density functional”. In: *Phys. Rev. C* 97 (4 Apr. 2018), p. 044313. DOI: 10.1103/PhysRevC.97.044313.
- [88] A. V. Smirnov, S. V. Tolokonnikov, and S. A. Fayans. “Method of the energy functional with pairing in the coordinate representation”. In: *Sov. J. Nucl. Phys. (Engl. Transl.); (United States)* 48:6 (Dec. 1988).
- [89] S. A. Fayans. “Towards a universal nuclear density functional”. In: *Journal of Experimental and Theoretical Physics Letters* 68.3 (Aug. 1998), pp. 169–174. DOI: 10.1134/1.567841.
- [90] M. Bender, P.-H. Heenen, and P.-G. Reinhard. “Self-consistent mean-field models for nuclear structure”. In: *Rev. Mod. Phys.* 75 (1 Jan. 2003), pp. 121–180. DOI: 10.1103/RevModPhys.75.121.
- [91] N. Schunck and L. M. Robledo. “Microscopic theory of nuclear fission: a review”. In: *Reports on Progress in Physics* 79.11 (Oct. 2016), p. 116301. DOI: 10.1088/0034-4885/79/11/116301.
- [92] N. Schunck et al. “Microscopic calculation of fission product yields for odd-mass nuclei”. In: *Phys. Rev. C* 107 (4 Apr. 2023), p. 044312. DOI: 10.1103/PhysRevC.107.044312.
- [93] N. Schunck, ed. *Energy Density Functional Methods for Atomic Nuclei*. 2053-2563. IOP Publishing, 2019. DOI: 10.1088/2053-2563/aae0ed.

- [94] M. Kortelainen et al. “Nuclear energy density optimization: Large deformations”. In: *Phys. Rev. C* 85 (2 Feb. 2012), p. 024304. DOI: 10.1103/PhysRevC.85.024304.
- [95] D. Vautherin. “Hartree-Fock Calculations with Skyrme’s Interaction. II. Axially Deformed Nuclei”. In: *Phys. Rev. C* 7 (1 Jan. 1973), pp. 296–316. DOI: 10.1103/PhysRevC.7.296.
- [96] J. Dobaczewski and J. Dudek. “Solution of the Skyrme–Hartree–Fock equations in the Cartesian deformed harmonic oscillator basis II. The program HFODD”. In: *Computer Physics Communications* 102.1 (1997), pp. 183–209. DOI: [https://doi.org/10.1016/S0010-4655\(97\)00005-2](https://doi.org/10.1016/S0010-4655(97)00005-2).
- [97] K. Bennaceur and J. Dobaczewski. “Coordinate-space solution of the Skyrme–Hartree–Fock–Bogolyubov equations within spherical symmetry. The program HFBRAD (v1.00)”. In: *Computer Physics Communications* 168.2 (2005), pp. 96–122. DOI: <https://doi.org/10.1016/j.cpc.2005.02.002>.
- [98] J. Maruhn et al. “The TDHF code Sky3D”. In: *Computer Physics Communications* 185.7 (2014), pp. 2195–2216. DOI: <https://doi.org/10.1016/j.cpc.2014.04.008>.
- [99] J. C. Slater. “A Simplification of the Hartree-Fock Method”. In: *Phys. Rev.* 81 (3 Feb. 1951), pp. 385–390. DOI: 10.1103/PhysRev.81.385.
- [100] M. Anguiano, J. Egido, and L. Robledo. “Coulomb exchange and pairing contributions in nuclear Hartree–Fock–Bogoliubov calculations with the Gogny force”. In: *Nuclear Physics A* 683.1 (2001), pp. 227–254. DOI: [https://doi.org/10.1016/S0375-9474\(00\)00445-0](https://doi.org/10.1016/S0375-9474(00)00445-0).
- [101] H. Abusara, A. V. Afanasjev, and P. Ring. “Fission barriers in covariant density functional theory: Extrapolation to superheavy nuclei”. In: *Phys. Rev. C* 85 (2 Feb. 2012), p. 024314. DOI: 10.1103/PhysRevC.85.024314.
- [102] L. Neufcourt et al. “Bayesian approach to model-based extrapolation of nuclear observables”. In: *Phys. Rev. C* 98 (3 Sept. 2018), p. 034318. DOI: 10.1103/PhysRevC.98.034318.
- [103] T. H. R. Skyrme. “CVII. The nuclear surface”. In: *The Philosophical Magazine: A Journal of Theoretical Experimental and Applied Physics* 1.11 (1956), pp. 1043–1054. DOI: 10.1080/14786435608238186.
- [104] J. S. Bell and T. H. R. Skyrme. “CVIII. The nuclear spin-orbit coupling”. In: *The Philosophical Magazine: A Journal of Theoretical Experimental and Applied Physics* 1.11 (1956), pp. 1055–1068. DOI: 10.1080/14786435608238187.

- [105] T. H. R. Skyrme. “The effective nuclear potential”. In: *Nuclear Physics* 9.4 (1958), pp. 615–634. DOI: [https://doi.org/10.1016/0029-5582\(58\)90345-6](https://doi.org/10.1016/0029-5582(58)90345-6).
- [106] J. W. Negele and D. Vautherin. “Density-Matrix Expansion for an Effective Nuclear Hamiltonian”. In: *Phys. Rev. C* 5 (5 May 1972), pp. 1472–1493. DOI: [10.1103/PhysRevC.5.1472](https://doi.org/10.1103/PhysRevC.5.1472).
- [107] J. W. Negele and D. Vautherin. “Density-matrix expansion for an effective nuclear Hamiltonian. II”. In: *Phys. Rev. C* 11 (3 Mar. 1975), pp. 1031–1041. DOI: [10.1103/PhysRevC.11.1031](https://doi.org/10.1103/PhysRevC.11.1031).
- [108] E. Perlińska et al. “Local density approximation for proton-neutron pairing correlations: Formalism”. In: *Phys. Rev. C* 69 (1 Jan. 2004), p. 014316. DOI: [10.1103/PhysRevC.69.014316](https://doi.org/10.1103/PhysRevC.69.014316).
- [109] R. R. Chasman. “Density-dependent delta interactions and actinide pairing matrix elements”. In: *Phys. Rev. C* 14 (5 Nov. 1976), pp. 1935–1945. DOI: [10.1103/PhysRevC.14.1935](https://doi.org/10.1103/PhysRevC.14.1935).
- [110] P. Klüpfel et al. “Variations on a theme by Skyrme: A systematic study of adjustments of model parameters”. In: *Phys. Rev. C* 79 (3 Mar. 2009), p. 034310. DOI: [10.1103/PhysRevC.79.034310](https://doi.org/10.1103/PhysRevC.79.034310).
- [111] N. Schunck et al. “Error analysis in nuclear density functional theory”. In: *Journal of Physics G: Nuclear and Particle Physics* 42.3 (Feb. 2015), p. 034024. DOI: [10.1088/0954-3899/42/3/034024](https://doi.org/10.1088/0954-3899/42/3/034024).
- [112] G. Bertsch and H. Esbensen. “Pair correlations near the neutron drip line”. In: *Annals of Physics* 209.2 (1991), pp. 327–363. DOI: [https://doi.org/10.1016/0003-4916\(91\)90033-5](https://doi.org/10.1016/0003-4916(91)90033-5).
- [113] D. Brink and E. Boeker. “Effective interactions for Hartree-Fock calculations”. In: *Nuclear Physics A* 91.1 (1967), pp. 1–26. DOI: [https://doi.org/10.1016/0375-9474\(67\)90446-0](https://doi.org/10.1016/0375-9474(67)90446-0).
- [114] L. M. Robledo, T. R. Rodríguez, and R. R. Rodríguez-Guzmán. “Mean field and beyond description of nuclear structure with the Gogny force: a review”. In: *Journal of Physics G: Nuclear and Particle Physics* 46.1 (Dec. 2018), p. 013001. DOI: [10.1088/1361-6471/aadebd](https://doi.org/10.1088/1361-6471/aadebd).
- [115] J. Berger, M. Girod, and D. Gogny. “Microscopic analysis of collective dynamics in low energy fission”. In: *Nuclear Physics A* 428 (1984), pp. 23–36. DOI: [https://doi.org/10.1016/0375-9474\(84\)90240-9](https://doi.org/10.1016/0375-9474(84)90240-9).

- [116] P. Lykos and G. W. Pratt. “Discussion on The Hartree-Fock Approximation”. In: *Rev. Mod. Phys.* 35 (3 July 1963), pp. 496–501. DOI: 10.1103/RevModPhys.35.496.
- [117] H. Fukutome. “Theory of the unrestricted Hartree-Fock equation and its solutions. i”. In: *Progress of Theoretical Physics* 45.5 (1971), pp. 1382–1406.
- [118] H. Fukutome. “Theory of the Unrestricted Hartree-Fock Equation and Its Solutions II: Classification and Characterization of UHF Solutions by Their Behavior for Spin Rotation and Time Reversal”. In: *Progress of Theoretical Physics* 52.1 (1974), pp. 115–130.
- [119] M. V. Stoitsov et al. “Variation after particle-number projection for the Hartree-Fock-Bogoliubov method with the Skyrme energy density functional”. In: *Phys. Rev. C* 76 (1 July 2007), p. 014308. DOI: 10.1103/PhysRevC.76.014308.
- [120] H. J. Lipkin. “Collective motion in many-particle systems: Part 1. The violation of conservation laws”. In: *Annals of Physics* 9.2 (1960), pp. 272–291. DOI: [https://doi.org/10.1016/0003-4916\(60\)90032-4](https://doi.org/10.1016/0003-4916(60)90032-4).
- [121] J. F. Goodfellow and Y. Nogami. “On the Superconductivity Approximation for Nuclear Pairing Interaction”. In: *Canadian Journal of Physics* 44.6 (1966), pp. 1321–1327. DOI: 10.1139/p66-111.
- [122] M. Anguiano, J. Egido, and L. Robledo. “Mean-field based approaches to pairing correlations in atomic nuclei”. In: *Physics Letters B* 545.1 (2002), pp. 62–72. DOI: [https://doi.org/10.1016/S0370-2693\(02\)02557-1](https://doi.org/10.1016/S0370-2693(02)02557-1).
- [123] O. Burglin and N. Rowley. “Exact pairing calculations in a large Nilsson-model basis: comparison with BCS and Lipkin-Nogami methods”. In: *Nuclear Physics A* 602.1 (1996), pp. 21–40. DOI: [https://doi.org/10.1016/0375-9474\(96\)00096-6](https://doi.org/10.1016/0375-9474(96)00096-6).
- [124] N. López Vaquero, T. R. Rodríguez, and J. L. Egido. “On the impact of large amplitude pairing fluctuations on nuclear spectra”. In: *Physics Letters B* 704.5 (2011), pp. 520–526. DOI: <https://doi.org/10.1016/j.physletb.2011.09.073>.
- [125] N. L. Vaquero, J. L. Egido, and T. R. Rodríguez. “Large-amplitude pairing fluctuations in atomic nuclei”. In: *Phys. Rev. C* 88 (6 Dec. 2013), p. 064311. DOI: 10.1103/PhysRevC.88.064311.
- [126] A. Staszczak et al. “Coupling of the pairing vibrations with the fission mode”. In: *Physics Letters B* 161.4 (1985), pp. 227–230. DOI: [https://doi.org/10.1016/0370-2693\(85\)90750-6](https://doi.org/10.1016/0370-2693(85)90750-6).
- [127] J. Sadhukhan et al. “Pairing-induced speedup of nuclear spontaneous fission”. In: *Phys. Rev. C* 90 (6 Dec. 2014), p. 061304. DOI: 10.1103/PhysRevC.90.061304.

- [128] J. Sadhukhan et al. “Spontaneous fission lifetimes from the minimization of self-consistent collective action”. In: *Phys. Rev. C* 88 (6 Dec. 2013), p. 064314. DOI: 10.1103/PhysRevC.88.064314.
- [129] R. N. Perez et al. “Axially deformed solution of the Skyrme–Hartree–Fock–Bogolyubov equations using the transformed harmonic oscillator basis (III) hfbtho (v3.00): A new version of the program”. In: *Computer Physics Communications* 220 (2017), pp. 363–375. DOI: <https://doi.org/10.1016/j.cpc.2017.06.022>.
- [130] M. V. Stoitsov, W. Nazarewicz, and S. Pittel. “New discrete basis for nuclear structure studies”. In: *Phys. Rev. C* 58 (4 Oct. 1998), pp. 2092–2098. DOI: 10.1103/PhysRevC.58.2092.
- [131] A. Baran et al. “Broyden’s method in nuclear structure calculations”. In: *Phys. Rev. C* 78 (1 July 2008), p. 014318. DOI: 10.1103/PhysRevC.78.014318.
- [132] M. Stoitsov et al. “Axially deformed solution of the Skyrme–Hartree–Fock–Bogoliubov equations using the transformed harmonic oscillator basis (II) hfbtho v2.00d: A new version of the program”. In: *Computer Physics Communications* 184.6 (2013), pp. 1592–1604. DOI: <https://doi.org/10.1016/j.cpc.2013.01.013>.
- [133] L. M. Robledo and G. F. Bertsch. “Application of the gradient method to Hartree–Fock–Bogoliubov theory”. In: *Phys. Rev. C* 84 (1 July 2011), p. 014312. DOI: 10.1103/PhysRevC.84.014312.
- [134] E. J. Heller. “Time-dependent approach to semiclassical dynamics”. In: *The Journal of Chemical Physics* 62.4 (Feb. 1975), pp. 1544–1555. DOI: 10.1063/1.430620.
- [135] E. J. Heller. “Time dependent variational approach to semiclassical dynamics”. In: *The Journal of Chemical Physics* 64.1 (Jan. 1976), pp. 63–73. DOI: 10.1063/1.431911.
- [136] J.-P. Blaizot et al. *Quantum Theory of Finite Systems and Quantum Many-Particle Systems*. 1988.
- [137] K. Gottfried. *Quantum mechanics: fundamentals*. CRC Press, 2018.
- [138] L. Fonda, G. C. Ghirardi, and A. Rimini. “Decay theory of unstable quantum systems”. In: *Reports on Progress in Physics* 41.4 (Apr. 1978), p. 587. DOI: 10.1088/0034-4885/41/4/003.
- [139] W. Nazarewicz. “Adiabaticity of nuclear motion: problems and perspectives”. In: *Nuclear Physics A* 557 (1993), pp. 489–514. DOI: [https://doi.org/10.1016/0375-9474\(93\)90565-F](https://doi.org/10.1016/0375-9474(93)90565-F).

- [140] P. Kramer and M. Saraceno. *Geometry of the time-dependent variational principle in quantum mechanics*. Springer, 1981.
- [141] P. Kramer and M. Saraceno. “Geometry of the time-dependent variational principle in quantum mechanics”. In: *Group Theoretical Methods in Physics: Proceedings of the IX International Colloquium Held at Cocoyoc, México, June 23–27, 1980*. Springer, 2005, pp. 112–121.
- [142] K. Takatsuka, H. Ushiyama, and A. Inoue-Ushiyama. “Tunneling paths in multi-dimensional semiclassical dynamics”. In: *Physics Reports* 322.5 (1999), pp. 347–417. DOI: [https://doi.org/10.1016/S0370-1573\(99\)00036-8](https://doi.org/10.1016/S0370-1573(99)00036-8).
- [143] A. Shudo, Y. Ishii, and K. S. Ikeda. “Julia sets and chaotic tunneling: I”. In: *Journal of Physics A: Mathematical and Theoretical* 42.26 (June 2009), p. 265101. DOI: 10.1088/1751-8113/42/26/265101.
- [144] A. Shudo, Y. Ishii, and K. S. Ikeda. “Julia sets and chaotic tunneling: II”. In: *Journal of Physics A: Mathematical and Theoretical* 42.26 (June 2009), p. 265102. DOI: 10.1088/1751-8113/42/26/265102.
- [145] S. Keshavamurthy and P. Schlagheck. *Dynamical tunneling: theory and experiment*. CRC Press, 2011.
- [146] T. Nakatsukasa, T. Inakura, and K. Yabana. “Finite amplitude method for the solution of the random-phase approximation”. In: *Phys. Rev. C* 76 (2 Aug. 2007), p. 024318. DOI: 10.1103/PhysRevC.76.024318.
- [147] P. Avogadro and T. Nakatsukasa. “Finite amplitude method for the quasiparticle random-phase approximation”. In: *Phys. Rev. C* 84 (1 July 2011), p. 014314. DOI: 10.1103/PhysRevC.84.014314.
- [148] K. Washiyama, N. Hinohara, and T. Nakatsukasa. “Finite-amplitude method for collective inertia in spontaneous fission”. In: *Phys. Rev. C* 103 (1 Jan. 2021), p. 014306. DOI: 10.1103/PhysRevC.103.014306.
- [149] A. Baran et al. “Quadrupole collective inertia in nuclear fission: Cranking approximation”. In: *Phys. Rev. C* 84 (5 Nov. 2011), p. 054321. DOI: 10.1103/PhysRevC.84.054321.
- [150] E. Yuldashbaeva et al. “Mass parameters for large amplitude collective motion: A perturbative microscopic approach”. In: *Physics Letters B* 461.1 (1999), pp. 1–8. DOI: [https://doi.org/10.1016/S0370-2693\(99\)00836-9](https://doi.org/10.1016/S0370-2693(99)00836-9).

- [151] A. Staszczak, S. Pilat, and K. Pomorski. “Influence of the pairing vibrations on spontaneous fission probability”. In: *Nuclear Physics A* 504.3 (1989), pp. 589–604. DOI: [https://doi.org/10.1016/0375-9474\(89\)90559-9](https://doi.org/10.1016/0375-9474(89)90559-9).
- [152] C. M. Bender and S. A. Orszag. *Advanced mathematical methods for scientists and engineers I: Asymptotic methods and perturbation theory*. Springer Science & Business Media, 2013.
- [153] S. Coleman. “The Uses of Instantons”. In: *The Whys of Subnuclear Physics*. Ed. by A. Zichichi. Boston, MA: Springer US, 1979, pp. 805–941. DOI: 10.1007/978-1-4684-0991-8_16.
- [154] J. O. Richardson. “Perspective: Ring-polymer instanton theory”. In: *The Journal of Chemical Physics* 148.20 (May 2018), p. 200901. DOI: 10.1063/1.5028352.
- [155] A. M. Cooper, P. P. Hallmen, and J. Kästner. “Potential energy surface interpolation with neural networks for instanton rate calculations”. In: *The Journal of Chemical Physics* 148.9 (Mar. 2018), p. 094106. DOI: 10.1063/1.5015950.
- [156] M. Brack et al. “Funny Hills: The Shell-Correction Approach to Nuclear Shell Effects and Its Applications to the Fission Process”. In: *Rev. Mod. Phys.* 44 (2 Apr. 1972), pp. 320–405. DOI: 10.1103/RevModPhys.44.320.
- [157] A. Baran et al. “A dynamic analysis of spontaneous-fission half-lives”. In: *Nuclear Physics A* 361.1 (1981), pp. 83–101. DOI: [https://doi.org/10.1016/0375-9474\(81\)90471-1](https://doi.org/10.1016/0375-9474(81)90471-1).
- [158] A. Baran. “Some dynamical aspects of the fission process”. In: *Physics Letters B* 76.1 (1978), pp. 8–10. DOI: [https://doi.org/10.1016/0370-2693\(78\)90085-0](https://doi.org/10.1016/0370-2693(78)90085-0).
- [159] E. Flynn et al. “Nudged elastic band approach to nuclear fission pathways”. In: *Phys. Rev. C* 105 (5 May 2022), p. 054302. DOI: 10.1103/PhysRevC.105.054302.
- [160] B. C. Garrett and D. G. Truhlar. “A least-action variational method for calculating multidimensional tunneling probabilities for chemical reactions”. In: *The Journal of Chemical Physics* 79.10 (Nov. 1983), pp. 4931–4938. DOI: 10.1063/1.445586.
- [161] G. Mills and H. Jónsson. “Quantum and thermal effects in H₂ dissociative adsorption: Evaluation of free energy barriers in multidimensional quantum systems”. In: *Phys. Rev. Lett.* 72 (7 Feb. 1994), pp. 1124–1127. DOI: 10.1103/PhysRevLett.72.1124.
- [162] G. Mills, H. Jónsson, and G. K. Schenter. “Reversible work transition state theory: application to dissociative adsorption of hydrogen”. In: *Surf. Sci.* 324.2 (1995), pp. 305–337. DOI: [https://doi.org/10.1016/0039-6028\(94\)00731-4](https://doi.org/10.1016/0039-6028(94)00731-4).

- [163] H. Jónsson, G. Mills, and K. W. Jacobsen. “Nudged elastic band method for finding minimum energy paths of transitions”. In: *Classical and Quantum Dynamics in Condensed Phase Simulations*, pp. 385–404. DOI: 10.1142/9789812839664_0016.
- [164] G. Henkelman, B. P. Uberuaga, and H. Jónsson. “A climbing image nudged elastic band method for finding saddle points and minimum energy paths”. In: *J. Chem. Phys.* 113.22 (2000), pp. 9901–9904. DOI: 10.1063/1.1329672.
- [165] G. Henkelman and H. Jónsson. “Improved tangent estimate in the nudged elastic band method for finding minimum energy paths and saddle points”. In: *The Journal of Chemical Physics* 113.22 (Dec. 2000), pp. 9978–9985. DOI: 10.1063/1.1323224.
- [166] B. J. Berne, G. Ciccotti, and D. F. Coker. *Classical and quantum dynamics in condensed phase simulations: Proceedings of the International School of Physics*. World Scientific, 1998.
- [167] L. Verlet. “Computer “Experiments” on Classical Fluids. I. Thermodynamical Properties of Lennard-Jones Molecules”. In: *Phys. Rev.* 159 (1 July 1967), pp. 98–103. DOI: 10.1103/PhysRev.159.98.
- [168] W. C. Swope et al. “A computer simulation method for the calculation of equilibrium constants for the formation of physical clusters of molecules: Application to small water clusters”. In: *The Journal of Chemical Physics* 76.1 (Jan. 1982), pp. 637–649. DOI: 10.1063/1.442716.
- [169] E. Bitzek et al. “Structural Relaxation Made Simple”. In: *Phys. Rev. Lett.* 97 (17 Oct. 2006), p. 170201. DOI: 10.1103/PhysRevLett.97.170201.
- [170] J. Guénolé et al. “Assessment and optimization of the fast inertial relaxation engine (fire) for energy minimization in atomistic simulations and its implementation in lammmps”. In: *Computational Materials Science* 175 (2020), p. 109584. DOI: <https://doi.org/10.1016/j.commatsci.2020.109584>.
- [171] E. W. Dijkstra. “A note on two problems in connexion with graphs”. In: *Numer. Math.* 1.1 (1959), pp. 269–271. DOI: 10.1007/BF01386390.
- [172] K. Müller and L. D. Brown. “Location of saddle points and minimum energy paths by a constrained simplex optimization procedure”. In: *Theoretica chimica acta* 53.1 (Mar. 1979), pp. 75–93. DOI: 10.1007/BF00547608.
- [173] V. Ásgeirsson, A. Arnaldsson, and H. Jónsson. “Efficient evaluation of atom tunneling combined with electronic structure calculations”. In: *The Journal of Chemical Physics* 148.10 (Jan. 2018), p. 102334. DOI: 10.1063/1.5007180.

- [174] J. J. Moré and T. S. Munson. “Computing mountain passes and transition states”. In: *Mathematical Programming* 100.1 (May 2004), pp. 151–182. DOI: 10.1007/s10107-003-0489-0.
- [175] A. Bulgac et al. “Fission dynamics of ^{240}Pu from saddle to scission and beyond”. In: *Phys. Rev. C* 100 (3 Sept. 2019), p. 034615. DOI: 10.1103/PhysRevC.100.034615.
- [176] D. Lay et al. “Multimodal fission from self-consistent calculations”. In: *Phys. Rev. C* 109 (4 Apr. 2024), p. 044306. DOI: 10.1103/PhysRevC.109.044306.
- [177] A. Bulgac, S. Jin, and I. Stetcu. “Nuclear Fission Dynamics: Past, Present, Needs, and Future”. In: *Frontiers in Physics* Volume 8 - 2020 (2020). DOI: 10.3389/fphy.2020.00063.
- [178] G. Scamps, C. Simenel, and D. Lacroix. “Superfluid dynamics of ^{258}Fm fission”. In: *Phys. Rev. C* 92 (1 July 2015), p. 011602. DOI: 10.1103/PhysRevC.92.011602.
- [179] A. Bulgac et al. “Non-Equilibrium Aspects of Fission Dynamics within the Time Dependent Density Functional Theory”. In: *EPJ Web Conf.* 322 (2025), p. 07002. DOI: 10.1051/epjconf/202532207002.
- [180] C. H. Dasso, T. Døssing, and H. C. Pauli. “On the mass distribution in Time-Dependent Hartree-Fock calculations of heavy-ion collisions”. In: *Zeitschrift für Physik A Atoms and Nuclei* 289.4 (Dec. 1979), pp. 395–398. DOI: 10.1007/BF01409391.
- [181] D. Lacroix and S. Ayik. “Stochastic quantum dynamics beyond mean field”. In: *The European Physical Journal A* 50.6 (June 2014), p. 95. DOI: 10.1140/epja/i2014-14095-8.
- [182] D. Regnier, N. Dubray, and N. Schunck. “From asymmetric to symmetric fission in the fermion isotopes within the time-dependent generator-coordinate-method formalism”. In: *Phys. Rev. C* 99 (2 Feb. 2019), p. 024611. DOI: 10.1103/PhysRevC.99.024611.
- [183] J. Zhao et al. “Time-dependent generator-coordinate-method study of mass-asymmetric fission of actinides”. In: *Phys. Rev. C* 99 (5 May 2019), p. 054613. DOI: 10.1103/PhysRevC.99.054613.
- [184] W. Younes, D. M. Gogny, and J.-F. Berger. *A microscopic theory of fission dynamics based on the generator coordinate method*. Vol. 950. Springer, 2019.
- [185] S. Ayik. “A stochastic mean-field approach for nuclear dynamics”. In: *Physics Letters B* 658.4 (2008), pp. 174–179. DOI: <https://doi.org/10.1016/j.physletb.2007.09.072>.

- [186] Y. Tanimura, D. Lacroix, and S. Ayik. “Microscopic Phase-Space Exploration Modeling of ^{258}Fm Spontaneous Fission”. In: *Phys. Rev. Lett.* 118 (15 Apr. 2017), p. 152501. DOI: 10.1103/PhysRevLett.118.152501.
- [187] Y. Abe et al. “On stochastic approaches of nuclear dynamics”. In: *Physics Reports* 275.2 (1996), pp. 49–196. DOI: [https://doi.org/10.1016/0370-1573\(96\)00003-8](https://doi.org/10.1016/0370-1573(96)00003-8).
- [188] S. Ayik et al. “The Boltzmann-Langevin model for nuclear collisions”. In: *Nuclear Physics A* 545.1 (1992), pp. 35–46. DOI: [https://doi.org/10.1016/0375-9474\(92\)90444-0](https://doi.org/10.1016/0375-9474(92)90444-0).
- [189] H. Kramers. “Brownian motion in a field of force and the diffusion model of chemical reactions”. In: *Physica* 7.4 (1940), pp. 284–304. DOI: [https://doi.org/10.1016/S0031-8914\(40\)90098-2](https://doi.org/10.1016/S0031-8914(40)90098-2).
- [190] P. Fröbrich and I. Gontchar. “Langevin description of fusion, deep-inelastic collisions and heavy-ion-induced fission”. In: *Physics Reports* 292.3 (1998), pp. 131–237. DOI: [https://doi.org/10.1016/S0370-1573\(97\)00042-2](https://doi.org/10.1016/S0370-1573(97)00042-2).
- [191] J. Randrup and P. Möller. “Brownian Shape Motion on Five-Dimensional Potential-Energy Surfaces:Nuclear Fission-Fragment Mass Distributions”. In: *Phys. Rev. Lett.* 106 (13 Mar. 2011), p. 132503. DOI: 10.1103/PhysRevLett.106.132503.
- [192] P. Möller and T. Ichikawa. “A method to calculate fission-fragment yields $Y(Z,N)$ versus proton and neutron number in the Brownian shape-motion model”. In: *The European Physical Journal A* 51.12 (Dec. 2015), p. 173. DOI: 10.1140/epja/i2015-15173-1.
- [193] P. Möller and C. Schmitt. “Evolution of uranium fission-fragment charge yields with neutron number”. In: *The European Physical Journal A* 53.1 (Jan. 2017), p. 7. DOI: 10.1140/epja/i2017-12188-6.
- [194] M. R. Mumpower et al. “Primary fission fragment mass yields across the chart of nuclides”. In: *Phys. Rev. C* 101 (5 May 2020), p. 054607. DOI: 10.1103/PhysRevC.101.054607.
- [195] J.-F. Lemaître et al. “New statistical scission-point model to predict fission fragment observables”. In: *Phys. Rev. C* 92 (3 Sept. 2015), p. 034617. DOI: 10.1103/PhysRevC.92.034617.
- [196] J.-F. Lemaître et al. “Fully microscopic scission-point model to predict fission fragment observables”. In: *Phys. Rev. C* 99 (3 Mar. 2019), p. 034612. DOI: 10.1103/PhysRevC.99.034612.

- [197] J.-F. Lemaître et al. “Fission fragment distributions and their impact on the r -process nucleosynthesis in neutron star mergers”. In: *Phys. Rev. C* 103 (2 Feb. 2021), p. 025806. DOI: [10.1103/PhysRevC.103.025806](https://doi.org/10.1103/PhysRevC.103.025806).
- [198] K.-H. Schmidt et al. “General Description of Fission Observables: GEF Model Code”. In: *Nuclear Data Sheets* 131 (2016). Special Issue on Nuclear Reaction Data, pp. 107–221. DOI: <https://doi.org/10.1016/j.nds.2015.12.009>.
- [199] J. Sadhukhan et al. “Efficient method for estimation of fission fragment yields of r -process nuclei”. In: *Phys. Rev. C* 101 (6 June 2020), p. 065803. DOI: [10.1103/PhysRevC.101.065803](https://doi.org/10.1103/PhysRevC.101.065803).
- [200] J. Sadhukhan, S. A. Giuliani, and W. Nazarewicz. “Theoretical description of fission yields: Toward a fast and efficient global model”. In: *Phys. Rev. C* 105 (1 Jan. 2022), p. 014619. DOI: [10.1103/PhysRevC.105.014619](https://doi.org/10.1103/PhysRevC.105.014619).
- [201] P.-G. Reinhard et al. “Localization in light nuclei”. In: *Phys. Rev. C* 83 (3 Mar. 2011), p. 034312. DOI: [10.1103/PhysRevC.83.034312](https://doi.org/10.1103/PhysRevC.83.034312).
- [202] C. L. Zhang, B. Schuetrumpf, and W. Nazarewicz. “Nucleon localization and fragment formation in nuclear fission”. In: *Phys. Rev. C* 94 (6 Dec. 2016), p. 064323. DOI: [10.1103/PhysRevC.94.064323](https://doi.org/10.1103/PhysRevC.94.064323).
- [203] P. Fong. “Asymmetric Fission”. In: *Phys. Rev.* 89 (1 Jan. 1953), pp. 332–333. DOI: [10.1103/PhysRev.89.332](https://doi.org/10.1103/PhysRev.89.332).
- [204] J. Sadhukhan, W. Nazarewicz, and N. Schunck. “Microscopic modeling of mass and charge distributions in the spontaneous fission of ^{240}Pu ”. In: *Phys. Rev. C* 93 (1 Jan. 2016), p. 011304. DOI: [10.1103/PhysRevC.93.011304](https://doi.org/10.1103/PhysRevC.93.011304).
- [205] Y. Miyamoto et al. “Origin of the dramatic change of fission mode in fermium isotopes investigated using Langevin equations”. In: *Phys. Rev. C* 99 (5 May 2019), p. 051601. DOI: [10.1103/PhysRevC.99.051601](https://doi.org/10.1103/PhysRevC.99.051601).
- [206] M. Albertsson et al. “Super-short fission mode in fermium isotopes”. In: *Phys. Rev. C* 104 (6 Dec. 2021), p. 064616. DOI: [10.1103/PhysRevC.104.064616](https://doi.org/10.1103/PhysRevC.104.064616).
- [207] P. Möller, J. Nix, and W. Swiatecki. “Calculated fission properties of the heaviest elements”. In: *Nuclear Physics A* 469.1 (1987), pp. 1–50. DOI: [https://doi.org/10.1016/0375-9474\(87\)90083-2](https://doi.org/10.1016/0375-9474(87)90083-2).
- [208] M. Warda et al. “Self-consistent calculations of fission barriers in the Fm region”. In: *Phys. Rev. C* 66 (1 July 2002), p. 014310. DOI: [10.1103/PhysRevC.66.014310](https://doi.org/10.1103/PhysRevC.66.014310).

- [209] A. Staszczak et al. “Microscopic description of complex nuclear decay: Multimodal fission”. In: *Phys. Rev. C* 80 (1 July 2009), p. 014309. DOI: 10.1103/PhysRevC.80.014309.
- [210] K. Depta et al. “Bimodal Fission in ^{258}Fm ”. In: *Mod. Phys. Lett. A* 01.06 (1986), pp. 377–381. DOI: 10.1142/S0217732386000464.
- [211] P. Möller, J. Nix, and W. Swiatecki. “New developments in the calculation of heavy-element fission barriers”. In: *Nucl. Phys. A* 492.3 (1989), pp. 349–387. DOI: 10.1016/0375-9474(89)90403-X.
- [212] P. Möller et al. “Five-dimensional potential-energy surfaces and coexisting fission modes in heavy nuclei”. In: *AIP Conf. Proc.* 561.1 (Apr. 2001), pp. 455–468. DOI: 10.1063/1.1372821.
- [213] M. Warda et al. “Fission paths in Fm region calculated with the Gogny forces”. In: *Phys. At. Nucl.* 66 (2003), pp. 1178–1181. DOI: 10.1134/1.1586434.
- [214] M. Warda et al. “Microscopic Structure of The Bimodal Fission of ^{258}Fm ”. In: *Int. J. of Mod. Phys. E* 13.01 (2004), pp. 169–174. DOI: 10.1142/S0218301304001904.
- [215] T. Asano et al. “Dynamical calculation of multi-modal nuclear fission of fermium nuclei”. In: *J. Nucl. Radiochem. Sci.* 5.1 (2004), pp. 1–5. DOI: 10.14494/jnrs2000.5.1.
- [216] L. Bonneau. “Fission modes of ^{256}Fm and ^{258}Fm in a microscopic approach”. In: *Phys. Rev. C* 74 (1 July 2006), p. 014301. DOI: 10.1103/PhysRevC.74.014301.
- [217] C. Simenel and A. S. Umar. “Formation and dynamics of fission fragments”. In: *Phys. Rev. C* 89 (3 Mar. 2014), 031601(R). DOI: 10.1103/PhysRevC.89.031601.
- [218] K. Pomorski et al. “Fission Fragment Mass and Kinetic Energy Yields of Fermium Isotopes”. In: *Acta Phys. Pol. B* 54 (2023), 9–A2. DOI: 10.5506/APhysPolB.54.9-A2.
- [219] R. Bernard, C. Simenel, and G. Blanchon. “Hartree–Fock–Bogoliubov study of quantum shell effects on the path to fission in ^{180}Hg , ^{236}U and ^{256}Fm ”. In: *Eur. Phys. J. A* 59.3 (2023), p. 51. URL: <https://doi.org/10.1140/epja/s10050-023-00964-2>.
- [220] R. M. Harbour et al. “Mass and Nuclear Charge Distributions from the Spontaneous Fission of ^{254}Fm ”. In: *Phys. Rev. C* 8 (4 Oct. 1973), pp. 1488–1493. DOI: 10.1103/PhysRevC.8.1488.
- [221] J. E. Gindler et al. “Distribution of mass, kinetic energy, and neutron yield in the spontaneous fission of ^{254}Fm ”. In: *Phys. Rev. C* 16 (4 Oct. 1977), pp. 1483–1492. DOI: 10.1103/PhysRevC.16.1483.

- [222] K. F. Flynn et al. “Distribution of Mass in the Spontaneous Fission of ^{256}Fm ”. In: *Phys. Rev. C* 5 (5 May 1972), pp. 1725–1729. DOI: 10.1103/PhysRevC.5.1725.
- [223] D. C. Hoffman et al. “12.3-min ^{256}Cf and 43-min ^{258}Md and systematics of the spontaneous fission properties of heavy nuclides”. In: *Phys. Rev. C* 21 (3 Mar. 1980), pp. 972–981. DOI: 10.1103/PhysRevC.21.972.
- [224] R. Smolańczuk, J. Skalski, and A. Sobiczewski. “Spontaneous-fission half-lives of deformed superheavy nuclei”. In: *Phys. Rev. C* 52 (4 Oct. 1995), pp. 1871–1880. DOI: 10.1103/PhysRevC.52.1871.
- [225] S. A. Giuliani et al. “Colloquium: Superheavy elements: Oganesson and beyond”. In: *Rev. Mod. Phys.* 91 (1 Jan. 2019), p. 011001. DOI: 10.1103/RevModPhys.91.011001.
- [226] M. Itkis et al. “Fusion and fission of heavy and superheavy nuclei (experiment)”. In: *Nucl. Phys. A* 944 (2015). Special Issue on Superheavy Elements, pp. 204–237. DOI: 10.1016/j.nuclphysa.2015.09.007.
- [227] L. P. Somerville et al. “Spontaneous fission of rutherfordium isotopes”. In: *Phys. Rev. C* 31.5 (1985), p. 1801. DOI: 10.1103/PhysRevC.31.1801.
- [228] A. Sobiczewski and K. Pomorski. “Description of structure and properties of superheavy nuclei”. In: *Prog. Part. Nucl. Phys.* 58.1 (2007), pp. 292–349. DOI: <https://doi.org/10.1016/j.pnpnp.2006.05.001>.
- [229] K. E. Gregorich et al. “New isotope ^{264}Sg and decay properties of $^{262-264}\text{Sg}$ ”. In: *Phys. Rev. C* 74 (4 Oct. 2006), p. 044611. DOI: 10.1103/PhysRevC.74.044611.
- [230] J. M. Gates et al. “Synthesis of rutherfordium isotopes in the $^{238}\text{U}(^{26}\text{Mg}, xn)^{264-x}\text{Rf}$ reaction and study of their decay properties”. In: *Phys. Rev. C* 77 (3 Mar. 2008), p. 034603. DOI: 10.1103/PhysRevC.77.034603.
- [231] A. Staszczak, A. Baran, and W. Nazarewicz. “Spontaneous fission modes and lifetimes of superheavy elements in the nuclear density functional theory”. In: *Phys. Rev. C* 87 (2 Feb. 2013), p. 024320. DOI: 10.1103/PhysRevC.87.024320.
- [232] A. Afanasjev, S. Agbemava, and A. Gyawali. “Hyperheavy nuclei: Existence and stability”. In: *Phys. Lett. B* 782 (2018), pp. 533–540. DOI: <https://doi.org/10.1016/j.physletb.2018.05.070>.
- [233] A. Baran et al. “Fission barriers and probabilities of spontaneous fission for elements with $Z \geq 100$ ”. In: *Nuc. Phys. A* 944 (2015). Special Issue on Superheavy Elements, pp. 442–470. DOI: <https://doi.org/10.1016/j.nuclphysa.2015.06.002>.

- [234] N. Sowmya et al. “Competition between Cluster and Alpha Decay in Even Atomic Number Superheavy Nuclei $110 \leq Z \leq 126$ ”. In: *Phys. Part. Nucl. Lett.* 20.3 (2023), pp. 544–555. URL: <https://doi.org/10.1134/S1547477123030664>.
- [235] P. V. Kostyukov et al. “Potential energy surfaces and fission fragment mass yields of even-even superheavy nuclei *”. In: *Chinese Phys. C* 45.12 (Dec. 2021), p. 124108. DOI: 10.1088/1674-1137/ac29a3.
- [236] C. Ishizuka et al. “Nuclear fission properties of super heavy nuclei described within the four-dimensional Langevin model”. In: *Front. Phys.* 11 (2023), p. 1111868. URL: <https://doi.org/10.3389/fphy.2023.1111868>.
- [237] Z. Matheson et al. “Cluster radioactivity of ^{294}Og ”. In: *Phys. Rev. C* 99.4 (Apr. 2019), 041304(R). DOI: 10.1103/PhysRevC.99.041304.
- [238] D. Lay et al. “Neural network emulation of spontaneous fission”. In: *Phys. Rev. C* 109 (4 Apr. 2024), p. 044305. DOI: 10.1103/PhysRevC.109.044305.
- [239] P. Giuliani et al. “Bayes goes fast: Uncertainty quantification for a covariant energy density functional emulated by the reduced basis method”. In: *Frontiers in Physics* 10 (2023). DOI: 10.3389/fphy.2022.1054524.
- [240] E. Bonilla et al. “Training and projecting: A reduced basis method emulator for many-body physics”. In: *Phys. Rev. C* 106 (5 2022), p. 054322. DOI: 10.1103/PhysRevC.106.054322.
- [241] M. Verriere et al. “Building surrogate models of nuclear density functional theory with Gaussian processes and autoencoders”. In: *Frontiers in Physics* Volume 10 - 2022 (2022). DOI: 10.3389/fphy.2022.1028370.
- [242] D. Odell et al. “ROSE: A reduced-order scattering emulator for optical models”. In: *Phys. Rev. C* 109 (4 2024), p. 044612. DOI: 10.1103/PhysRevC.109.044612.
- [243] S. Lalit, A. C. Semposki, and J. M. Maldonado. “Star Log-extended eMulation: a method for efficient computation of the Tolman-Oppenheimer-Volkoff equations”. In: *arXiv preprint arXiv:2411.10556* (2024).
- [244] D. Lay. “Novel Computational Approaches for Nuclear Fission Theory”. English. PhD thesis. 2025, p. 110. URL: <https://www.proquest.com/dissertations-theses/novel-computational-approaches-nuclear-fission/docview/3182185919/se-2>.
- [245] D. Schlosshauer. “The quantum-to-classical transition”. In: *The Frontiers Collection (Springer-Verlag, 2007)* (2007).

- [246] R. Feynman and A. Hibbs. “The path integral formulation of quantum mechanics”. In: *McGraw-Hill, New York* (1965).
- [247] S. Levit. “Time-dependent mean-field approximation for nuclear dynamical problems”. In: *Phys. Rev. C* 21 (4 Apr. 1980), pp. 1594–1602. DOI: 10.1103/PhysRevC.21.1594.
- [248] S. Levit, J. W. Negele, and Z. Paltiel. “Time-dependent mean-field theory and quantized bound states”. In: *Phys. Rev. C* 21 (4 Apr. 1980), pp. 1603–1625. DOI: 10.1103/PhysRevC.21.1603.
- [249] S. Levit, J. W. Negele, and Z. Paltiel. “Barrier penetration and spontaneous fission in the time-dependent mean-field approximation”. In: *Phys. Rev. C* 22 (5 Nov. 1980), pp. 1979–1995. DOI: 10.1103/PhysRevC.22.1979.
- [250] H. Reinhardt. “Semiclassical theory of large amplitude collective excitations”. In: *Nuclear Physics A* 346.1 (1980), pp. 1–69. DOI: [https://doi.org/10.1016/0375-9474\(80\)90488-1](https://doi.org/10.1016/0375-9474(80)90488-1).
- [251] H. Reinhardt. “Semiclassical theory of nuclear fission”. In: *Nuclear Physics A* 367.2 (1981), pp. 269–312. DOI: [https://doi.org/10.1016/0375-9474\(81\)90517-0](https://doi.org/10.1016/0375-9474(81)90517-0).
- [252] E. Fradkin. *Quantum field theory: an integrated approach*. Princeton University Press, 2021.
- [253] A. Altland and B. D. Simons. *Condensed matter field theory*. Cambridge university press, 2010.
- [254] B. Hatfield. *Quantum field theory of point particles and strings*. CRC Press, 2018.
- [255] L. H. Ryder. *Quantum field theory*. Cambridge university press, 1996.
- [256] A. Zee. *Quantum field theory in a nutshell*. Vol. 7. Princeton university press, 2010.
- [257] L. S. Schulman. *Techniques and applications of path integration*. Courier Corporation, 2012.
- [258] M. C. M. Wright. “Green function or green’s function?” In: *Nature Physics* 2.10 (Oct. 2006), pp. 646–646. DOI: 10.1038/nphys411.
- [259] J. Feldbrugge and N. Turok. “Existence of real time quantum path integrals”. In: *Annals of Physics* 454 (2023), p. 169315. DOI: <https://doi.org/10.1016/j.aop.2023.169315>.

- [260] J. Feldbrugge, D. L. Jow, and U.-L. Pen. “Complex classical paths in quantum reflections and tunneling”. In: *Phys. Rev. D* 111 (8 Apr. 2025), p. 085027. DOI: 10.1103/PhysRevD.111.085027.
- [261] E. Witten. *A New Look At The Path Integral Of Quantum Mechanics*. 2010. URL: <https://arxiv.org/abs/1009.6032>.
- [262] E. Witten. *Analytic Continuation Of Chern-Simons Theory*. 2010. URL: <https://arxiv.org/abs/1001.2933>.
- [263] N. Turok. “On quantum tunneling in real time”. In: *New Journal of Physics* 16.6 (June 2014), p. 063006. DOI: 10.1088/1367-2630/16/6/063006.
- [264] Y. Tanizaki and T. Koike. “Real-time Feynman path integral with Picard–Lefschetz theory and its applications to quantum tunneling”. In: *Annals of Physics* 351 (2014), pp. 250–274. DOI: <https://doi.org/10.1016/j.aop.2014.09.003>.
- [265] A. Cherman and M. Unsal. *Real-Time Feynman Path Integral Realization of Instantons*. 2014. URL: <https://arxiv.org/abs/1408.0012>.
- [266] Z.-G. Mou, P. M. Saffin, and A. Tranberg. “Quantum tunnelling, real-time dynamics and Picard-Lefschetz thimbles”. In: *Journal of High Energy Physics* 2019.11 (Nov. 2019), p. 135. DOI: 10.1007/JHEP11(2019)135.
- [267] J. Nishimura, K. Sakai, and A. Yosprakob. “A new picture of quantum tunneling in the real-time path integral from Lefschetz thimble calculations”. In: *Journal of High Energy Physics* 2023.9 (Sept. 2023), p. 110. DOI: 10.1007/JHEP09(2023)110.
- [268] J. Nishimura and H. Watanabe. “Quantum Decoherence from Complex Saddle Points”. In: *Phys. Rev. Lett.* 134 (21 May 2025), p. 210401. DOI: 10.1103/PhysRevLett.134.210401.
- [269] H. Reinhardt. “Time-dependent mean field S-matrix theory”. In: *Nuclear Physics A* 390.1 (1982), pp. 70–116. DOI: [https://doi.org/10.1016/0375-9474\(82\)90607-8](https://doi.org/10.1016/0375-9474(82)90607-8).
- [270] J. J. Griffin, P. C. Lichtner, and M. Dworzecka. “Time-dependent— \mathcal{S} -matrix Hartree-Fock theory of complex reactions”. In: *Phys. Rev. C* 21 (4 Apr. 1980), pp. 1351–1376. DOI: 10.1103/PhysRevC.21.1351.
- [271] Y. Alhassid and S. E. Koonin. “Mean-field approximation to the many-body S matrix”. In: *Phys. Rev. C* 23 (4 Apr. 1981), pp. 1590–1611. DOI: 10.1103/PhysRevC.23.1590.

- [272] H. Flocard. “Time dependent Hartree-Fock-present status- possible prolongations”. In: *Nuclear Physics A* 387.1 (1982), pp. 283–295. DOI: [https://doi.org/10.1016/0375-9474\(82\)90206-8](https://doi.org/10.1016/0375-9474(82)90206-8).
- [273] E. A. Remler. “Cross-sections from TDHF calculations”. In: *Time-Dependent Hartree-Fock and Beyond*. Ed. by K. Goeke and P. .-. Reinhard. Berlin, Heidelberg: Springer Berlin Heidelberg, 1982, pp. 288–296.
- [274] J. Ankerhold. *Quantum tunneling in complex systems: the semiclassical approach*. Vol. 224. Springer, 2007.
- [275] S. Coleman. “Fate of the false vacuum: Semiclassical theory”. In: *Phys. Rev. D* 15 (10 May 1977), pp. 2929–2936. DOI: [10.1103/PhysRevD.15.2929](https://doi.org/10.1103/PhysRevD.15.2929).
- [276] C. G. Callan and S. Coleman. “Fate of the false vacuum. II. First quantum corrections”. In: *Phys. Rev. D* 16 (6 Sept. 1977), pp. 1762–1768. DOI: [10.1103/PhysRevD.16.1762](https://doi.org/10.1103/PhysRevD.16.1762).
- [277] M. Marino. *Instantons and large N: an introduction to non-perturbative methods in quantum field theory*. Cambridge University Press, 2015.
- [278] J. Drut, R. Furnstahl, and L. Platter. “Toward ab initio density functional theory for nuclei”. In: *Progress in Particle and Nuclear Physics* 64.1 (2010), pp. 120–168. DOI: <https://doi.org/10.1016/j.pnpnp.2009.09.001>.
- [279] R. Furnstahl and H.-W. Hammer. “Effective Field Theory for Fermi Systems in a Large N Expansion”. In: *Annals of Physics* 302.2 (2002), pp. 206–228. DOI: <https://doi.org/10.1006/aphy.2002.6313>.
- [280] J. W. Negele. *Quantum many-particle systems*. CRC Press, 2018.
- [281] P. Romatschke. *Quantum Field Theory in Large N Wonderland: Three Lectures*. 2024. URL: <https://arxiv.org/abs/2310.00048>.
- [282] J. W. Negele. “Microscopic theory of fission dynamics”. In: *Nuclear Physics A* 502 (1989), pp. 371–386.
- [283] J. Skalski. “Nuclear fission with mean-field instantons”. In: *Phys. Rev. C* 77 (6 June 2008), p. 064610. DOI: [10.1103/PhysRevC.77.064610](https://doi.org/10.1103/PhysRevC.77.064610).
- [284] W. Brodziński and J. Skalski. “Instanton-motivated study of spontaneous fission of odd- A nuclei”. In: *Phys. Rev. C* 102 (5 Nov. 2020), p. 054603. DOI: [10.1103/PhysRevC.102.054603](https://doi.org/10.1103/PhysRevC.102.054603).

- [285] S. Levit. “Variational approach to tunneling dynamics. Application to hot superfluid Fermi systems. Spontaneous and induced fission”. In: *Physics Letters B* 813 (2021), p. 136042. DOI: <https://doi.org/10.1016/j.physletb.2020.136042>.
- [286] J. V. Beck, B. Blackwell, and C. R. S. Clair. *Inverse heat conduction: Ill-posed problems*. James Beck, 1985.
- [287] W. F. Ames and B. Straughan. *Non-standard and improperly posed problems*. Vol. 194. Elsevier, 1997.
- [288] S.-I. Chu. “Recent Developments in Semiclassical Floquet Theories for Intense-Field Multiphoton Processes”. In: ed. by D. Bates and B. Bederson. Vol. 21. *Advances in Atomic and Molecular Physics*. Academic Press, 1985, pp. 197–253. DOI: [https://doi.org/10.1016/S0065-2199\(08\)60143-8](https://doi.org/10.1016/S0065-2199(08)60143-8).
- [289] S.-I. Chu and D. A. Telnov. “Beyond the Floquet theorem: generalized Floquet formalisms and quasienergy methods for atomic and molecular multiphoton processes in intense laser fields”. In: *Physics Reports* 390.1 (2004), pp. 1–131. DOI: <https://doi.org/10.1016/j.physrep.2003.10.001>.
- [290] J. Walecka. “A theory of highly condensed matter”. In: *Annals of Physics* 83.2 (1974), pp. 491–529. DOI: [https://doi.org/10.1016/0003-4916\(74\)90208-5](https://doi.org/10.1016/0003-4916(74)90208-5).
- [291] L. N. Savushkin and H. Toki. *The atomic nucleus as a relativistic system*. Springer Science & Business Media, 2013.
- [292] J. Meng. *Relativistic density functional for nuclear structure*. Vol. 10. World Scientific, 2016.
- [293] S. Kratochvila and P. de Forcrand. “QCD at zero baryon density and the Polyakov loop paradox”. In: *Phys. Rev. D* 73 (11 June 2006), p. 114512. DOI: [10.1103/PhysRevD.73.114512](https://doi.org/10.1103/PhysRevD.73.114512).
- [294] A. Li et al. “Finite density phase transition of QCD with $N_f = 4$ and $N_f = 2$ using canonical ensemble method”. In: *Phys. Rev. D* 82 (5 June 2010), p. 054502. DOI: [10.1103/PhysRevD.82.054502](https://doi.org/10.1103/PhysRevD.82.054502).
- [295] J. Danzer and C. Gattringer. “Properties of canonical determinants and a test of fugacity expansion for finite density lattice QCD with Wilson fermions”. In: *Phys. Rev. D* 86 (1 July 2012), p. 014502. DOI: [10.1103/PhysRevD.86.014502](https://doi.org/10.1103/PhysRevD.86.014502).
- [296] C. Gattringer and H.-P. Schadler. “Generalized quark number susceptibilities from fugacity expansion at finite chemical potential for $N_f = 2$ Wilson fermions”. In: *Phys. Rev. D* 91 (7 Apr. 2015), p. 074511. DOI: [10.1103/PhysRevD.91.074511](https://doi.org/10.1103/PhysRevD.91.074511).

- [297] B. D. Serot and J. Walecka. “Properties of finite nuclei in a relativistic quantum field theory”. In: *Physics Letters B* 87.3 (1979), pp. 172–176. DOI: [https://doi.org/10.1016/0370-2693\(79\)90957-2](https://doi.org/10.1016/0370-2693(79)90957-2).
- [298] B. D. Serot. “A relativistic nuclear field theory with π and ρ mesons”. In: *Physics Letters B* 86.2 (1979), pp. 146–150. DOI: [https://doi.org/10.1016/0370-2693\(79\)90804-9](https://doi.org/10.1016/0370-2693(79)90804-9).
- [299] W. H. Press. *Numerical recipes 3rd edition: The art of scientific computing*. Cambridge university press, 2007.
- [300] A. Alexandru et al. “Sign problem and Monte Carlo calculations beyond Lefschetz thimbles”. In: *Journal of High Energy Physics* 2016.5 (May 2016), p. 53. DOI: 10.1007/JHEP05(2016)053.
- [301] S. Lawrence and Y. Yamauchi. “Normalizing flows and the real-time sign problem”. In: *Phys. Rev. D* 103 (11 June 2021), p. 114509. DOI: 10.1103/PhysRevD.103.114509.
- [302] S. Lawrence, H. Oh, and Y. Yamauchi. “Lattice scalar field theory at complex coupling”. In: *Phys. Rev. D* 106 (11 Dec. 2022), p. 114503. DOI: 10.1103/PhysRevD.106.114503.
- [303] S. Lawrence and Y. Yamauchi. “Convex optimization of contour deformations”. In: *Phys. Rev. D* 110 (1 July 2024), p. 014508. DOI: 10.1103/PhysRevD.110.014508.
- [304] D. J. Earl and M. W. Deem. “Parallel tempering: Theory, applications, and new perspectives”. In: *Phys. Chem. Chem. Phys.* 7 (23 2005), pp. 3910–3916. DOI: 10.1039/B509983H.
- [305] R. H. Swendsen and J.-S. Wang. “Replica Monte Carlo Simulation of Spin-Glasses”. In: *Phys. Rev. Lett.* 57 (21 Nov. 1986), pp. 2607–2609. DOI: 10.1103/PhysRevLett.57.2607.
- [306] A. Umar et al. “Basis-spline collocation method for the lattice solution of boundary value problems”. In: *Journal of Computational Physics* 93.2 (1991), pp. 426–448. DOI: [https://doi.org/10.1016/0021-9991\(91\)90193-0](https://doi.org/10.1016/0021-9991(91)90193-0).
- [307] J. P. Boyd. *Chebyshev and Fourier spectral methods*. Courier Corporation, 2001.
- [308] D. Gottlieb and S. A. Orszag. *Numerical analysis of spectral methods: theory and applications*. SIAM, 1977.
- [309] L. N. Trefethen. *Spectral methods in MATLAB*. SIAM, 2000.

- [310] N. Schunck, D. Duke, and H. Carr. “Description of induced nuclear fission with Skyrme energy functionals. II. Finite temperature effects”. In: *Phys. Rev. C* 91 (3 2015), p. 034327. DOI: 10.1103/PhysRevC.91.034327.
- [311] G. Baym and C. Pethick. “Landau Fermi-liquid theory: concepts and applications”. In: (2008).
- [312] N. Michel and M. Ploszajczak. *Gamow shell model*. Vol. 983. Springer, 2021.
- [313] O. Smits et al. “Pushing the limits of the periodic table - A review on atomic relativistic electronic structure theory and calculations for the superheavy elements”. In: *Physics Reports* 1035 (2023), pp. 1–57. DOI: <https://doi.org/10.1016/j.physrep.2023.09.004>.
- [314] B. Nagels, L. J. F. Hermans, and P. L. Chapovsky. “Quantum Zeno Effect Induced by Collisions”. In: *Phys. Rev. Lett.* 79 (17 1997), pp. 3097–3100. DOI: 10.1103/PhysRevLett.79.3097.
- [315] A. Kofman and G. Kurizki. “Acceleration of quantum decay processes by frequent observations”. In: *Nature* 405.6786 (2000), pp. 546–550.
- [316] A. D. Godbeer, J. S. Al-Khalili, and P. D. Stevenson. “Environment-induced dephasing versus von Neumann measurements in proton tunneling”. In: *Phys. Rev. A* 90 (1 2014), p. 012102. DOI: 10.1103/PhysRevA.90.012102.
- [317] A. Caldeira and A. Leggett. “Quantum tunnelling in a dissipative system”. In: *Annals of Physics* 149.2 (1983), pp. 374–456. DOI: [https://doi.org/10.1016/0003-4916\(83\)90202-6](https://doi.org/10.1016/0003-4916(83)90202-6).
- [318] S. L. Brunton and J. N. Kutz. *Data-driven science and engineering: Machine learning, dynamical systems, and control*. Cambridge University Press, 2022.
- [319] A. Quarteroni, A. Manzoni, and F. Negri. *Reduced basis methods for partial differential equations: an introduction*. Vol. 92. Springer, 2015.
- [320] P. Cook et al. “Parametric Matrix Models”. In: *arXiv preprint arXiv:2401.11694* (2024).
- [321] B. T. Reed et al. “Toward Accelerated Nuclear-physics Parameter Estimation from Binary Neutron Star Mergers: Emulators for the Tolman–Oppenheimer–Volkoff Equations”. In: *The Astrophysical Journal* 974.2 (Oct. 2024), p. 285. DOI: 10.3847/1538-4357/ad737c.

- [322] R. Somasundaram et al. “Emulators for scarce and noisy data: Application to auxiliary field diffusion Monte Carlo for the deuteron”. In: *Physics Letters B* 866 (2025), p. 139558. DOI: <https://doi.org/10.1016/j.physletb.2025.139558>.
- [323] A. Nouri et al. “Skeletal Kinetics Reduction for Astrophysical Reaction Networks”. In: *The Astrophysical Journal Supplement Series* 272.2 (2024), p. 34.
- [324] Y. Saito. “Development of statistical tools for studies of the rapid neutron capture process”. PhD thesis. University of British Columbia, 2023.
- [325] W. Quapp and D. Heidrich. “Analysis of the concept of minimum energy path on the potential energy surface of chemically reacting systems”. In: *Theoret. Chim. Acta.* 66.3 (1984), pp. 245–260. DOI: <https://doi.org/10.1007/BF00549673>.